Spitzer Space Telescope Spectroscopy of Comets: Data Set Overview

Michael S. P. Kelley[1], David E. Harker[2], Charles E. Woodward[3], and Diane H. Wooden[4]

[1]*Department of Astronomy, University of Maryland, 4254 Stadium Dr, College Park, MD 20742, USA*

[2]*Center for Astrophysics and Space Sciences, University of California, San Diego, 9500 Gilman Drive, La Jolla, CA 92093-0424, USA*

[3]*Physics and Astronomy, 116 Church Street, S.E., University of Minnesota, Minneapolis, MN 55455, USA*

[4]*NASA Ames Research Center, Space Science Division, MS 245-1, Moffett Field, CA 94035-1000, USA*

July 3, 2021

Contents

1 Introduction **4**

2 Observations **5**

3 Data Processing and Reduction Strategy **11**

3.1 IRS pipeline 11

3.2 Spectral reduction 11

3.2.1 Background removal 12

3.2.2 Spectral extraction apertures 13

3.2.3 Exposure combining and spectral trimming 13

3.2.4 Nucleus subtraction 15

3.2.5 Point source versus extended source calibration 16

3.2.6 Order-to-order scaling 17

3.2.7 Spectral uncertainties 18

4 Known Issues and Caveats **19**
4.1 Spectral fringing . . . 19
4.2 14-μm teardrop . . . 19
4.3 Gas emission . . . 19
4.4 Effective field-of-view, exposures, and integration time . . . 19
4.5 Spectral shape from 19 to 23 μm . . . 20

5 Data Notes by Target **20**
5.1 6P/d'Arrest . . . 20
5.2 8P/Tuttle . . . 20
5.3 9P/Tempel 1 . . . 21
5.4 17P/Holmes . . . 21
5.5 21P/Giacobini-Zinner . . . 21
5.6 29P/Schwassmann-Wachmann 1 . . . 22
5.7 37P/Forbes . . . 22
5.8 41P/Tuttle-Giacobini-Kresák . . . 22
5.9 46P/Wirtanen . . . 22
5.10 48P/Johnson . . . 23
5.11 62P/Tsuchinshan 1 . . . 23
5.12 65P/Gunn . . . 23
5.13 67P/Churyumov-Gerasimenko . . . 23
5.14 71P/Clark . . . 24
5.15 73P/Schwassmann-Wachmann 3 . . . 24
5.16 78P/Gehrels 2 . . . 24
5.17 88P/Howell . . . 24
5.18 105P/Singer Brewster . . . 25
5.19 121P/Shoemaker-Holt 2 . . . 25
5.20 123P/West-Hartley . . . 25
5.21 132P/Helin-Roman-Alu 2 . . . 25
5.22 144P/Kushida . . . 25
5.23 C/2001 Q4 (NEAT) . . . 25
5.24 C/2003 K4 (LINEAR) . . . 26
5.25 C/2003 T3 (Tabur) . . . 26
5.26 C/2003 T4 (LINEAR) . . . 26
5.27 C/2004 B1 (LINEAR) . . . 26
5.28 C/2004 Q2 (Machholz) . . . 26

5.29 C/2006 P1 (McNaught) . . . 27
5.30 C/2006 Q1 (McNaught) . . . 27
5.31 C/2007 N3 (Lulin) . . . 27
5.32 C/2008 T2 (Cardinal) . . . 27

A Spectral Map Reconstruction Artifacts **28**

B Slit Losses and Cometary Comae **29**
B.1 Slit centered on the comet . . . 31
B.2 Offset spectra . . . 32

C Comet Spectra **36**

List of Figures

1 Example unprocessed spectra. . . . 14
2 Example spectra coadded, trimmed, and bad data removed. . . . 15
3 Derivation of order-to-order scaling factors for the example spectra. . . . 17
4 Following Fig. 3, the order-to-order scale factors are applied producing the final spectrum. . . . 18
5 Comparison of spectra reduced with SPICE and CUBSIM. . . . 30
6 Slit-loss correction functions for cometary comae. . . . 32
7 Model comae calibrated as a point source or uniform source. . . . 33
8 Percent spectral error based on Fig. 7. . . . 34
9 Percent spectral error for a ρ^{-1} coma and a 5″ offset from the peak surface brightness. . . . 35
10 Comet 6P/d'Arrest. . . . 40
11 Comet 8P/Tuttle. . . . 41
12 Comet 9P/Tempel 1. . . . 42
13 Comet 17P/Holmes. . . . 43
14 Comet 21P/Giacobini-Zinner. . . . 44
15 Comet 29P/Schwassmann-Wachmann 1. . . . 45
16 Comet 37P/Forbes. . . . 46
17 Comet 41P/Tuttle-Giacobini-Kresák. . . . 47
18 Comet 46P/Wirtanen. . . . 48
19 Comet 48P/Johnson. . . . 49
20 Comet 62P/Tsuchinshan 1. . . . 50

21 Comet 65P/Gunn. 51
22 Comet 67P/Churyumov-Gerasimenko. 52
23 Comet 71P/Clark. 53
24 Comet 73P/Schwassmann-Wachmann 3 B. 54
25 Comet 73P/Schwassmann-Wachmann 3 C. 55
26 Comet 78P/Gerhels 2. 56
27 Comet 88P/Howell. 57
28 Comet 105P/Singer Brewser. 58
29 Comet 121P/Shoemaker-Holt 2. 59
30 Comet 123P/West-Hartley. 60
31 Comet 132P/Helin-Roman-Alu 2. 61
32 Comet 144P/Kushida. 62
33 Comet C/2001 Q4 (NEAT). 63
34 Comet C/2003 K4 (LINEAR). 64
35 Comet C/2003 T3 (Tabur). 65
36 Comet C/2003 T4 (LINEAR). 66
37 Comet C/2004 B1 (LINEAR). 67
38 Comet C/2004 Q2 (Machholz). 68
39 Comet C/2006 P1 (McNaught). 69
40 Comet C/2006 Q1 (McNaught). 70
41 Comet C/2007 N3 (Lulin). 71
42 Comet C/2008 T2 (Cardinal). 72

List of Tables

1 Properties of the observation modes used in this data set. 6
2 Survey targets and observational parameters. 7
3 *Spitzer* Astronomical Observation Request (AOR) identifiers. 9
4 Extraction apertures for Spectral Stare observations. 13

1 Introduction

Cometary nuclei formed from dust and volatiles present in the outer Solar System during the epoch of planet formation. After formation, comets were scattered into their current cold-storage zones: the trans-Neptunian region and the Oort cloud.

Their interior compositions have likely been preserved since incorporation into the nucleus. In particular, cometary dust may be unaltered, and compositional studies of the dust have provided us with insights into the processes extant in the early Solar System (Wooden et al. 2007, 2017; Brownlee 2014).

Mid-infrared spectroscopy (i.e., $\lambda \sim 5$–50 μm) is a useful technique for the study of cometary dust. Wooden (2002) details the main spectral features of dust in this wavelength regime. There are broad ($\Delta\lambda \gtrsim 1$ μm) emission features from amorphous silicate-type materials at 8–11 μm; narrow ($\Delta\lambda \sim 0.1$ μm) emission features from Mg-rich crystalline olivine near 11.1, 19.5, 23.5, 33.5 μm, as well as weaker features; and narrow emission features from Mg-rich crystalline ortho-pyroxene at 9.3 and 10.5 μm (Koike et al. 2003). Carbonaceous materials and metal sulfides are found in abundance in cometary dust and interplanetary dust particles (IDPs) thought to have cometary origins, but lack strong spectral signatures in the mid-infrared. Instead, these materials contribute to a smooth, featureless continuum with an effective temperature that tends to be warmer than the local thermodynamic equilibrium temperature of a large blackbody sphere.

The *Spitzer Space Telescope* (Werner et al. 2004) observed over 100 comets as part of its Guaranteed Time and General Observer programs, producing a data set that may be used, among other science goals, to assess the dust properties of comets. We present a spectroscopic survey of comets at mid-infrared wavelengths based on the *Spitzer* data archive. Low-resolution, long-slit spectra are reduced with a uniform approach, so that users of the data set may investigate the dust properties of each comet, and explore comet-to-comet comparisons. This document summarizes the observations and methods used to produce the final spectra.

2 Observations

Our survey goal is to assess the dust properties of the comet population using observations and thermal emission models executed with a homogeneous approach (Harker et al. in prep.). This goal can be achieved with low-resolution spectroscopy ($R \sim 100$) at moderate signal-to-noise ratios, SNR $\gtrsim 20$. *Spitzer*'s primary spectroscopic instrument is the InfraRed Spectrograph (IRS; Houck et al. 2004). The IRS has four detectors, with six spectroscopic entrance apertures, and two filters for direct imaging. Our data set utilizes the the Short-Low (SL, 5–14 μm) and Long-Low (LL, 14–40 μm) modules, each with a spectral resolving power, $R = \lambda/\Delta\lambda$, ranging from 60–130. Observations with the high-resolution modules, Short-High (SH) and Long-High (LH)

Table 1: Properties of the observation modes used in this data set.

Module	λ range (μm)	R^b	Pixel scale (″)	Aperture (″)
SL2	5.1–7.6	60–127	1.8	3.6×57
SL3[a]	7.3–8.7			
SL1	7.5–14.3	61–120		3.7×57
LL2	13.9–21.3	57–126	5.1	10.5×168
LL3[a]	19.2–21.6			
LL1	19.9–39.9	58–112		10.7×168

[a]Bonus order within the SL2/LL2 module.
[b]Spectral resolving power.

with $R \sim 600$, were not used in this study. A summary of the spectral and spatial properties of the low-resolution modules is presented in Table 1. Details may be found in the IRS Instrument Handbook (Spitzer Science Center 2012).

We searched the *Spitzer* Heritage Archive[1] for IRS observations of comets that meet our SNR threshold. Additional spectra below our SNR threshold were included only when they were part of an observational time series, e.g., multiple observations of a comet across a wide range of heliocentric distances. Our target list is presented in Table 2. Astronomical Observation Request (AOR) identifiers, unique identifiers for all *Spitzer* observations, are given in Table 3. These IDs can be used to retrieve the original data from the *Spitzer* Heritage Archive.

The low-resolution modules each have two parallel slits. The first, named SL1 or LL1, produces the first-order spectrum of the grating. The second slit, named SL2 or LL2, produces the second-order spectrum. A bonus segment of the first order spectrum is also present on the detector when observing through the SL2 or LL2 slits. These bonus spectra are named SL3 and LL3. *Spitzer*'s orientation with respect to the Sun is fixed (±2°). The long-dimensions of the LL slits is approximately in line with the Sun direction. The long-dimensions of the SL slits are nearly perpendicular (84°) to those of the LL slits. The meta data in the data set labels documents the position angle of the reference slit (described in Section 3.2.6) for each observation with the `Spectral_Characteristics` class attribute `Field_of_View/Rectangular_FOV/celestial_north_position_angle`.

All IRS spectral observations may be preceded by a target acquisition through the Blue or Red broadband filters (16 and 22 μm, respectively). The target acquisition would take two exposures, move the brightest source to a predefined location, and

[1]Presently online at the Infrared Science Archive (IRSA) via `https://sha.ipac.caltech.edu/`.

Table 2: Survey targets and observational parameters.

Comet	Prog.	Date (UT)	r_h (au)	Δ (au)	θ (°)	Mode	Modules	N_{exp}	t_{exp} (s)
(1)	(2)	(3)	(4)	(5)	(6)	(7)	(8)	(9)	(10)
6P/d'Arrest	50335	2008-09-12 07:05	1.392	0.596	41.5	Stare	SL1 SL2	4	134
8P/Tuttle	40270	2007-11-02 18:11	1.606	1.322	39.4	Stare	LL1 LL2 SL1 SL2	24	151
9P/Tempel 1	3658	2005-07-02 12:22	1.506	0.711	35.8	Stare	LL1 LL2 SL1 SL2	16	235
9P/Tempel 1	3658	2005-07-03 06:48	1.506	0.714	36.0	Stare	LL1 LL2 SL1 SL2	24	352
17P/Holmes	466	2007-11-10 19:51	2.505	1.867	21.3	Map	LL1 LL2 SL1 SL2	4	25
21P/Giacobini-Zinner	20021	2005-12-18 20:18	2.292	1.907	25.9	Map	LL1 LL2 SL1 SL2	12	403
29P/Schwassmann-Wachmann 1	1081	2003-11-23 07:17	5.734	5.540	10.1	Stare	LL1 LL2 SL1	10	239
37P/Forbes	20021	2005-10-14 15:11	1.735	1.185	35.0	Map	LL1 LL2 SL1 SL2	12	403
41P/Tuttle-Giacobini-Kresák	20021	2006-04-18 02:13	1.275	0.866	51.8	Map	SL1 SL2	6	63
46P/Wirtanen	40042	2007-12-08 11:44	1.290	0.585	50.0	Stare	SL1 SL2	12	126
46P/Wirtanen	40042	2008-01-17 20:41	1.078	0.446	69.1	Stare	SL1 SL2	12	75
46P/Wirtanen	40042	2008-04-24 15:27	1.494	0.807	39.0	Stare	LL1 LL2 SL1 SL2	24	529
46P/Wirtanen	40042	2008-05-24 01:26	1.742	1.227	34.5	Stare	LL1 LL2 SL1 SL2	90	4728
46P/Wirtanen	40042	2008-07-02 13:08	2.076	1.912	29.1	Stare	LL1 LL2 SL1	50	4267
48P/Johnson	210	2004-10-04 14:47	2.311	1.740	24.4	Stare	LL1 LL2 SL1	24	352
62P/Tsuchinshan 1	131	2005-02-13 08:38	1.650	0.921	32.4	Map	SL1 SL2	6	88
65P/Gunn	210	2004-08-10 15:53	3.478	3.003	16.1	Stare	LL1 LL2 SL1	24	630
67P/Churyumov-Gerasimenko	30589	2008-06-29 19:41	2.784	2.492	21.3	Stare	LL1 LL2	36	1133
67P/Churyumov-Gerasimenko	50022	2008-11-28 09:03	1.652	1.005	35.7	Map	LL1 LL2 SL1 SL2	10	80
67P/Churyumov-Gerasimenko	50022	2008-11-29 02:36	1.647	1.006	35.9	Map	LL1 LL2 SL1 SL2	10	80
67P/Churyumov-Gerasimenko	50022	2008-11-29 16:49	1.643	1.007	36.1	Map	LL1 LL2 SL1 SL2	10	80
67P/Churyumov-Gerasimenko	50022	2008-11-30 11:41	1.637	1.008	36.4	Map	LL1 LL2 SL1 SL2	10	80
71P/Clark	20021	2006-05-27 13:29	1.566	0.910	37.6	Map	LL1 LL2 SL1 SL2	20	756
73P/Schwassmann-Wachmann 3 B	20205	2006-04-17 14:07	1.192	0.441	54.8	Stare	SL1 SL2	8	1211
73P/Schwassmann-Wachmann 3 B	30066	2006-08-06 04:14	1.259	0.846	53.9	Stare	LL1 LL2 SL1 SL2	102	8411
73P/Schwassmann-Wachmann 3 C	20205	2006-03-17 00:57	1.466	0.784	40.0	Stare	SL1 SL2	8	1211
73P/Schwassmann-Wachmann 3 C	30066	2006-08-06 01:14	1.267	0.864	53.4	Stare	SL1 SL2	30	1829
78P/Gehrels 2	210	2004-09-01 14:22	2.059	1.531	28.6	Stare	LL1 LL2 SL1	24	352
88P/Howell	210	2004-09-01 14:47	1.996	1.391	28.7	Stare	LL1 LL2 SL1	24	352
105P/Singer Brewster	2316	2005-07-14 13:37	2.091	1.918	29.1	Stare	SL1 SL2	16	605
121P/Shoemaker-Holt 2	2316	2005-04-22 22:16	2.989	2.357	17.0	Stare	SL1 SL2	16	234
123P/West-Hartley	210	2004-02-04 08:00	2.176	1.600	25.2	Stare	LL1 LL2	6	88

Continued on next page.

Table 2, continued.

Comet	Prog.	Date (UT)	r_h (au)	Δ (au)	θ (°)	Mode	Modules	N_{exp}	t_{exp} (s)
(1)	(2)	(3)	(4)	(5)	(6)	(7)	(8)	(9)	(10)
132P/Helin-Roman-Alu 2	20021	2005-11-20 03:18	2.074	1.480	27.3	Map	LL1 LL2 SL1 SL2	12	403
144P/Kushida	50335	2008-12-06 05:55	1.552	0.827	36.9	Map	SL1 SL2	18	727
C/2001 Q4 (NEAT)	131	2004-10-23 09:21	2.622	2.528	22.7	Stare	SL1 SL2	12	176
C/2003 K4 (LINEAR)	131	2004-07-16 05:01	1.760	1.409	35.4	Map	SL1 SL2	6	88
C/2003 K4 (LINEAR)	20021	2005-09-13 06:01	4.501	4.283	13.1	Stare	LL1 LL2 SL1	17	1587
C/2003 T3 (Tabur)	2316	2005-01-11 18:04	3.560	2.961	14.3	Stare	LL1 LL2 SL1 SL2	24	1026
C/2003 T4 (LINEAR)	20104	2005-11-22 17:29	3.514	3.265	16.7	Stare	LL1 LL2 SL1 SL2	32	4104
C/2003 T4 (LINEAR)	20104	2006-01-29 19:56	4.257	3.774	12.6	Stare	LL1 LL2 SL1	26	3464
C/2003 T4 (LINEAR)	20104	2006-03-07 07:18	4.636	4.385	12.4	Stare	LL1 LL2	12	1463
C/2004 B1 (LINEAR)	20104	2005-10-15 05:35	2.210	2.031	27.5	Map	SL1 SL2	8	1228
C/2004 B1 (LINEAR)	20104	2006-05-16 05:34	2.058	1.608	28.7	Map	SL1 SL2	6	202
C/2004 B1 (LINEAR)	20104	2006-07-26 03:51	2.689	2.234	21.5	Map	LL1 LL2 SL1 SL2	14	1118
C/2004 B1 (LINEAR)	20104	2007-03-08 08:19	4.814	4.766	12.0	Stare	LL1 LL2 SL1	20	3158
C/2004 B1 (LINEAR)	20104	2007-06-09 20:14	5.643	5.395	10.2	Stare	LL1 LL2	36	4388
C/2004 Q2 (Machholz)	3152	2005-07-01 07:52	2.547	2.297	23.6	Map	SL1 SL2	16	101
C/2006 P1 (McNaught)	291	2007-05-04 19:58	2.398	2.224	24.8	Stare	LL1 LL2 SL1 SL2	20	865
C/2006 P1 (McNaught)	40812	2007-08-02 17:01	3.624	3.137	15.3	Stare	LL1 LL2 SL1 SL2	40	7275
C/2006 P1 (McNaught)	40812	2007-09-06 07:41	4.044	3.849	14.7	Stare	LL1 LL2 SL1	54	7782
C/2006 Q1 (McNaught)	30069	2007-03-22 02:05	5.279	5.174	10.9	Stare	LL1 LL2	34	4145
C/2006 Q1 (McNaught)	30069	2008-01-17 14:30	3.253	3.214	18.0	Map	LL1 LL2 SL1	9	82
C/2006 Q1 (McNaught)	30069	2008-02-25 07:56	3.066	2.673	18.6	Map	SL1 SL2	6	38
C/2006 Q1 (McNaught)	30069	2008-07-02 02:41	2.764	2.375	21.1	Map	LL1 LL2 SL1 SL2	12	126
C/2006 Q1 (McNaught)	50335	2008-07-09 16:50	2.764	2.475	21.5	Map	SL1 SL2	8	269
C/2007 N3 (Lulin)	50335	2008-10-04 06:45	1.901	1.673	32.6	Map	SL1 SL2	8	269
C/2008 T2 (Cardinal)	50335	2009-04-04 08:25	1.607	1.088	37.9	Map	LL1 LL2 SL1 SL2	24	151

Column notes — (1) Comet designation; (2) *Spitzer* observation program ID; (3) Observation start time; (4) Heliocentric distance; (5) *Spitzer*-comet distance; (6) Phase (*Spitzer*-comet-Sun) angle; (7) IRS observational mode; (8) IRS modules used; (9) Total number of exposures, all modules (see Section 4.4); (10) Total exposure time, all modules (see Section 4.4).

Table 3: *Spitzer* Astronomical Observation Request (AOR) identifiers.

Comet	r_h (au)	Primary AOR	Shadow AOR[a]	Other background AORs[a]
6P	1.392	25987072	25988352	...
8P	1.606	22857728	22857984	...
9P	1.506	15299072	...	...
9P	1.506	15299328	...	...
17P	2.505	24534784	...	24537344
21P	2.291	13817344	13825536	...
29P	5.734	6068992	...	...
37P	1.735	13817600	13825792	...
41P	1.275	13817856	13826048	...
46P	1.290	22240768	22241024	...
46P	1.078	22240256	22240512	...
46P	1.494	22238720	22238976	...
46P	1.742	22239232	22239488	...
46P	2.076	22239744	22240000	...
48P	2.311	6614016	...	...
62P	1.650	11625984	...	...
65P	3.478	6040064	...	9502208
67P	2.784	18555648	18559488	...
67P	1.652	25229568	25229824	...
67P	1.647	25230080	25230336	...
67P	1.643	25230592	25230848	...
67P	1.637	25231104	25231360	...
71P	1.566	13818368	13826304	...
73P-B	1.192	14394368	15895552	...
73P-B	1.259	17718016	17718784	...
73P-C	1.466	14394880	15895808	...
73P-C	1.267	17718528	17719296	...
78P	2.059	6615296	...	5297152
88P	1.996	6612224	...	5297152
105P	2.091	12207104	...	...
121P	2.989	10195200	...	...
123P	2.176	6615552	...	4169216
132P	2.074	13819392	...	...
144P	1.552	25987840	...	...
C/2001 Q4	2.622	6589952	...	9833728
C/2003 K4	1.760	8525056	...	4733952
C/2003 K4	4.501	13823488	13825280	...
C/2003 T3	3.560	10201344	...	...
C/2003 T4	3.514	15790080	15789056	...
C/2003 T4	4.257	15788800	15791360	...
C/2003 T4	4.636	15789824	15786240	...
C/2004 B1	2.211	15787008	15787776	...
C/2004 B1	2.058	15791616	15790848	...
C/2004 B1	2.689	15791104	15788544	...
C/2004 B1	4.814	15789568	15788288	...
C/2004 B1	5.643	15789312	15790336	...

Continued on next page.

Table 3, continued.

Comet	r_h (au)	Primary AOR	Shadow AOR[a]	Other background AORs[a]
C/2004 Q2	2.547	12814592	12813312	···
C/2006 P1	2.398	21477376	···	···
C/2006 P1	3.624	23237376	23237632	···
C/2006 P1	4.044	23237888	23238144	···
C/2006 Q1	5.279	20674560	20677376	···
C/2006 Q1	3.253	20675840	20676352	···
C/2006 Q1	3.066	20675328	20676864	···
C/2006 Q1	2.764	20675072	20675584	···
C/2006 Q1	2.764	25986816	25988096	···
C/2007 N3	1.901	25987584	25988864	···
C/2008 T2	1.607	32551936	32551680	···

[a] Not all observations have shadow data, and other backgrounds were only occasionally used (see Section 3.2.1). " ··· " indicates these techniques were not used for background subtraction.

take two more exposures. If the sequence was successful, the science target would then be placed into the slit. If the sequence failed, the offset would be discarded and the telescope would proceed with the spectral observations. Thus data may be taken without being centered on the coma.

The IRS can operate in a Spectral Stare or Spectral Mapping mode. The Spectral Stare mode centers the target coordinates in the narrow-dimension of a slit and exposures are taken at two well-separated locations along the long-dimension of the slit (i.e., long-slit nodding). In Spectral Mapping mode, the telescope would move the target along a 2D grid, taking exposures at each point, with offsets and grid spacings specified by the observer. In Table 2, we list the mode for each observation. See the IRS Instrument Handbook (Spitzer Science Center 2012) for more details on the observing modes.

Some high-SNR observations were intentionally left out of our survey:

- The spectrum of comet 10P/Tempel 2 was taken during a period of low or no activity, and therefore dominated by the nucleus (Kelley et al. 2017).
- The spectra of comet 2P/Encke from 2004 is nucleus dominated at short wavelengths (Kelley et al. 2006). There is a 10-μm silicate feature, but no significant spectral signatures at longer wavelengths.
- The spectra of comet 9P/Tempel 1 after the *Deep Impact* excavation event (Lisse et al. 2006) were not included. However, we do include the two epochs before impact.

3 Data Processing and Reduction Strategy

3.1 IRS pipeline

All data were initially processed at the *Spitzer* Science Center with the IRS pipeline, version S18.18. Details of the pipeline are presented in the IRS Instrument Handbook (Spitzer Science Center 2012). In summary, the pipeline: (1) identifies radiation hits on the detector; (2) extrapolates saturated pixels, if possible; (3) corrects for known constant offset artifacts; (4) removes dark current; (5) estimates the pixel-by-pixel signal-to-noise ratio; (6) corrects for detector non-linearities; (7) removes stray light and instrument cross-talk; and (8) applies a flat-field correction. The final products are 2D arrays of the detector focal planes for each commanded exposure. These data products are designated Basic Calibrated Data (BCD) and not included in this data set, but they are available for download from the *Spitzer* Heritage Archive.

3.2 Spectral reduction

Our reduction methods process the observations to produce a single spectrum of the inner coma. Each BCD product is background subtracted before spectral extraction (Section 3.2.1). Independent of the observation mode (Spectral Stare versus Spectral Map), we extract 1D spectra (3.2.2) using the Spitzer IRS Custom Extraction (SPICE) software available from the *Spitzer* Science Center (Teplitz & Brinkworth 2011). The SPICE software is a standard spectral extraction tool, specifically designed for IRS data. We avoid extracting spectra from spatial-spectral data cubes generated from the Spectral Map observations for two reasons. The foremost issue is that most of the spectral maps were not observed with optimal mapping strategies, which results in spectral shape artifacts when processed to generate spatial-spectral data cubes. This issue is described in detail in Appendix A. Moreover, our science goals are focused on the inner coma composition, therefore only the brightest pointings are kept when a target is observed with the Spectral Mapping mode.

Spectra extracted from multiple exposures are scaled together and averaged (3.2.3). If a nucleus size estimate is available and the observation centered on the nucleus / inner-coma, then we generate a model nuclear spectrum and subtract it from the data (3.2.4). If the observation missed the peak of the coma, and the spatial distribution in the slit is no longer point-source like, then an additional calibration factor is applied to correct the spectral shape as appropriate for an extended source (3.2.5). Finally, the spectral orders are combined into a single, near-continuous spectrum (3.2.6), and

the spectral uncertainties computed (3.2.7).

This process is largely independent of any cometary dust model expectations. However, preliminary model fits of the data set were produced as the reduction progressed. Discrepancies or unusual results from the model fits, and comet-to-comet comparisons prompted us to reconsider the spectral reduction in some cases, and led us to discover clear errors in the reduction that were subsequently mitigated. However, we avoided arbitrary revisions in the absence of any obvious reduction issues.

Below we describe each step in our reduction process. Examples from a Spectral Stare observation of 9P/Tempel 1 are shown in Figs. 1–4. We will refer to these figures to demonstrate our techniques.

3.2.1 Background removal

For background removal, we take advantage of the two-slit design of each low-resolution module, whenever possible. When the first-order slit (SL1 or LL1) is pointed at a target, the second-order slit (SL2 or LL2, respectively) is pointed at nearby sky. Since the light from both slits fall on the same detector, the nearby sky spectrum may be used as a background reference. If the background data are free from significant extended coma and bright background sources, we average the sky observations with outlier rejection, and subtract the result, pixel-by-pixel, from the on-source data.

Spitzer also has the ability to repeat an observation of a moving target after a user-specified time period. This "shadow" observation repeats the same observing mode, non-sidereal rates, and integration times at the same commanded sky coordinates as the original target. If the AOR was designed with a shadow observation, then we pair up BCDs and subtract the shadow observation from the on-source observation. In some circumstances, residual background remained, likely due to the changing zodiacal light between the prime and shadow epochs. For these cases we make an additional background subtraction with the accompanying sky measurements as summarized above.

These were the most common background removal techniques, e.g., the 9P/Tempel example presented in Figs. 1–4 used the nearby sky method. If other strategies are used, e.g., a dedicated sky observation near in time and sky coordinates from another AOR, then we describe them along with the data reduction notes in Section 5.

3.2.2 Spectral extraction apertures

The comets in our data set are generally extended sources. However, the IRS instrument is calibrated with point sources. Since the IRS is diffraction limited, point source spectroscopy is best executed with a variable-width extraction aperture, tuned to the variation of the point spread function (PSF) with wavelength. In observations of extended sources, such an aperture introduces a false spectral slope. For an ideal cometary coma ($1/\rho$ surface brightness distribution, where ρ is the projected distance to the nucleus) and IRS point source aperture, the effect can easily be tens of percent over the full wavelength range of one module. This artificial slope is avoided with a fixed-width aperture. Therefore, we use a fixed-width aperture for all spectral extractions. Aperture widths are chosen to coincide with the largest widths used for point sources. The values are listed in Table 4, including the equivalent circular aperture radius for an ideal coma ($1/\rho$). Figure 1 shows spectra of comet 9P/Tempel 1 after IRS pipeline processing, background subtraction, and spectral extraction with a fixed-width aperture.

Table 4: Extraction apertures for Spectral Stare observations.

Module	Width[a] ($''$)	ρ_{eff}[b] ($''$)
SL1	3.7×17	3.8
SL2/3	3.6×17	3.7
LL1/2/3	11×52	11

[a]Slit and extraction aperture widths.
[b]Equivalent circular aperture radius for an ideal coma.

3.2.3 Exposure combining and spectral trimming

Extractions from individual exposures are combined order-by-order. Telescope jitter and target ephemeris uncertainties cause small pointing offsets, which are manifested in the data as time variations in the total spectral flux. The spectra for each order are scaled to a common flux density (the observation median), then averaged together with outlier rejection to mitigate the effects of cosmic rays and "rogue" pixels (Spitzer Science Center 2012). Scaling the spectra to a common flux value before co-adding helps preserve spectral shape and improves the outlier rejection when combining the exposures. Figure 2 displays the 9P/Tempel 1 spectrum after intra-order averaging.

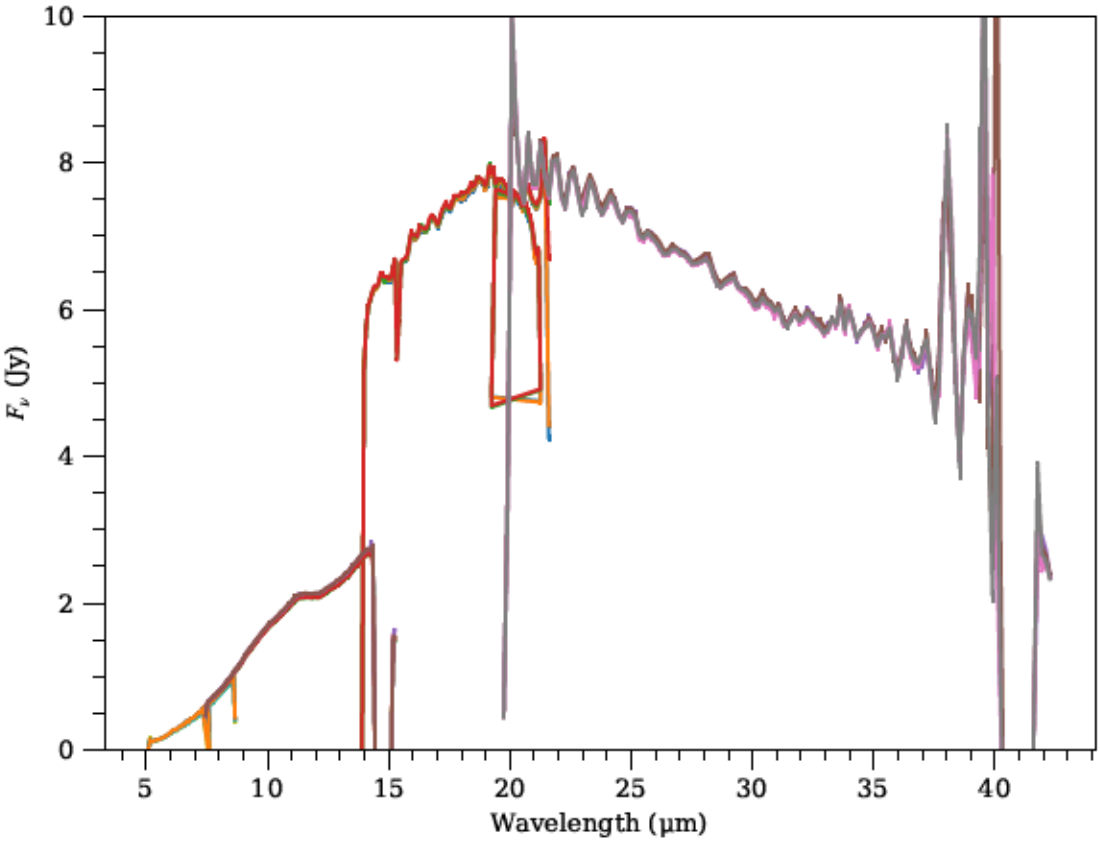

Figure 1: All extracted spectra of 9P/Tempel 1 from 2005 July 02. Bad data (e.g., near 9, 15, and 41 μm) and poor agreement between spectral orders (at 7–8 and 19–21 μm) are apparent. The different aperture sizes of the SL and LL modules are apparent in the factor of 3 difference in spectral flux density from 13 to 15 μm.

The edges of the orders are trimmed, based on an examination of the data by eye. The chosen wavelengths where orders are trimmed depend on SNR of the data, the accuracy of the spectral calibration (which may vary with position in the slit), and consistency of the spectral shape between all exposures. The trimming is conservative in the sense that only when an issue is apparent are the data trimmed. This may result in redundant data points in regions where the spectra overlap with another order, i.e., the orders are not combined and are left as independent measurements of the source. Comparing Fig. 1 and Fig. 2 illustrates the process.

The data where the LL orders overlap are especially difficult to interpret, due to spectral fringing and the roll off of sensitivities at the order edges. We caution interpretations in the 19–23 μm region, and elaborate further in Section 4.5.

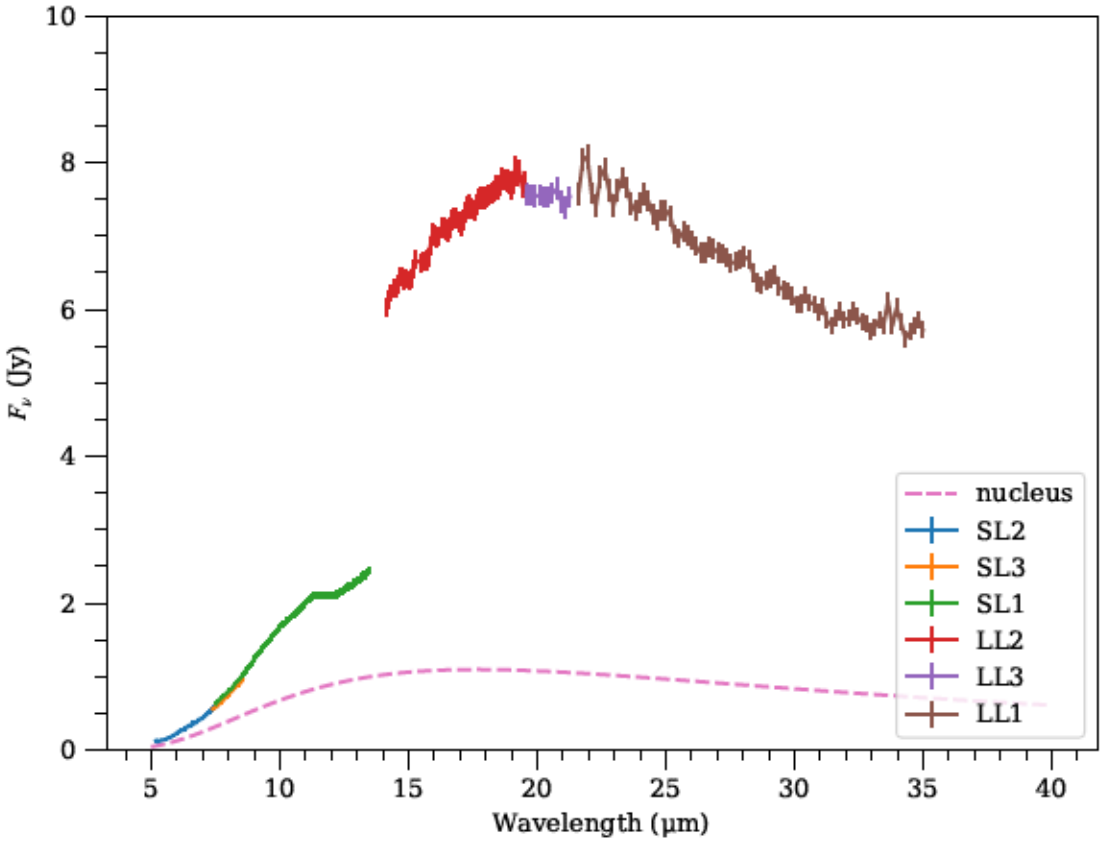

Figure 2: Following Fig. 1, the spectra are co-added by order, trimmed, and bad data removed. A model nucleus is shown before subtraction from the spectra.

3.2.4 Nucleus subtraction

In order to derive a pure coma spectrum, the nucleus must be removed from the data, if possible. Emission from the nucleus can affect continuum shape and strength, e.g., by preferentially enhancing the short-wavelength flux density distribution which would bias model-retrieved dust properties (Hanner et al. 1985; Kelley & Wooden 2009). We model nuclei with the near-Earth asteroid thermal model (NEATM; Harris 1998), and the parameters of Fernández et al. (2013): infrared emissivity of 0.95, infrared beaming parameter of 1.0, an optical geometric albedo of 5%, and a phase integral of 0.39 (used to convert the geometric albedo to bolometric albedo; Hanner et al. 1981). The uncertainties in this process may be substantial: we are using a single effective radius, but comets tend to have significantly non-spherical shapes (Kokotanekova et al. 2017; Keller & Kührt 2020). Moreover, many comets, especially those from the Oort cloud, do not have nucleus size estimates. However, we prefer to subtract the nucleus whenever possible. Comments regarding nucleus subtraction are

provided in the notes for individual comets. If a nuclear spectrum was subtracted from the data as part of the reduction, then the NEATM model fluxes were included in the data tables (field name `nucleus`). A model nuclear spectrum of comet 9P/Tempel 1 is given in Fig. 2.

3.2.5 Point source versus extended source calibration

The IRS modules are calibrated with point sources. The fraction of light from a point source that falls within the narrow-slit varies with wavelength. This variation is automatically accounted for in the IRS pipeline during calibration of point source spectra. In contrast, for extended sources with a near-uniform surface brightness distribution the fraction of light that falls within the narrow-slit does not vary. Since comae are intermediate to point sources and extended sources, this effect must be carefully considered when calibrating IRS observations of comets.

The IRS calibration data files include a slit-loss correction function, which is used to calibrate spectra of extended sources (see Section 4.1.5.2 of Spitzer Science Center 2012). We use this calibration factor in Spectral Stare observations when the slit is not centered on the nucleus (i.e., offset into the coma or tail). However, the inner coma, despite formally being an extended source, behaves similar to a point source on size scales close to the diffraction limit of the instrument. This is because the coma's surface brightness distribution, $1/\rho$, is strongly peaked on small size scales.

We calculated slit-loss correction functions specific to comae and IRS spectroscopy by estimating the slit throughput for model coma surface brightness distributions. The model comae are convolved with the wavelength dependent point source function for each low-resolution IRS module. Details are given in Appendix B. The results were compared to the slit-loss functions for point sources and extended sources. We find that treating a $1/\rho$ coma as a point source results in spectral slope errors at the $\approx 5\%$ level, but that treating it as an extended source yields errors as high as 15%.

In practice, the $1/\rho$ coma is a reasonable model, but other slopes, especially steeper functions (i.e., more point-source like), are not uncommon. We conclude that the assumption that the coma is a point source is sufficient for a narrow-slit observation when that slit is centered on a coma. This approach is a deviation from previous Spectral Stare observations of comae discussed by, e.g., Kelley et al. (2006) and Sitko et al. (2011). We calibrate the data as an extended source and apply the slit-loss correction function when an observation is offset into the coma at least one slit width along the dispersion direction.

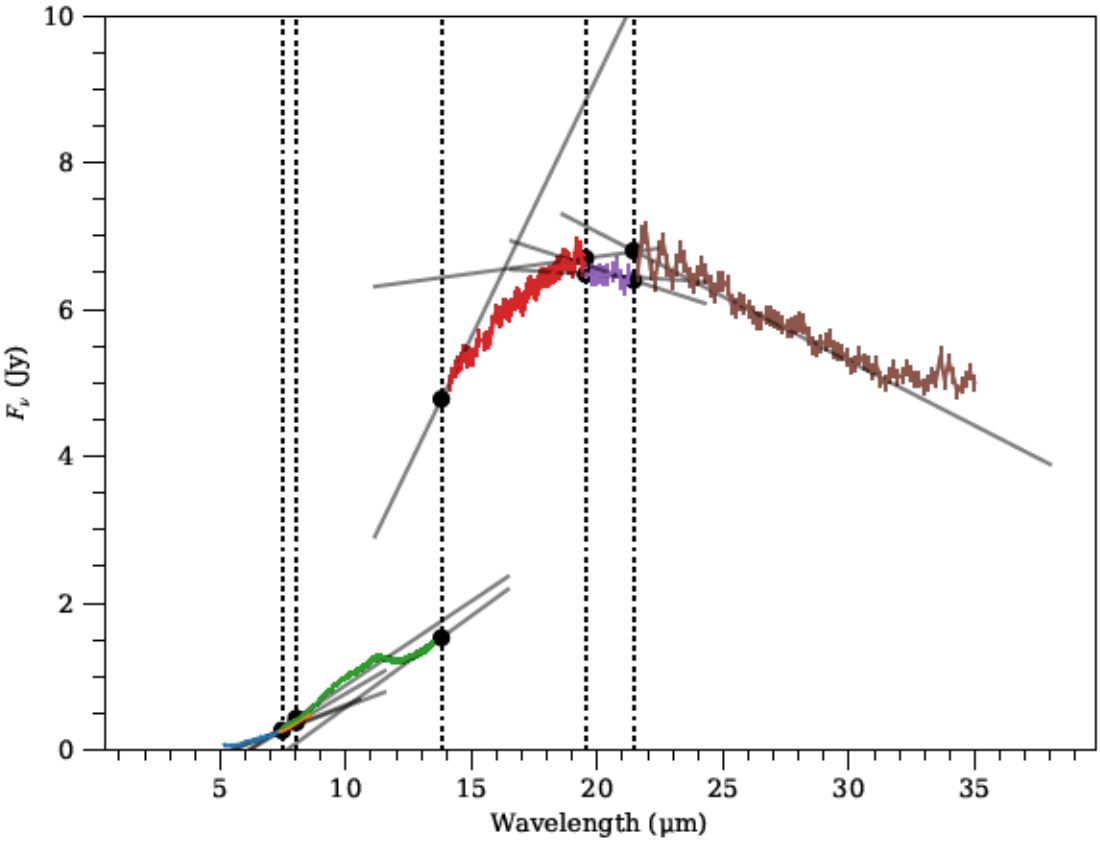

Figure 3: Following Fig. 2, order-to-order scaling factors are derived with linear fits (gray lines) to the edges of each order (data points with error bars). The neighboring orders are scaled based on the extrapolations at a common wavelength (marked with black circles).

3.2.6 Order-to-order scaling

Due to telescope jitter, order-to-order calibration uncertainties, the subtle effects of observing extended sources, the variations of aperture size by IRS module, and ephemeris uncertainties, the combined spectra are rarely continuous in flux density. To account for order-to-order offsets, we extrapolate neighboring orders to a common wavelength and compute a scale factor based on the ratio of the extrapolated flux densities. Either the SL1 or LL1 orders are typically used as the spectral flux reference. The derived scale factors are provided in each data table, and the reference order will have a scale factor of 1.0 at all wavelengths. Unusually large scale factors caused us to reconsider the spectral order trimming (Section 3.2.3), as poorly calibrated or bad data near the order edges can affect the order-to-order scale factor estimates. The derivation of the scale factors is demonstrated in Fig. 3.

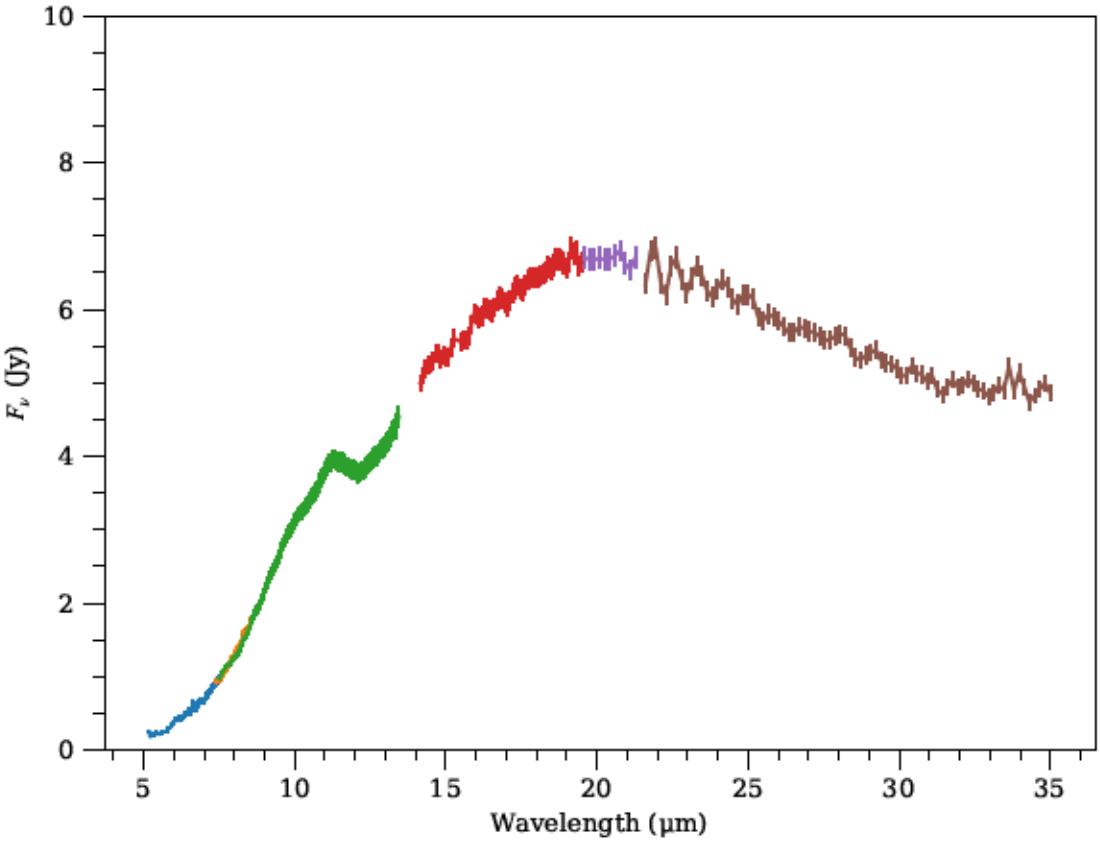

Figure 4: Following Fig. 3, the order-to-order scale factors are applied producing the final spectrum.

3.2.7 Spectral uncertainties

The IRS pipeline provides an estimate of the spectral uncertainties, based on Poisson noise, read noise, and calibration file uncertainties. However, the uncertainties tend to be too small for very high SNR spectra, and need to be augmented. We follow the approach used to generate the *Spitzer* Heritage Archive's IRS enhanced data products: (1) all uncertainties must be at least 0.1 mJy (Table 9.2 of the IRS Instrument Handbook); and (2) based on the repeatability of primary standard star HR 7341, an additional 1.1–1.8% uncertainty is added in quadrature to account for "additional sources of photometric noise, such as slit-loss or flat field noise." The final spectrum for our 9P/Tempel 1 example is shown in Fig. 4.

4 Known Issues and Caveats

Users should consult with Chapter 7 of the IRS Instrument Handbook (Spitzer Science Center 2012) for a description of all IRS data features and artifacts.

4.1 Spectral fringing

Spectral wiggles are present in our final LL data, likely due to optical fringing. The amplitude is $\sim$ 10% or less. Take caution when interpreting spectral features in the LL module, especially at 21–25 µm (e.g., Fig. 4).

4.2 14-µm teardrop

The SL1 module is affected by an artifact named the 14-µm teardrop. The artifact is an enhancement in the spectral flux densities of this module at >13.5 µm. The name "teardrop" refers to the asymmetric spatial distribution of light in the focal plane. It is potentially the result of an internal reflection. There is no reliable correction for this feature. We avoid the artifact by trimming our SL1 spectra at 13.5 µm, which results in a gap between the SL and LL spectral modules.

4.3 Gas emission

Emission from gas species was generally not considered during the data processing, and isolated emission lines, if they exist, may have been inadvertently removed. However, the ν_2 vibrational water band at 6-µm (Woodward et al. 2007; Bockelée-Morvan et al. 2009) is present in many spectra and should be preserved. Other gas species are undetectable or have yet to be identified.

4.4 Effective field-of-view, exposures, and integration time

The effective field-of-view, number of exposures, and integration time varies by module. The PDS4 label includes a `Spectral_Characteristics` class that summarizes these parameters for each spectrum. `Observation_Parameters/number_of_exposures` and `Observation_Parameters/net_integration_time` provide the total number of exposures and total integration time summed over all modules included in the spectrum.

The meaning of the `Field_of_View` class depends on the processing history and modules used. The given field-of-view is that of the reference slit in the order-to-

order scaling step (Section 3.2.6). For example, the spectrum of comet 48P was scaled holding the LL1 order fixed, therefore the field-of-view in the label is 11″×52″.

4.5 Spectral shape from 19 to 23 μm

The 19–23-μm wavelength region may contain spectral peaks from Mg-rich crystalline olivine (e.g., forsterite), which are seen clearly in our 17P/Holmes spectrum (Fig. 13). The strength of these peaks can vary between comets, which is directly related to the coma grain properties (e.g., abundance). However, we caution the user that the IRS spectra near this region are challenging to reduce. The region spans three different spectral segments: the long wavelength end of LL2 (< 21.3 μm), the full LL3 segment (19.2–21.6 μm), and the short wavelength end of LL1 (> 19.9 μm). Rarely do the flux densities for these segments agree with each other. The primary issues are a roll-off in sensitivity on the long wavelength end of LL2, and the strong spectral fringing on the short wavelength end of LL1. In general, the flux density falls with increasing wavelength in the LL2 module, suggesting a peak near 19 μm, but the LL3 segment tends to be flat over the same spectral range. Thus, choices made in the trimming of the edges of the spectral orders affects the shape of the final spectrum, depending on if one favored the LL2 or LL3 segments. In our reduction, we tended to favor LL3 over LL2. The presence and strengths of the 19.5-μm and other spectral features need to be taken with caution and in consideration with other resonances expected for the same mineral (e.g., Campins & Ryan 1989; Crovisier et al. 1997; Koike et al. 2003).

5 Data Notes by Target

5.1 6P/d'Arrest

We subtract a model nucleus with a 2.23-km radius based on the work of Fernández et al. (2013).

5.2 8P/Tuttle

The IRS observation of comet 8P/Tuttle was first analyzed by Groussin et al. (2019), extracted with a point-source (tapered) aperture. We re-reduce this data set for consistency within our survey, using fixed-width apertures. The nucleus is bilobed (Harmon et al. 2010), and appears to be two spheres in contact (Groussin et al. 2019).

We model the nucleus with an effective radius of 2.92 km, based on the total area of the two spheres (radii 2.7 and 1.1 km; Groussin et al. 2019).

5.3 9P/Tempel 1

The pre- and post-*Deep Impact* spectra of 9P/Tempel 1 were first presented by Lisse et al. (2006). Kelley & Wooden (2009) re-reduced the data and subtracted a model of the nucleus to properly enhance the dust spectral features. We re-reduce the data a second time to update it to the latest IRS reduction pipeline and for consistency within our survey. As noted above, we only present the pre-*Deep Impact* spectra.

A model nucleus was subtracted from the data, using the effective radius of 3.3 km, as measured through *Spitzer*/IRS spectra and imaging by Lisse et al. (2005).

5.4 17P/Holmes

The spectra of comet 17P/Holmes were first presented by Reach et al. (2010). The SL and LL data presented here are reprocessed in the same manner as our other spectra for survey consistency. The spectra were taken 18.5 days after the mega-outburst that occurred on 2007 October 23.3 UT (Hsieh et al. 2010).

The background data for this observation are from a dedicated observation request, offset from the comet.

The shape of the short wavelength edge of the silicate feature and the 6 to 7-μm region suggest an absorption feature at these wavelengths. However, residual background may be present in the spectrum, perhaps related to stray light from the peak up arrays in the SL module. This aspect is difficult to assess due to the large extent of the coma with respect to the IRS fields-of-view. We caution the user against strong conclusions based on this spectral range without further investigation.

5.5 21P/Giacobini-Zinner

The ephemeris position of the comet is coincident with the peak of the brightness in the SL and LL spectral maps. However, note that this peak is at the edge of the SL map. Furthermore, the LL positions in the slit are far from the nominal IRS stare locations (Spitzer Science Center 2012). The spectral shape in the 20 μm region is an outlier in our survey, and we suspect this is due to the pointing offset. We caution the user against strong conclusions in this spectral range without further analysis. The data is still calibrated assuming a point source spatial distribution (Section 3.2.5).

5.6 29P/Schwassmann-Wachmann 1

The spectrum was first published by Stansberry et al. (2004), and further analyzed by Schambeau et al. (2015). For consistency with our survey, we have reprocessed the data and include the results in our data set.

We use the nucleus model parameters from Schambeau et al. (2015): radius R=30.2 km, and NEATM infrared beaming parameter $\eta = 0.99$. At 8, 13, 15, and 30 μm, this model accounts for 55%, 75%, 40%, and 40% of the flux in our spectrum, respectively. Therefore, the shape of the SL portion of the spectrum ($\lambda < 14$ μm) is strongly affected by the adopted nucleus model. The IRS data and the *Spitzer* imaging on which the nucleus parameters are derived were non-contemporaneous (separated by 6 hr to 2 days). We cannot account for any cross-sectional variations due to rotation of the nucleus, which will affect the shape of the spectrum. However, we include the spectrum in our survey because of it's high SNR and abundant spectral features from silicate dust species.

5.7 37P/Forbes

The background (shadow) observation was taken about a year after the prime data. Increasing the background flux densities by 8% reduced background residuals.

There are substantial gaps in the SL2 spectrum due to bad data. Take caution interpreting any features in this spectral range. A low data point is present at 8.1 μm. This is an unusual feature, but since it is present in both the SL2 and SL3 data, we have preserved it in the spectrum.

5.8 41P/Tuttle-Giacobini-Kresák

The spectral map is not centered on the comet. The ephemeris position is approximately 8″ from the map edge. Therefore, we calibrated the data as an extended source, applying the slit-loss correction function (Section 3.2.5).

5.9 46P/Wirtanen

We use the optically derived nucleus effective radius from Lamy et al. (1998), R=0.6 km for all five epochs. The model accounts for 6–15% of the flux density at 5.5 μm for the spectra inside of 2 au, and 16% of the flux density at 7.5 μm for the spectrum at 2.1 au.

5.10 48P/Johnson

There is no background or shadow observation for the SL data (only SL1 was used). We searched the *Spitzer* Heritage Archive for SL1 spectra taken close in time, but found none that were suitable. Instead, the spatial distribution of the coma along the SL slit is narrow enough that the two nod positions can be subtracted from each other without any overlap inside our 9.7-pixel wide aperture. We subtracted a model nucleus using a radius of 2.97 km from Fernández et al. (2013).

The two SL nod positions in this Spectral Stare differ at the 20% level, suggesting that the comet was not well-centered in the slit narrow dimension. The spectra data were averaged together after scaling to remove the difference, as described in Section 3.2.6.

5.11 62P/Tsuchinshan 1

This spectral map is sparse, with 7.2″ steps in a direction perpendicular to the slit. The brightest SL spectra are 5″ off from the comet's ephemeris position. We did not subtract a nucleus from the spectrum. In addition, we calibrated the data as an extended source, applying the slit-loss correction function (Section 3.2.5).

The spectrum has an unusual local minimum near 7.7 μm, but the SL2 and SL3 data trend together and give some confidence that it may be real.

5.12 65P/Gunn

There is no suitable background observation taken with these data. We searched the *Spitzer* Heritage Archive for other data that may be used as a background subtraction. A dedicated background stare accompanying an observation of NGC 628 was used for SL (AOR ID 9502208) and the in-scene LL backgrounds taken in an observation of NGC 660 (AOR ID 9070848) were used after scaling each by a factor of 0.9.

5.13 67P/Churyumov-Gerasimenko

For the nucleus of this comet, we used the NEATM model parameters of Kelley et al. (2009), R=2.04 km, η=0.7. The benefit to using these parameters rather than results from the *Rosetta* mission is that they are based on *Spitzer* data taken at similar wavelengths.

The observation at 2.8 au was not centered on the comet. The SL slit missed the comet by 4.5″, and lacked any appreciable signal, but the comet was covered by the

LL slit. Only the LL spectrum is presented, after subtracting the model nucleus.

5.14 71P/Clark

This data was previously examined for emission from water, polycyclic aromatic hydrocarbons, and carbonates by Bockelée-Morvan et al. (2009). We re-reduce the data for survey consistency.

Bockelée-Morvan et al. (2009) found that the SL map missed the nucleus by 8″. We did not subtract a model nucleus spectrum from the data. In addition, we calibrated the SL data as an extended source, applying the slit-loss correction function (Section 3.2.5).

5.15 73P/Schwassmann-Wachmann 3

Spitzer spectra of fragments B and C of this comet were studied by Sitko et al. (2011). We include the Spectral Stare observations in our survey, re-reduced for consistency. A second observation of each nucleus was taken 4 to 5 months after the first observations. They are also included in our survey.

The LL module partially saturated in all observations except for fragment B at 1.3 au. Therefore, LL is only kept in the 1.3 au spectrum.

5.16 78P/Gehrels 2

The off-source LL1 data include some coma from this bright comet, and the SL1 data have no accompanying background observation. We use SL and LL sky background from a nearby observation (AOR ID 5297152). The SL background is scaled by 0.94 and the LL background is scaled by 0.95. We subtract a model nucleus based on a 1.35-km effective radius from Fernández et al. (2013).

5.17 88P/Howell

Similar to 78P/Gerhels 2, the LL1 background is coma contaminated, and there is no background for SL1. We use SL and LL sky background from a nearby observation (AOR ID 5297152, the same as for 78P/Gerhels 2). The background observation was scaled by 0.90 to match the apparent in-scene background.

5.18 105P/Singer Brewster

The extracted SL2 spectrum had an usual shape (approximately flat in flux per unit frequency space), potentially due to residual background in the data. We searched the *Spitzer* Heritage Archive for nearby background observations, but did not find any suitable replacements. Therefore, we omitted the SL2 data from the final spectrum.

5.19 121P/Shoemaker-Holt 2

We subtracted a model nucleus with an effective radius of 3.87 km (Fernández et al. 2013). The spectrum is 50% nucleus at 7.5 μm. The SL2 data, with very low SNRs, were omitted.

5.20 123P/West-Hartley

The LL1 off-source pointing was contaminated by coma, so a nearby background was found in the *Spitzer* Heritage Archive (AOR ID 4169216). We subtracted a model nucleus radius of 2.18 km from Fernández et al. (2013). The SL spectrum has a very low SNR and was omitted.

5.21 132P/Helin-Roman-Alu 2

We subtracted a model nucleus using a radius of 0.81 km (Fernández et al. 2013). The model accounts for 50% of the observed flux at 8 μm.

5.22 144P/Kushida

The peak brightness for this comet occurs at the edge of the spectral map. This is confirmed with the ephemeris position, which is approximately 1/2 an SL slit width from the center of the peak pixel. The data are calibrated assuming a point source spatial distribution (Section 3.2.5).

5.23 C/2001 Q4 (NEAT)

The SL1 off-source pointing includes some coma. We use a nearby observation from the *Spitzer* Heritage Archive (AOR ID 9833728) for background subtraction.

5.24 C/2003 K4 (LINEAR)

As described by Woodward et al. (2007), the observation at 1.76 au is a sparse Spectral Map, not centered on the comet. We extracted spectra from the brightest pointing, and calibrated it as an extended source, applying the slit-loss correction function (Section 3.2.5). For the background, we used a nearby observation (AOR 4733952).

The background (shadow) observation at 4.50 au was taken a year after the prime data. The background data needed to be scaled by unusually low values to avoid over subtraction: 0.65 for SL and 0.81 for LL.

5.25 C/2003 T3 (Tabur)

The SL2 data were omitted due to low SNR.

5.26 C/2003 T4 (LINEAR)

The SL shadow observation at 3.5 au has a gradient that adversely affects the SL2 data. We omitted the SL2 data from this epoch.

At 4.6 au, strong latent charge was present in the SL shadow observation. We omitted the SL data from this epoch.

5.27 C/2004 B1 (LINEAR)

Similar to 71P/Clark, the spectra of comet C/2004 B1 at 2.2 and 2.1 au were studied by Bockelée-Morvan et al. (2009). They are re-reduced and included this data set. We omitted the SL2 data from the spectrum at 2.6 au, due to strong residual background flux.

5.28 C/2004 Q2 (Machholz)

The comet is at the edge of this Spectral Map, but the ephemeris position is within the peak pixel, therefore we calibrate the data as a point source (Section 3.2.5). The background is noisy and is over subtracted in SL2. We offset the SL2 and SL3 spectra by a constant factor (4 mJy) to help mitigate the issue. The results have good agreement with the SL1 spectrum.

5.29 C/2006 P1 (McNaught)

Harker et al. (in prep.) identified a point source as the comet nucleus in *Spitzer*/MIPS 24-μm images at 6.4 and 7.9 au. They estimate the effective radius to be 3.8 km. We adopt this radius and subtract a model nucleus from our spectra.

At 2.4 au, the nucleus accounts for about 20% of the SL2 spectral flux. At 3.6 au, the nucleus is up to 50% of the SL2 spectral flux, but the data have a low SNR and are omitted from the final spectrum. At 4.0 au, the nucleus accounts for 100% of the SL1 spectral flux at 8 μm, and 25% at 13 μm. For the wider-slit LL2 data, the fraction drops to 8% at 14 μm.

5.30 C/2006 Q1 (McNaught)

The SNR of the SL2 spectrum at 3.1 au is very low, therefore we omitted it from the final spectrum.

5.31 C/2007 N3 (Lulin)

This observation was originally analyzed by Woodward et al. (2011). Here, we reprocessed the data for survey consistency.

5.32 C/2008 T2 (Cardinal)

Nothing to note.

Acknowledgments

Support for this work was provided by the NASA Emerging Worlds program grant NNX16AD33G, and NASA Solar System Observations program grant 80NSSC19K0868. Support for this work was also provided by NASA through a awards issued by JPL/Caltech.

This work is based on observations made with the Spitzer Space Telescope, which is operated by the Jet Propulsion Laboratory, California Institute of Technology under a contract with NASA.

This research made use of Tiny Tim/Spitzer, developed by John Krist for the Spitzer Science Center. The Center is managed by the California Institute of Technology under a contract with NASA.

Production of this data set also benefited from SAOImage DS9 (Joye & Mandel 2003), Astropy (Astropy Collaboration et al. 2013, 2018), and Reproject (Robitaille et al. 2020).

A Spectral Map Reconstruction Artifacts

Observations taken in IRS Spectral Mapping mode may be processed with the CUbe Builder for IRS Spectra Maps (CUBISM) software. Refer to Smith et al. (2007) for details on CUBISM and generating spectral maps from long-slit spectroscopy. One point regarding the observational design of the spectral map is particularly relevant for this cometary data set. The choice of spatial offsets of the telescope has a consequence on the ability for CUBISM to reconstruct the spatial-spectral scene. Smith et al. (2007) recommends a step size of 1/2 the slit width (1.85″) along the dispersion direction. However, many of the cometary spectral maps were executed with larger step sizes.

Early on in creating this data set, we reduced Spectral Map observations into data cubes, and extracted 1-dimensional spectra around the inner coma. The reduction of the Spectral Maps is similar to the process described in Section 3.2, but with an important exception: instead of spectral extraction with SPICE, the BCDs were processed with CUBISM and spectra extracted from the spatial-spectral data cubes. CUBISM produces spectral cubes on a module-by-module basis. The results were re-sampled onto a common spatial grid with the Python module `reproject` using a flux-conserving spherical polygon intersection technique, processing one spectral slice at a time.

Spectra were extracted from the re-projected data cubes within box apertures 18″ to 20″ wide along the slit's spatial direction, similar to our default SL aperture width. The aperture sizes perpendicular to the slit are limited by each observation's mapping strategy, and are typically no more than a couple slit widths across ($\lesssim 8''$). When the LL module is also used in mapping mode, we use the same aperture as for SL. The one exception is the observation of 17P/Holmes, which was large enough for us to use a circular aperture.

Based on these results, for this archive, we chose to abandon CUBISM and process all data as Spectral Stares using SPICE. We found that processing most of these data using CUBISM introduced substantial artifacts in some spectra. In Fig. 5, we compare spectra of comets 17P/Holmes, 21P/Giacobini-Zinner, 37P/Forbes, and 71P/Clark processed as Spectral Maps using CUBISM to the same data processed as

Spectral Stares using SPICE (Section 3.2). Spectral features are consistent between the two approaches for the 17P/Holmes data. However, the effective temperature of the spectrum is warmer in the map reduction, possibly due to CUBISM's default extended source calibration versus our point source calibration (Section 3.2.5). The spectral map reductions for 21P/Giacobini-Zinner and 37P/Forbes introduced a local peak near 16 μm and minimum near 18 μm, which are not seen in the Spectral Stare reduction of any other comet (note the 16-μm forsterite peak in the comet Holmes spectrum produces a spectral minimum near 17 μm). The spectral map approach using CUBISM for 71P/Clark yields a concave spectral shape at 20–35 μm.

The agreement between the two approaches for the comet 17P/Holmes spectra is consistent with the fact that the Holmes map used an optimal mapping strategy (1/2 slit-width step size in the dispersion direction). In contrast, the three other comets used a map strategy with a 2.5″ step size in the dispersion direction (2/3 slit). It is likely that the spectra from each pointing of the telescope are good, but using spectral maps and CUBISM to reconstruct a spatial-spectral data cube introduces spurious features. In summary, to avoid these issues for this archive, we reduce all observations, whether taken as part of a Spectral Map or Stare, as Spectral Stare observations (Section 3.2).

B Slit Losses and Cometary Comae

IRS observations of point sources have significant losses because the narrow slit dimension is similar to the diffraction limit of the instrument. The IRS pipeline's slit-loss correction factor is a description of the losses due to the narrow slit masking, i.e., the losses when the slit is narrower than the bulk of the PSF. For SL1, the point-source losses range from 17% to 36% for 5 to 14 μm, respectively. The losses are built into the IRS calibration, i.e., they are automatically accounted for in all observations of point sources. However, extended sources do not have the same slit losses. For an infinitely uniform extended source, the slit losses are 0 at all wavelengths. Thus, spectra of such extended sources processed with the IRS pipeline will unnecessarily change the spectral shape, since the point-source slit losses are built into the calibration. To remove this spectral dependence, the IRS pipeline provides the so-called "slit-loss correction function," which retrieves the original spectral energy distribution of the planar extended source, with an accuracy of ∼10%.

Comet comae tend to have spatial distributions that are intermediate to that of a point source, and that of a smoothly varying extended source. For a nominal

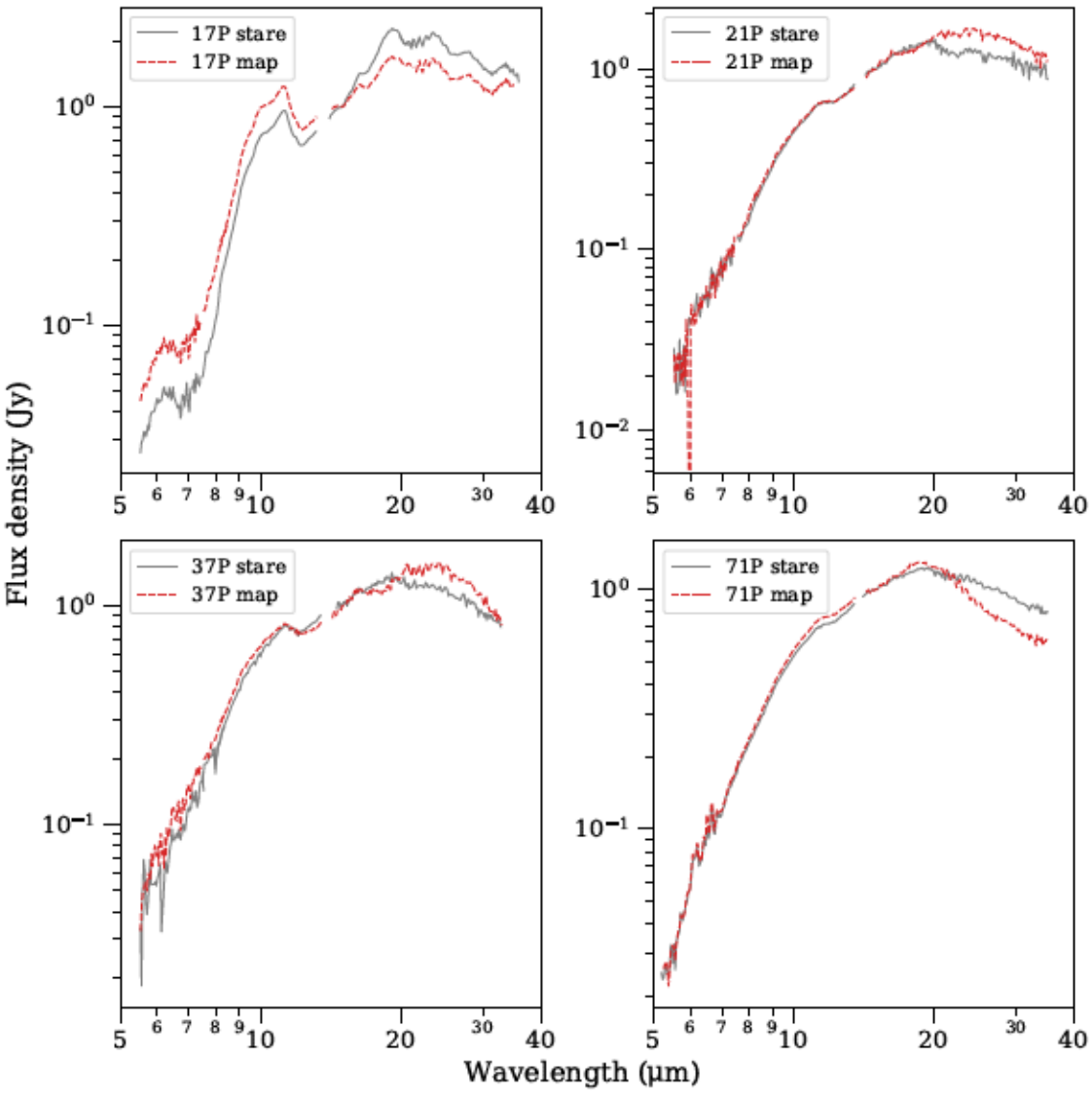

Figure 5: Comparison of spectra derived from single pointing using SPICE (Spectral Stare, solid lines) to those derived from a reconstructed Spectral Map using CUBISM (dashed lines). See the text for detailed discussion of the differences.

coma (isotropic and in free expansion), the surface brightness distribution varies as $1/\rho$, where ρ is the projected distance to the (unresolved) nucleus. When such a distribution is observed with a telescope, the inner core has the shape of the PSF, which quickly transitions to a $1/\rho$ surface brightness distribution as ρ increases.

Previous studies of comet comae with IRS have assumed the extended source case and applied the pipeline's slit-loss correction function (Kelley et al. 2006; Woodward et al. 2007; Bockelée-Morvan et al. 2009; Reach et al. 2010; Sitko et al. 2011; Woodward et al. 2011). We will demonstrate that it is more appropriate to assume the

slit-losses for a point source than an extended source for Spectral Stare observations with the coma centered in the slit's narrow dimension. We will also show that the slit loss correction function should be applied to Spectral Stare observations offset into the coma (i.e., not centered on the nucleus).

B.1 Slit centered on the comet

To examine the slit losses for a comet observed with IRS, we created PSFs for the IRS SL1 order from 5.2 to 14.0 μm. The PSFs were generated using the STinyTim software at a grid spacing of 0.12″/pix (native pixel size is 1.8″). The STinyTim model for IRS only accounts for the telescope optics up to the entrance slit, which is appropriate for our purposes. We generated five models: (1) a point source, $I \propto \delta(x, y)$, where I is surface brightness and δ is the Dirac delta function; (2) a nominal coma, $I \propto \rho^{-1}$; (3) a distant comet, with a morphology dominated by radiation pressure, $I \propto \rho^{-1.5}$; (4) a coma with extreme dust fragmentation, $I \propto \rho^{-0.5}$, and (5) a large (180″×180″) and uniform extended source, $I \propto 1$. We convolved each model with our set of PSFs, and masked regions outside of a 3.7″×17.5″ region corresponding to the slit width × our nominal constant-width extraction aperture. To compute the slit losses, we summed the total flux passing through the slit, and divided by the total flux passing through the slit in the absence of the telescope optics (i.e., before convolution). The results are plotted in Fig. 6.

Our results for a point source are offset by ≈ 5% from the IRS pipeline values. However, we will focus on the trends, especially how much the throughput affects the shape of a comet spectrum, rather than the absolute level. To that end, we simulate IRS spectra of a blackbody source with a spectral shape similar to that from a comet coma. We use a temperature of 250 K, and multiply the spectrum by the slit throughput for the distribution under study (e.g., a $1/\rho$ coma), then divide by the slit throughput for a point source. The last step is implicitly included in the IRS pipeline calibration. Figure 7 shows the true spectrum, and those that would arise if the calibration process assumed a point source or an extended source, and Fig. 8 shows the shape error as a percent difference from the true spectrum.

For the typical coma cases, ρ^{-1} and $\rho^{-1.5}$, assuming a point source distribution results in an error of only ≈ 5%, whereas assuming a large extended source is up to 15% in error. The situation is reversed for the extreme fragmentation coma, $\rho^{-0.5}$; here, assuming the large extended source calibration results in a truer spectrum. We conclude that the assumption that the coma is a point source is sufficient for a

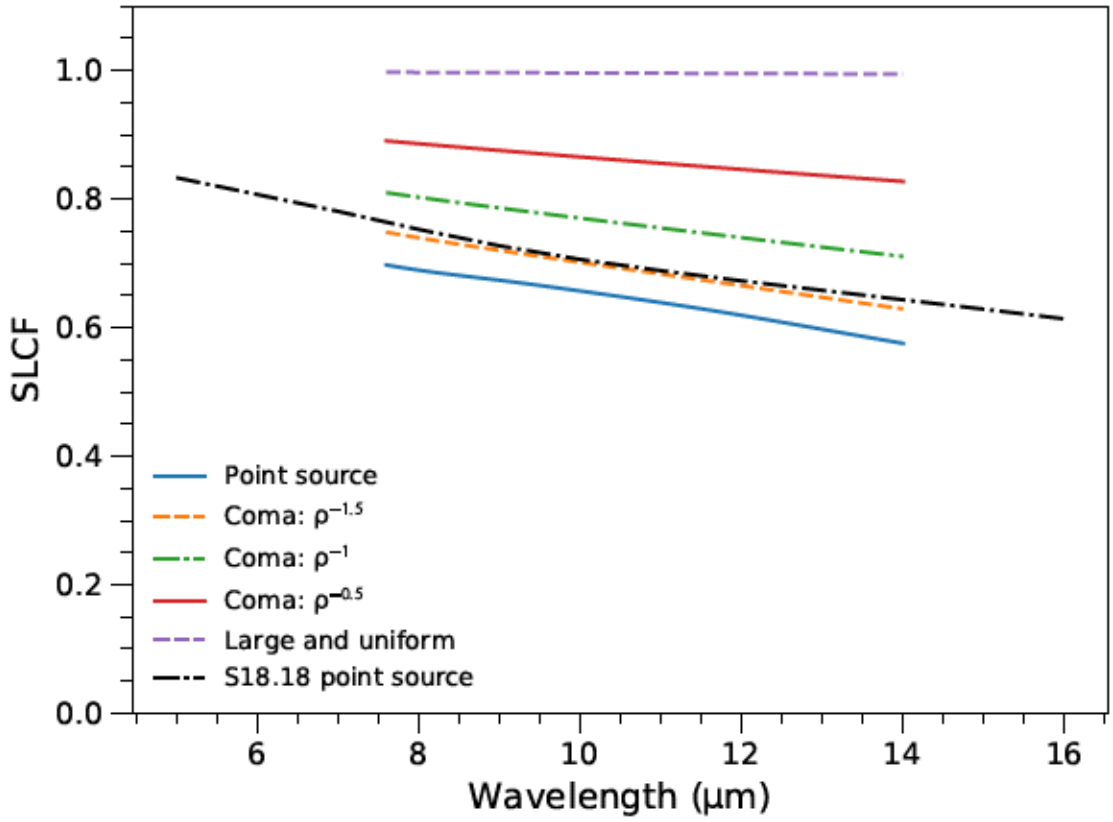

Figure 6: Fraction of energy entering the slit for three coma shapes ($\rho^{-1.5}$, ρ^{-1}, and $\rho^{-0.5}$), a large and uniform extended source, an infinitely uniform extended source, and a point source, as computed through our convolution tests. This fraction is commonly called the slit-loss correction function (SLCF). The SLCF of a point source from the IRS pipeline version S18.18 is also shown.

narrow-slit observation when that slit is centered on the peak of the coma.

B.2 Offset spectra

Similar to the tests above, we generated a ρ^{-1} coma and offset our synthetic slit 5″ into the coma (offset parallel to the narrow slit dimension). After convolution with the IRS PSFs, we find that the spectral shape from an extended source calibration is consistent within 1% of the ideal case, whereas calibrating for a point source results in errors up to 20% (Fig. 9). Spectral observations of isotropic comae offset away from the nucleus are best calibrated assuming the extended source case.

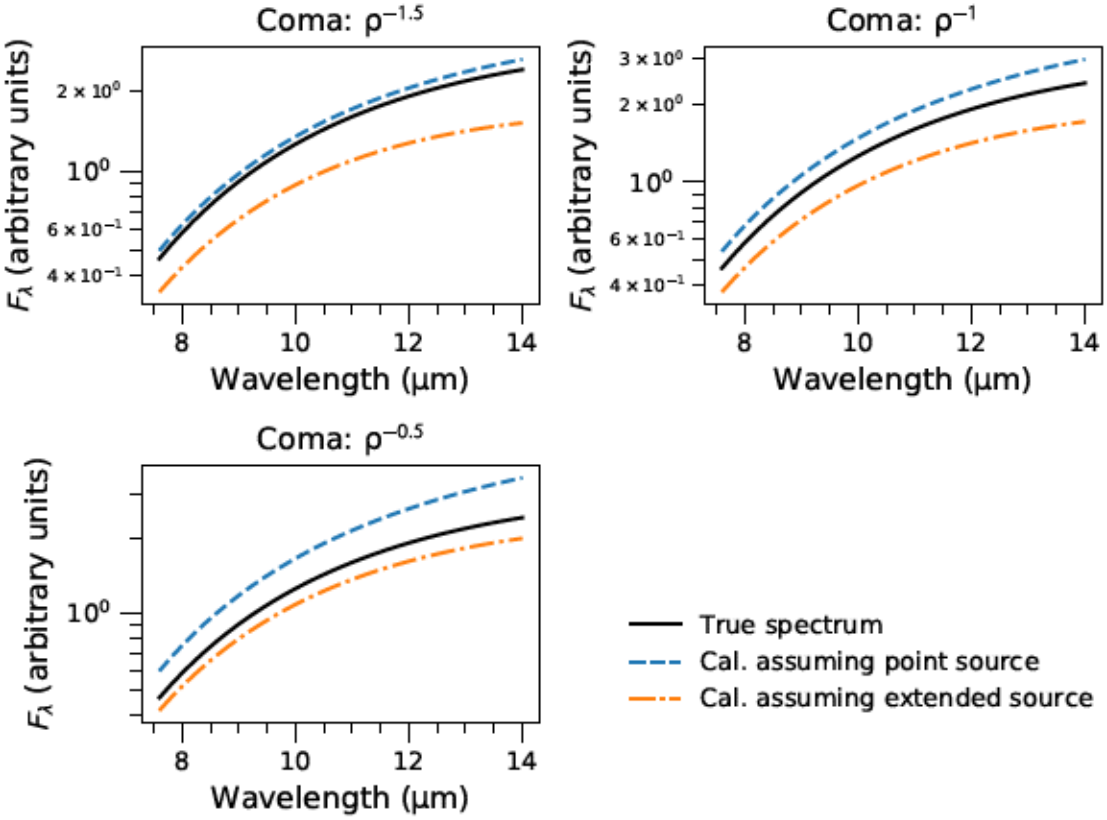

Figure 7: Nominal blackbody spectrum (250 K) of a comet coma (solid lines), as observed by the IRS and calibrated assuming either the brightness distribution is that of a point source (dash-dotted lines), or a large and uniform extended source (dashed-lines). The three model comae are: $I \propto \rho^{-1.5}$, ρ^{-1}, $\rho^{-0.5}$.

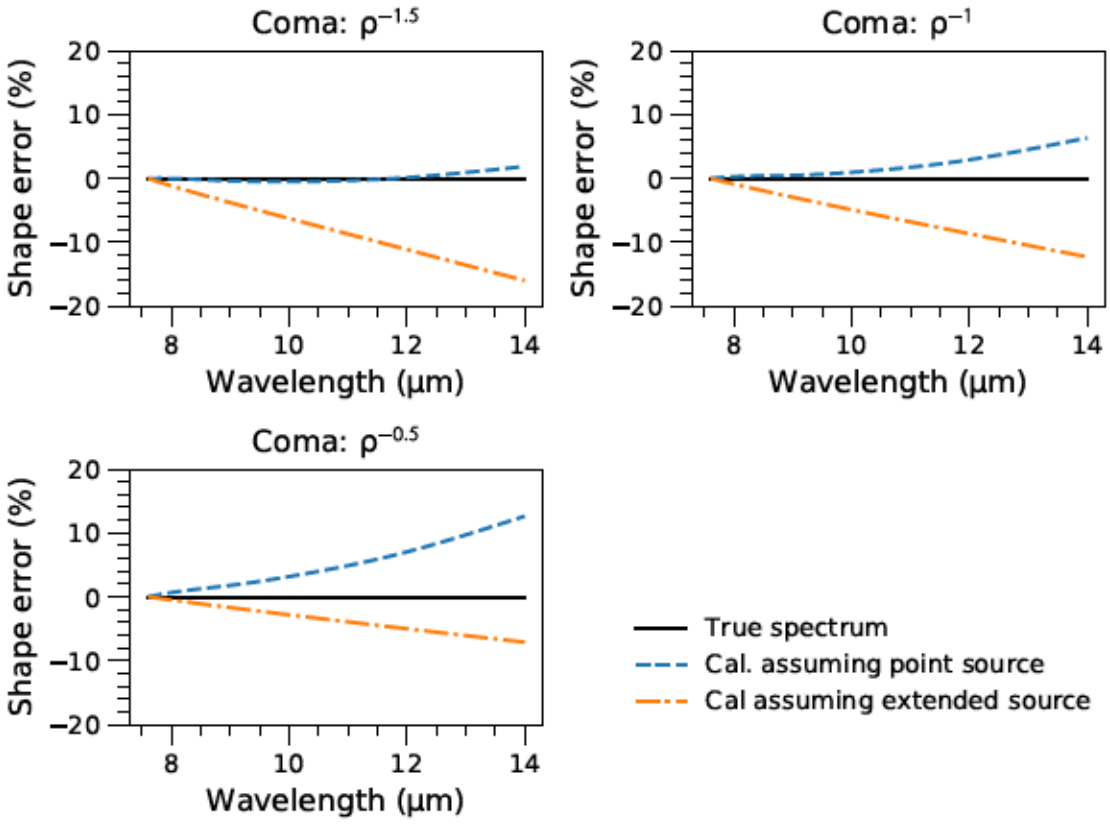

Figure 8: Percent spectral error based on Fig. 7.

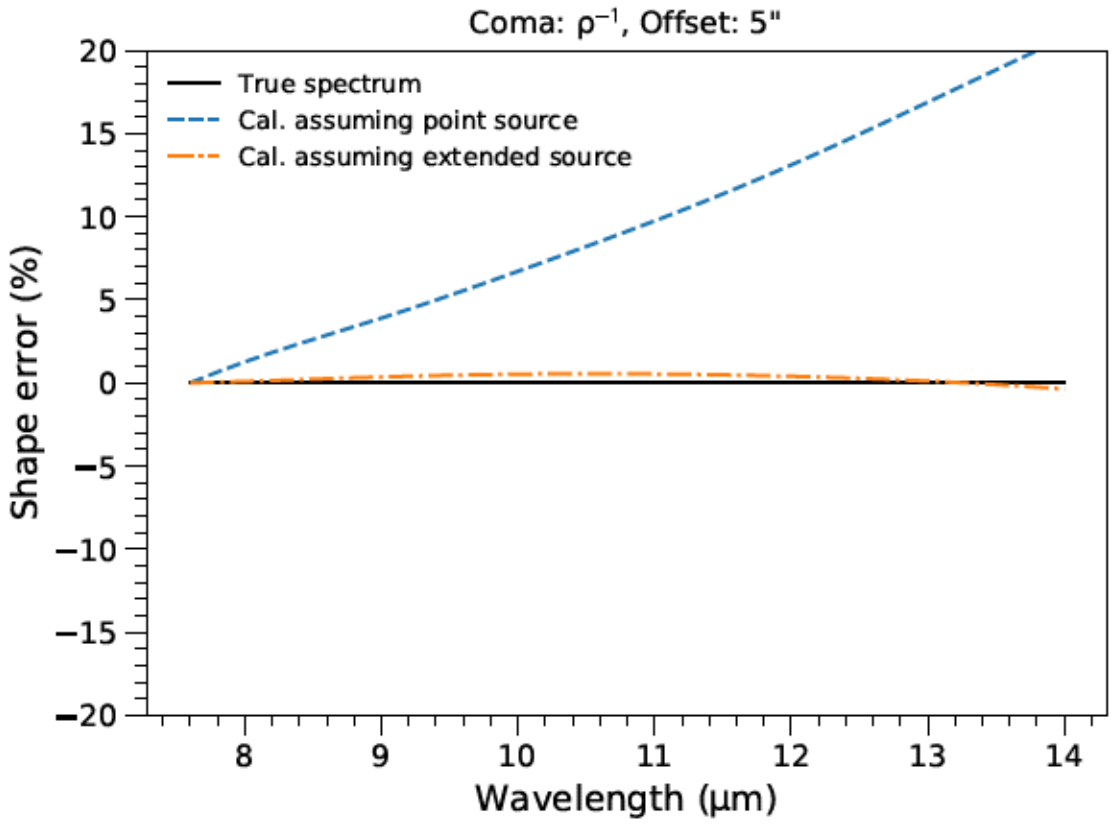

Figure 9: Percent spectral error for a ρ^{-1} coma and a 5″ offset from the peak surface brightness.

C Comet Spectra

All cometary spectra are plotted by target in Figs. 10–42. Spectra are displayed as λF_λ vs. λ on a log-log scale to better emphasize all spectral features and those wavelengths that dominate the emitted thermal energy. Some spectra are offset by a constant scale factor for clarity, as noted in the figure legends.

References

Astropy Collaboration et al. 2013, Astropy: A community Python package for astronomy, Astron. Astrophys., 558, A33

—. 2018, The Astropy Project: Building an Open-science Project and Status of the v2.0 Core Package, Astron. J., 156, 123

Bockelée-Morvan, D., Woodward, C. E., Kelley, M. S., & Wooden, D. H. 2009, Water in Comets 71P/Clark and C/2004 B1 (Linear) with Spitzer, Astrophys. J., 696, 1075

Brownlee, D. 2014, The Stardust Mission: Analyzing Samples from the Edge of the Solar System, Annu. Rev. Earth Planet. Sci., 42, 179

Campins, H., & Ryan, E. V. 1989, The identification of crystalline olivine in cometary silicates, Astrophys. J., 341, 1059

Crovisier, J., Leech, K., Bockelee-Morvan, D., Brooke, T. Y., Hanner, M. S., Altieri, B., Keller, H. U., & Lellouch, E. 1997, The spectrum of Comet Hale-Bopp (C/1995 O1) observed with the Infrared Space Observatory at 2.9 AU from the Sun, Science, 275, 1904

Fernández, Y. R., et al. 2013, Thermal properties, sizes, and size distribution of Jupiter-family cometary nuclei, Icarus, 226, 1138

Groussin, O., Lamy, P. L., Kelley, M. S. P., Toth, I., Jorda, L., Fernández, Y. R., & Weaver, H. A. 2019, Spitzer Space Telescope observations of bilobate comet 8P/Tuttle, Astron. Astrophys., 632, A104

Hanner, M. S., Aitken, D. K., Knacke, R., McCorkle, S., Roche, P. F., & Tokunaga, A. T. 1985, Infrared spectrophotometry of Comet IRAS-Araki-Alcock (1983d): a bare nucleus revealed?, Icarus, 62, 97

Hanner, M. S., Giese, R. H., Weiss, K., & Zerull, R. 1981, On the definition of albedo and application to irregular particles, Astron. Astrophys., 104, 42

Harker, D. E., Kelley, M. S. P., Woodward, C. E., & Wooden, D. H. in prep., Dust Properties of Comets Observed by *Spitzer*

Harmon, J. K., Nolan, M. C., Giorgini, J. D., & Howell, E. S. 2010, Radar observations of 8P/Tuttle: A contact-binary comet, Icarus, 207, 499

Harris, A. W. 1998, A Thermal Model for Near-Earth Asteroids, Icarus, 131, 291

Houck, J. R., et al. 2004, The Infrared Spectrograph (IRS) on the Spitzer Space Telescope, Astrophys. J., Suppl. Ser., 154, 18

Hsieh, H. H., Fitzsimmons, A., Joshi, Y., Christian, D., & Pollacco, D. L. 2010, SuperWASP observations of the 2007 outburst of Comet 17P/Holmes, Mon. Not. R. Astron. Soc., 407, 1784

Joye, W. A., & Mandel, E. 2003, New Features of SAOImage DS9, in Astronomical Society of the Pacific Conference Series, Vol. 295, Astronomical Data Analysis Software and Systems XII, ed. H. E. Payne, R. I. Jedrzejewski, & R. N. Hook, 489

Keller, H. U., & Kührt, E. 2020, Cometary Nuclei—From Giotto to Rosetta, Space Sci. Rev., 216, 14

Kelley, M., Woodward, C. E., Gehrz, R. D., Reach, W. T., & Harker, D. E. 2017, Mid-infrared spectra of comet nuclei, Icarus, 284, 344

Kelley, M. S., & Wooden, D. H. 2009, The composition of dust in Jupiter-family comets inferred from infrared spectroscopy, Planet. Space Sci., 57, 1133

Kelley, M. S., Wooden, D. H., Tubiana, C., Boehnhardt, H., Woodward, C. E., & Harker, D. E. 2009, Spitzer Observations of Comet 67P/Churyumov-Gerasimenko at 5.5-4.3 AU from the Sun, Astron. J., 137, 4633

Kelley, M. S., et al. 2006, A Spitzer Study of Comets 2P/Encke, 67P/Churyumov-Gerasimenko, and C/2001 HT50 (LINEAR-NEAT), Astrophys. J., 651, 1256

Koike, C., Chihara, H., Tsuchiyama, A., Suto, H., Sogawa, H., & Okuda, H. 2003, Compositional dependence of infrared absorption spectra of crystalline silicate. II. Natural and synthetic olivines, Astron. Astrophys., 399, 1101

Kokotanekova, R., et al. 2017, Rotation of cometary nuclei: new light curves and an update of the ensemble properties of Jupiter-family comets, Mon. Not. R. Astron. Soc., 471, 2974

Lamy, P. L., Toth, I., Jorda, L., Weaver, H. A., & A'Hearn, M. 1998, The nucleus and inner coma of Comet 46P/Wirtanen, Astron. Astrophys., 335, L25

Lisse, C. M., et al. 2005, Rotationally Resolved 8-35 Micron Spitzer Space Telescope Observations of the Nucleus of Comet 9P/Tempel 1, Astrophys. J., Lett., 625, L139

—. 2006, Spitzer Spectral Observations of the Deep Impact Ejecta, Science, 313, 635

Reach, W. T., Vaubaillon, J., Lisse, C. M., Holloway, M., & Rho, J. 2010, Explosion of Comet 17P/Holmes as revealed by the Spitzer Space Telescope, Icarus, 208, 276

Robitaille, T., Deil, C., & Ginsburg, A. 2020, reproject: Python-based astronomical image reprojection, Astrophysics Source Code Library 2011.023

Schambeau, C. A., Fernández, Y. R., Lisse, C. M., Samarasinha, N., & Woodney, L. M. 2015, A new analysis of Spitzer observations of Comet 29P/Schwassmann-Wachmann 1, Icarus, 260, 60

Sitko, M. L., et al. 2011, Infrared Spectroscopy of Comet 73P/Schwassmann-Wachmann 3 Using the Spitzer Space Telescope, Astron. J., 142, 80

Smith, J. D. T., et al. 2007, Spectral Mapping Reconstruction of Extended Sources, Publ. Astron. Soc. Pac., 119, 1133

Spitzer Science Center. 2012, IRS Instrument Handbook (Pasadena: Spitzer Science Center)

Stansberry, J. A., et al. 2004, Spitzer Observations of the Dust Coma and Nucleus of 29P/Schwassmann-Wachmann 1, Astrophys. J., Suppl. Ser., 154, 463

Teplitz, H., & Brinkworth, C. 2011, SPICE User's Guide (Pasadena: Spitzer Science Center)

Werner, M. W., et al. 2004, The Spitzer Space Telescope Mission, Astrophys. J., Suppl. Ser., 154, 1

Wooden, D., Desch, S., Harker, D., Gail, H., & Keller, L. 2007, Comet Grains and Implications for Heating and Radial Mixing in the Protoplanetary Disk, in Protostars and Planets V, ed. B. Reipurth, D. Jewitt, & K. Keil (Tucson, AZ: Univ. Arizona Press), 815–833

Wooden, D. H. 2002, Comet Grains: Their IR Emission and Their Relation to ISM Grains, Earth, Moon, Planets, 89, 247

Wooden, D. H., Ishii, H. A., & Zolensky, M. E. 2017, Cometary dust: the diversity of primitive refractory grains, Philosophical Transactions of the Royal Society of London Series A, 375, 20160260

Woodward, C. E., Kelley, M. S., Bockelée-Morvan, D., & Gehrz, R. D. 2007, Water in Comet C/2003 K4 (LINEAR) with Spitzer, Astrophys. J., 671, 1065

Woodward, C. E., et al. 2011, Dust in Comet C/2007 N3 (Lulin), Astron. J., 141, 181

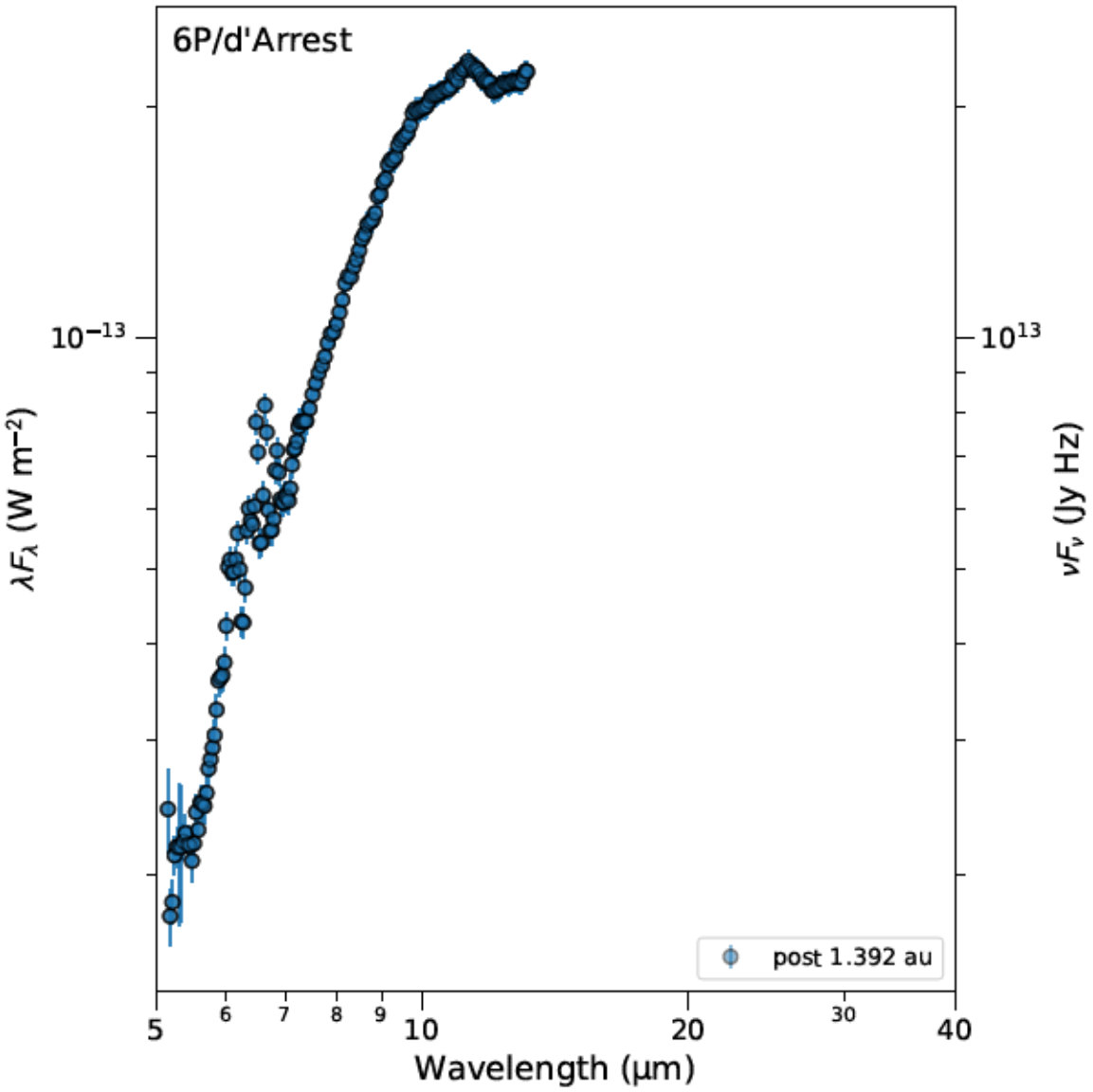

Figure 10: Comet 6P/d'Arrest.

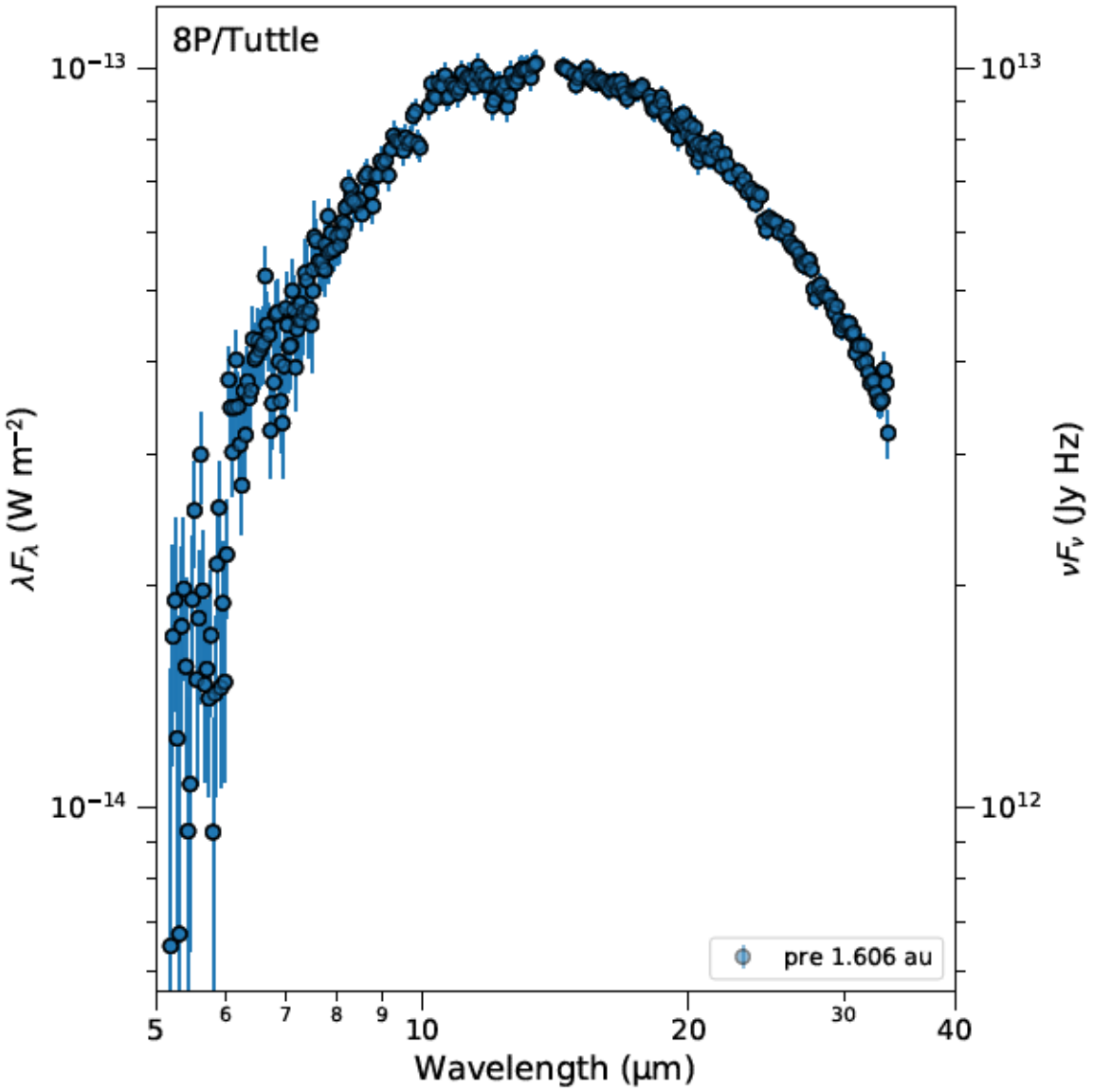

Figure 11: Comet 8P/Tuttle.

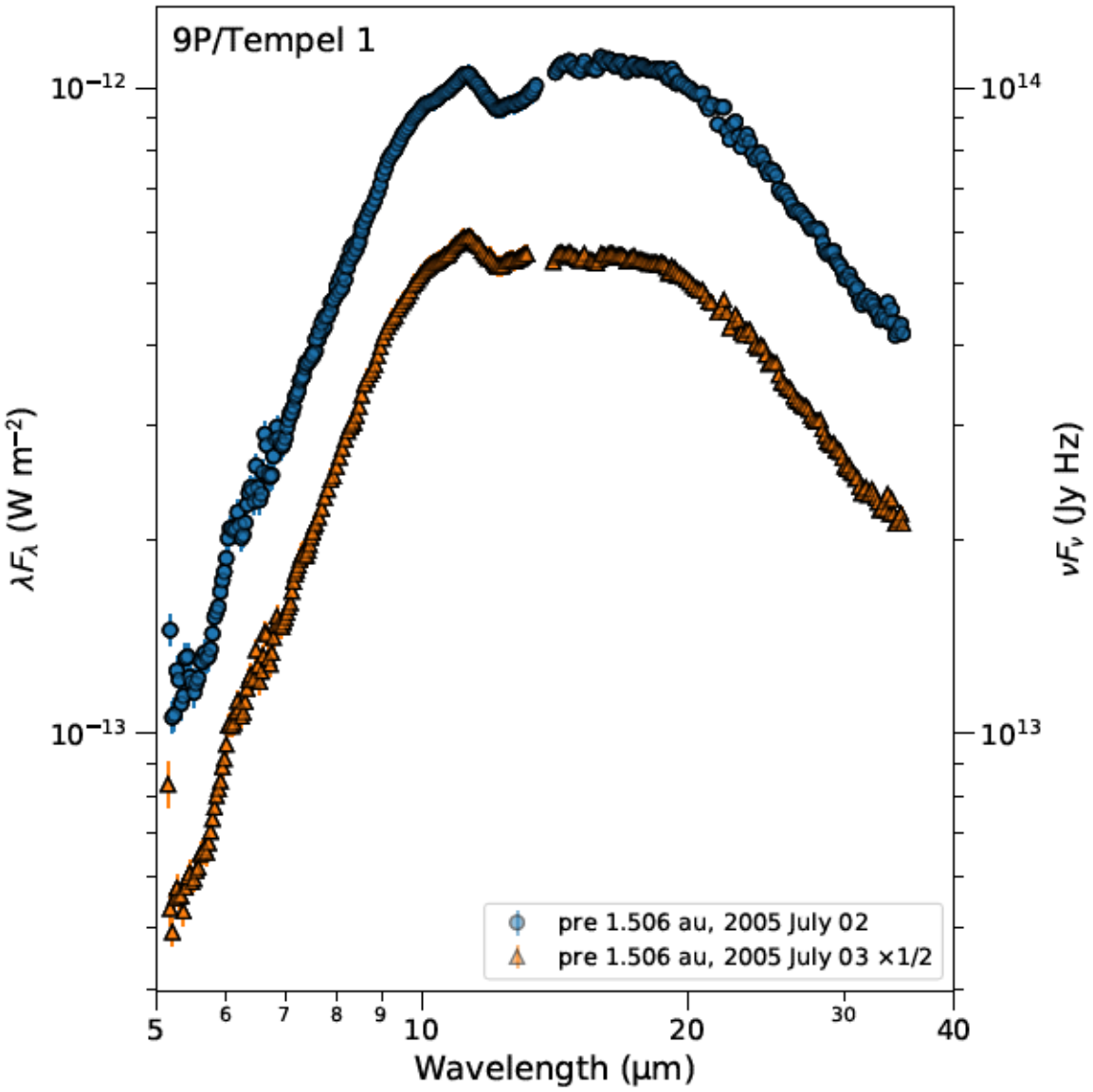

Figure 12: Comet 9P/Tempel 1.

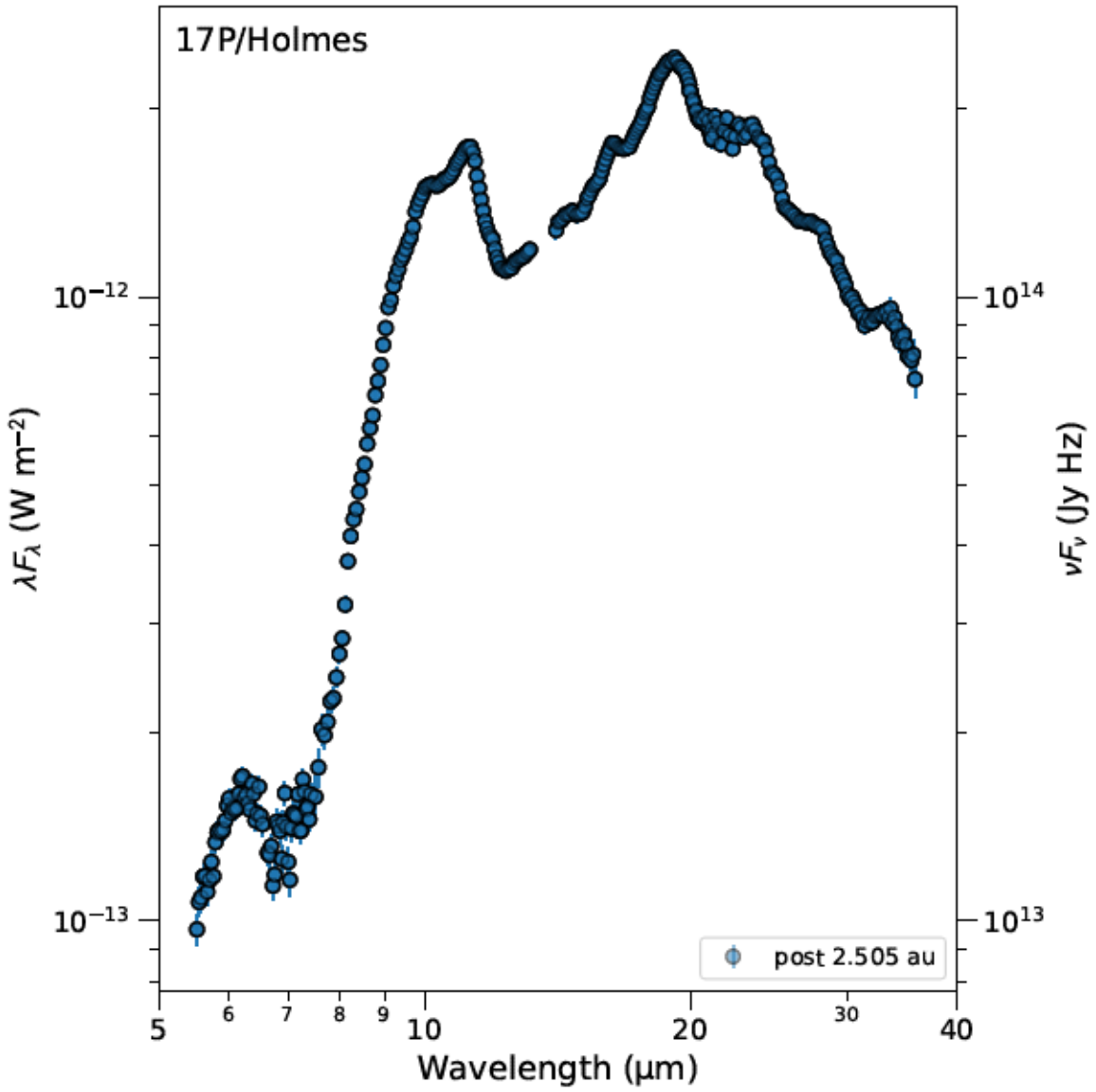

Figure 13: Comet 17P/Holmes. See Section 5.4 for cautionary notes on the spectral shape in the 6- to 9-μm region.

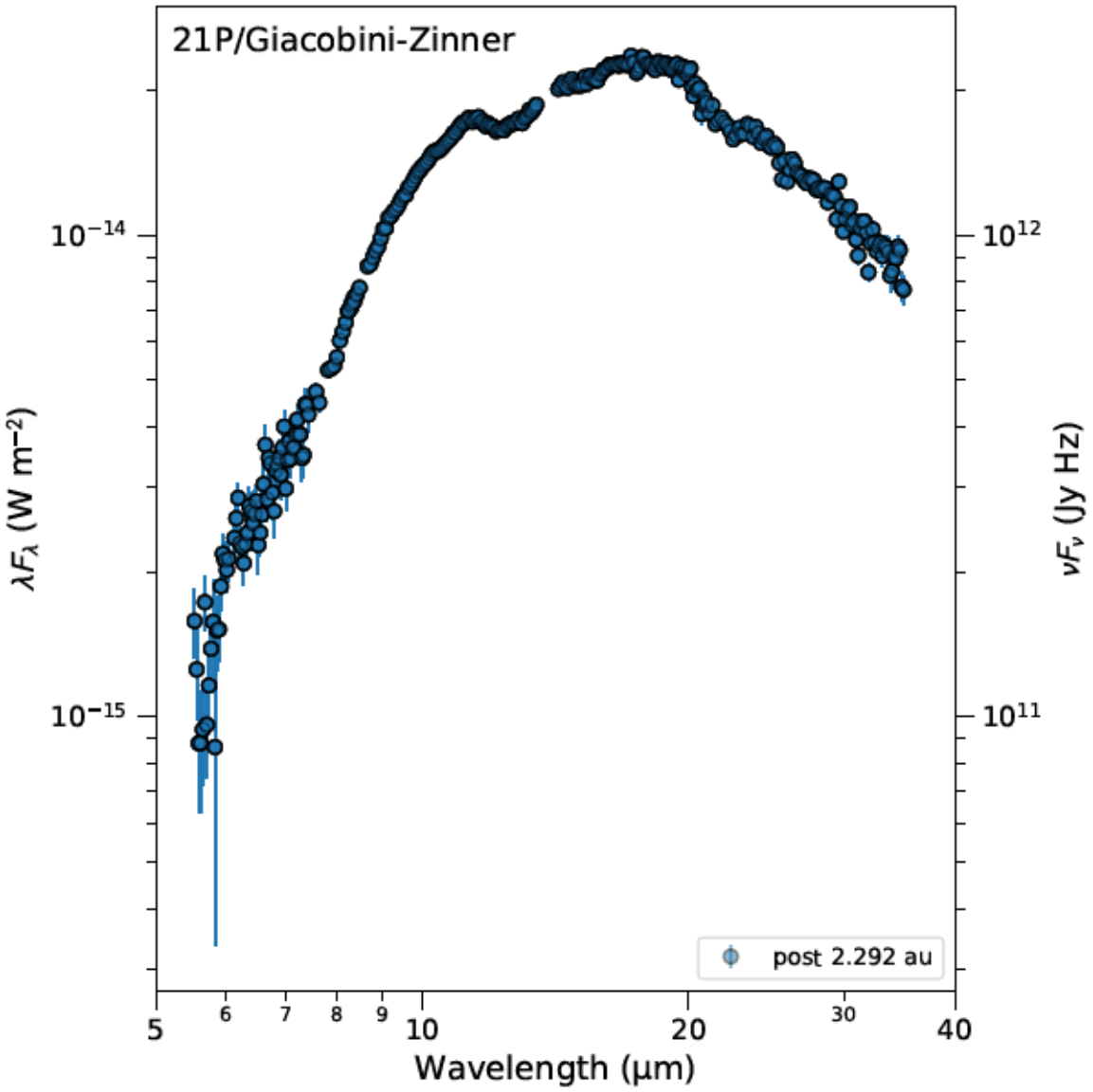

Figure 14: Comet 21P/Giacobini-Zinner. See Section 5.5 for cautionary notes on the spectral shape in the 20-μm region.

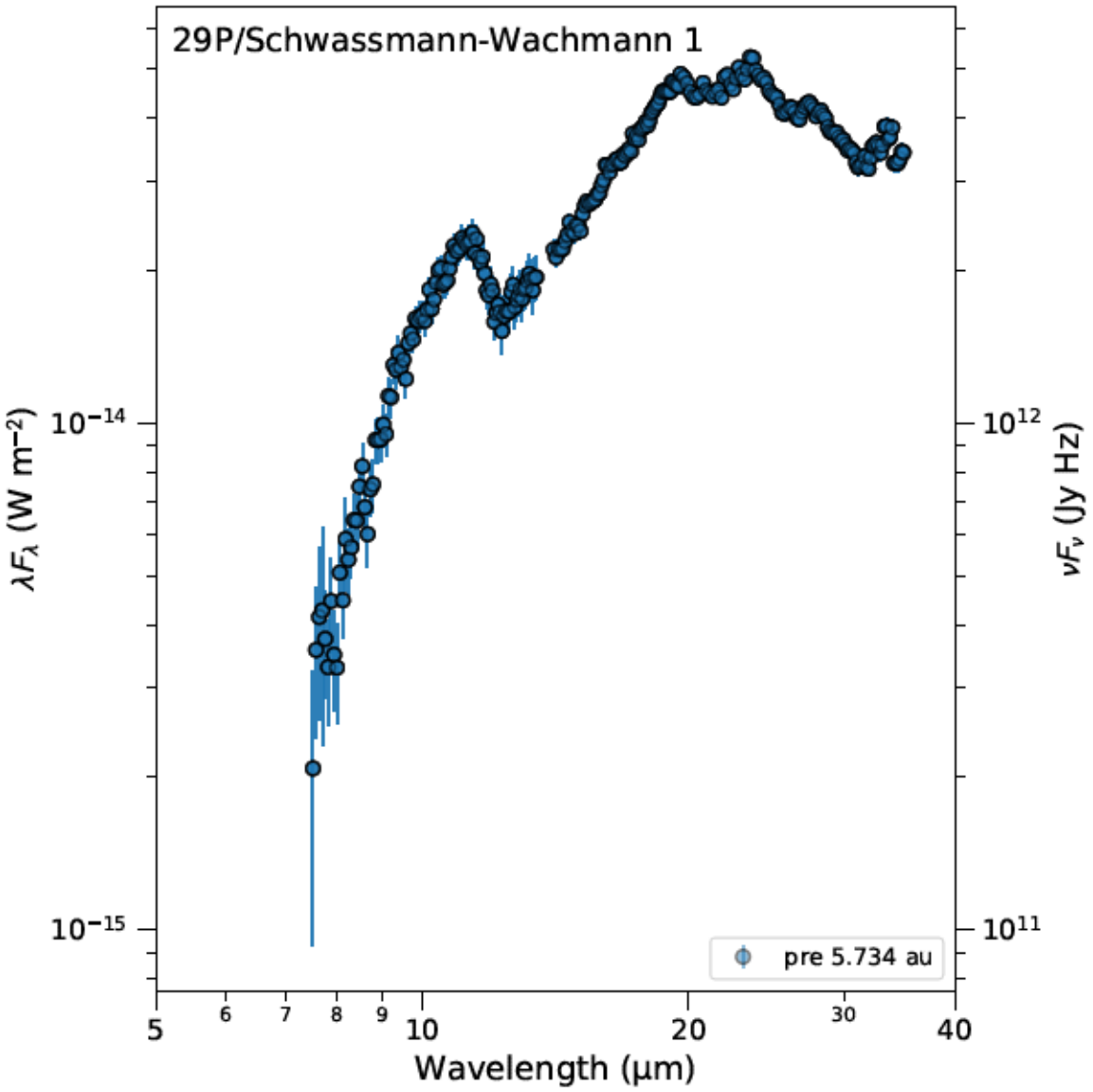

Figure 15: Comet 29P/Schwassmann-Wachmann 1.

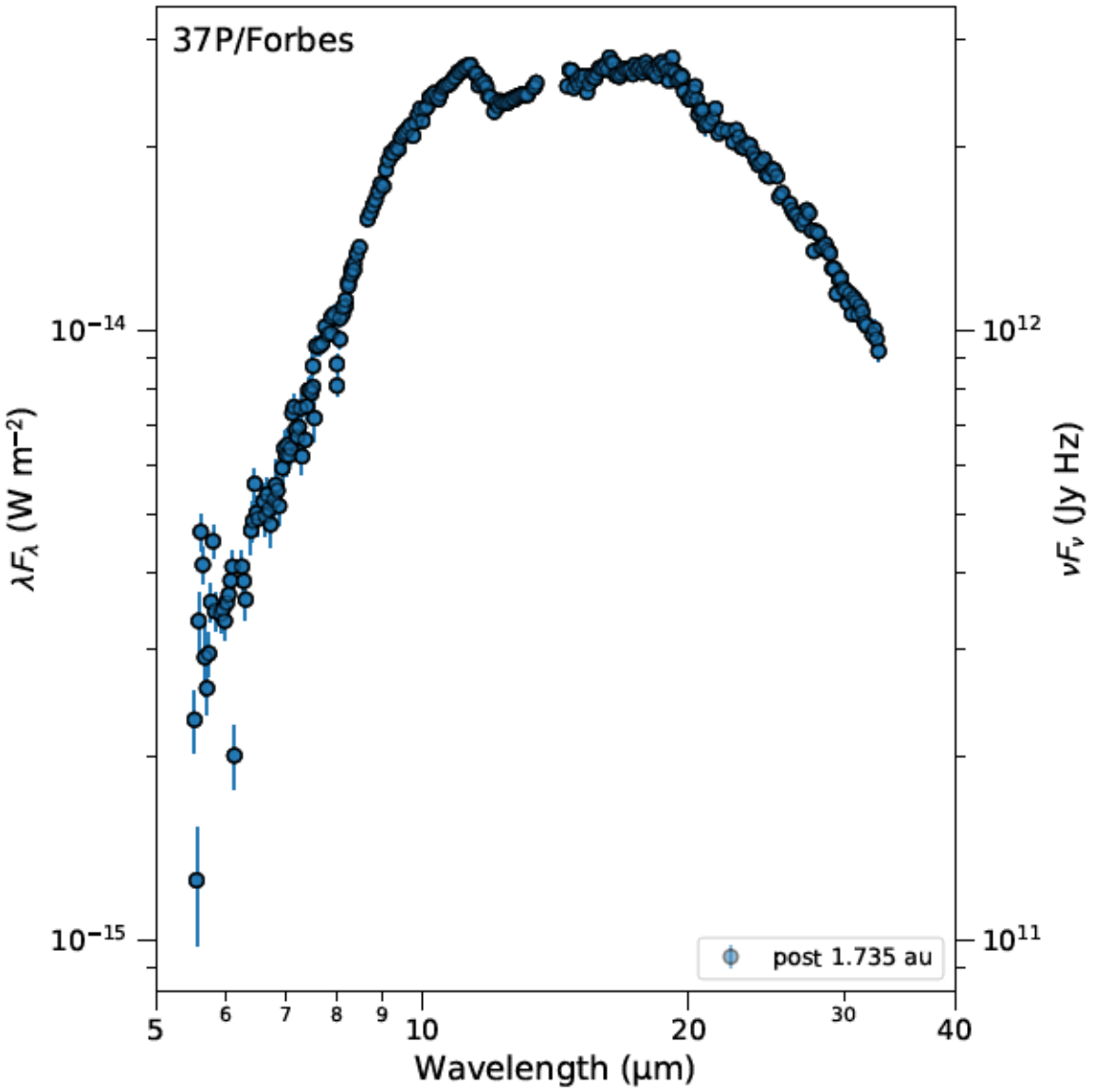

Figure 16: Comet 37P/Forbes.

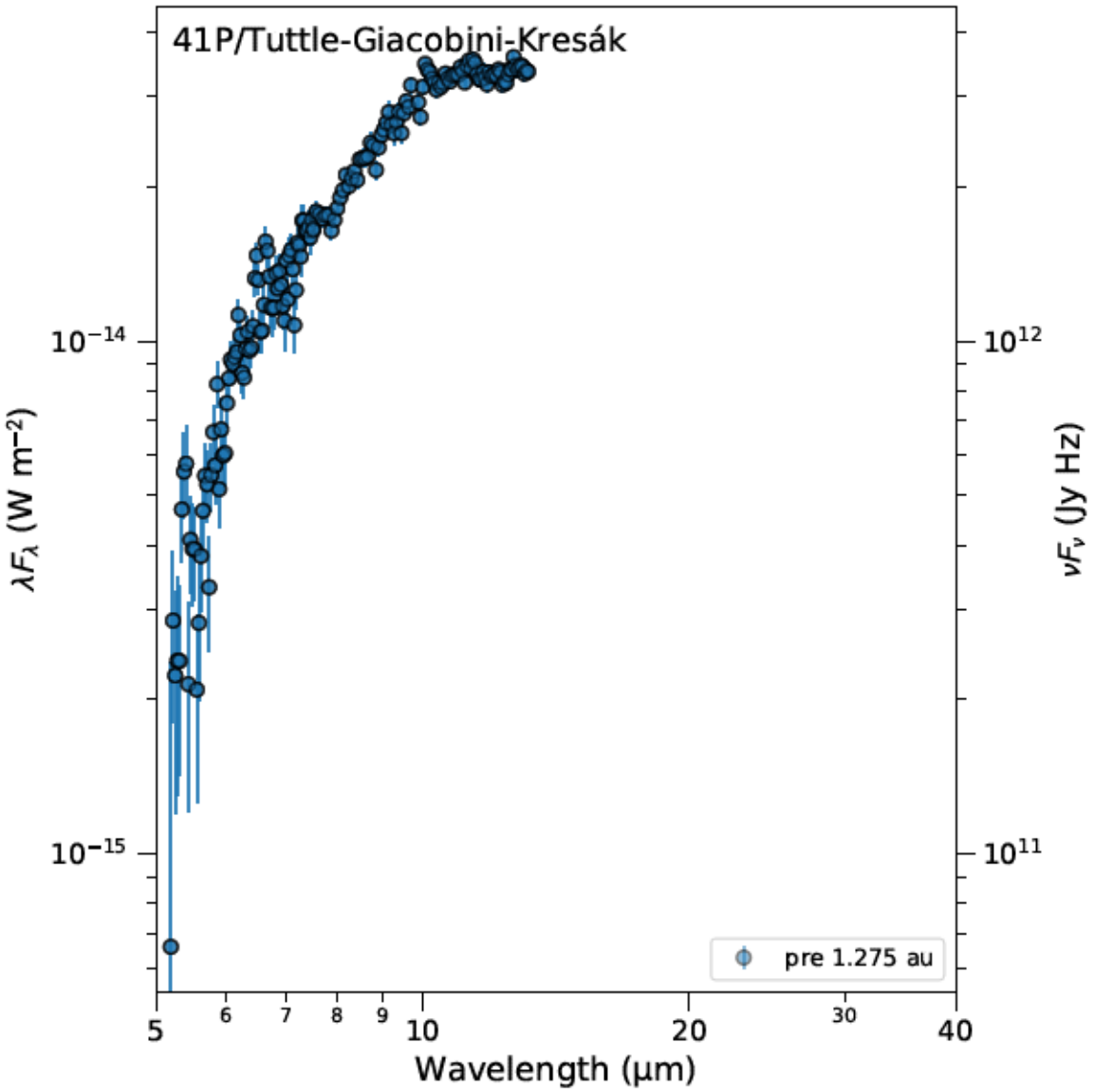

Figure 17: Comet 41P/Tuttle-Giacobini-Kresák.

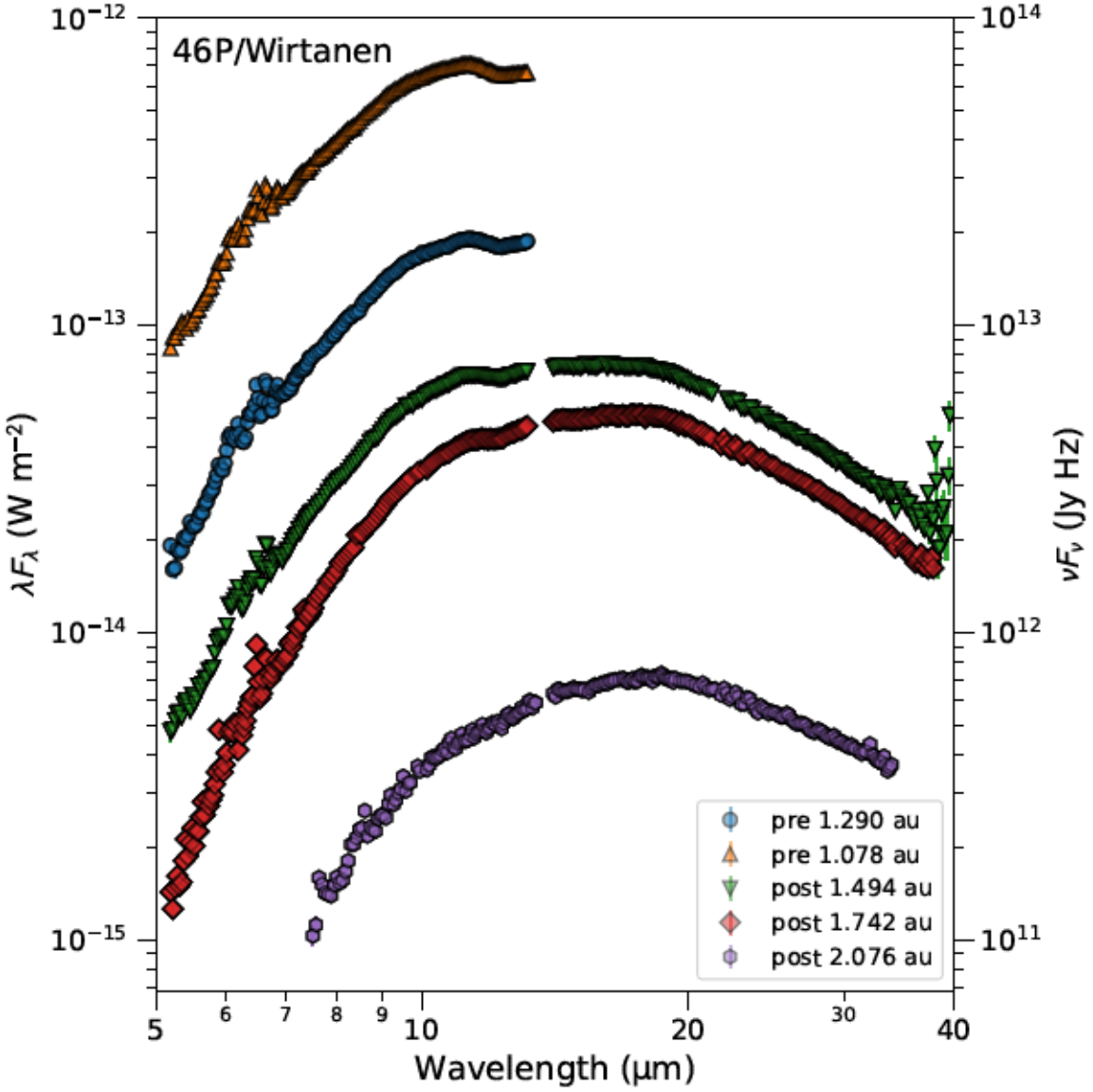

Figure 18: Comet 46P/Wirtanen.

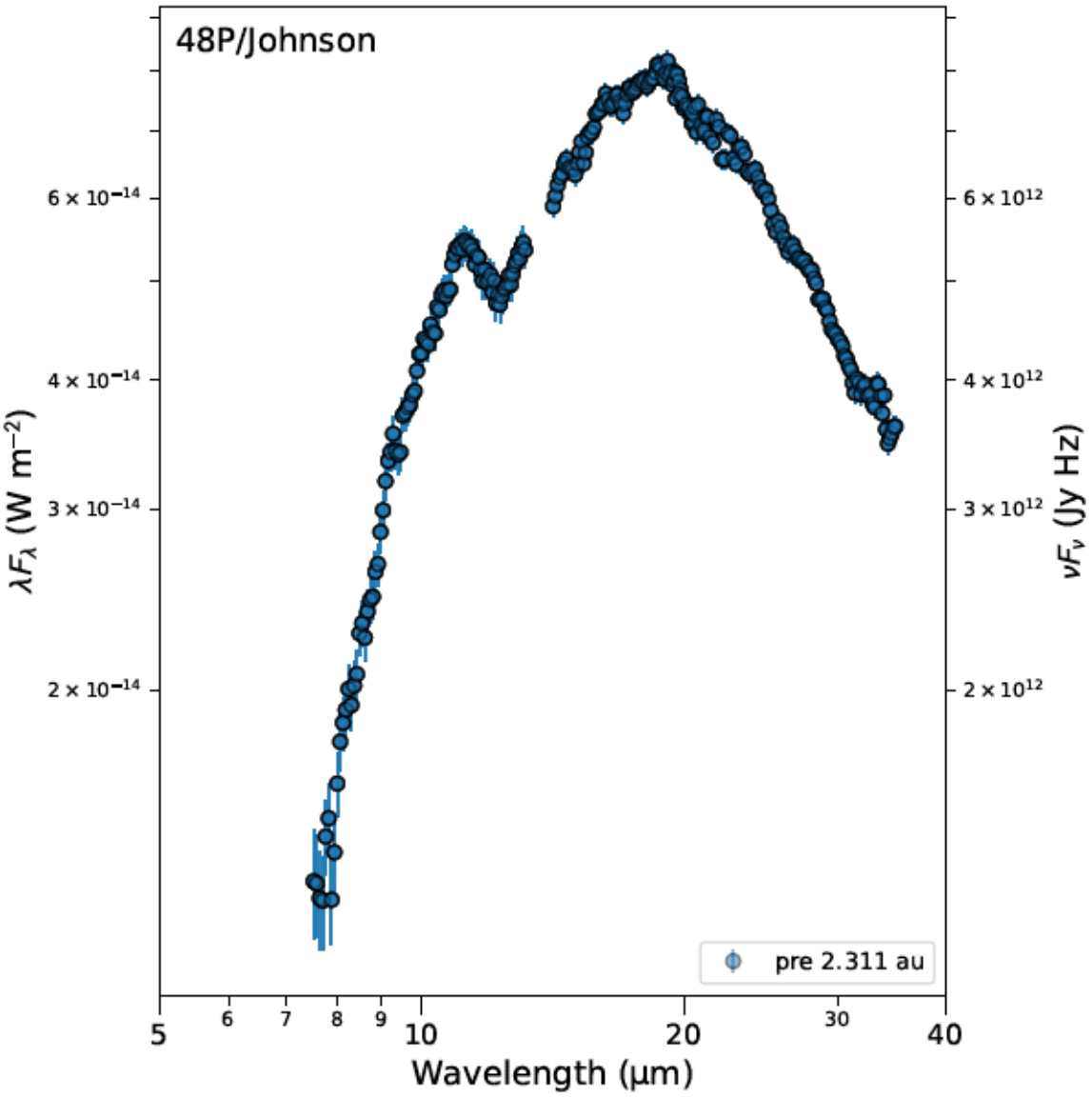

Figure 19: Comet 48P/Johnson.

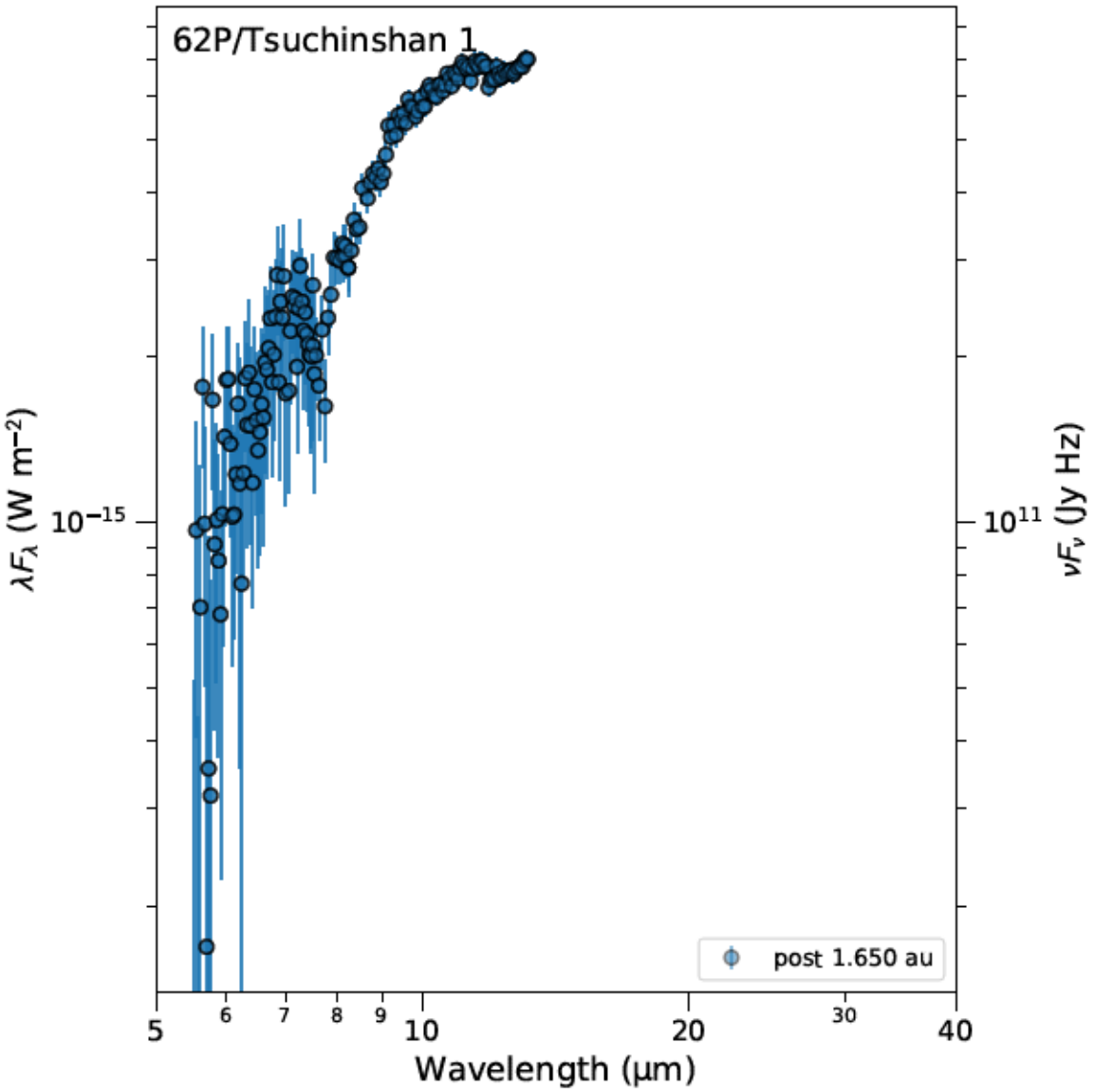

Figure 20: Comet 62P/Tsuchinshan 1.

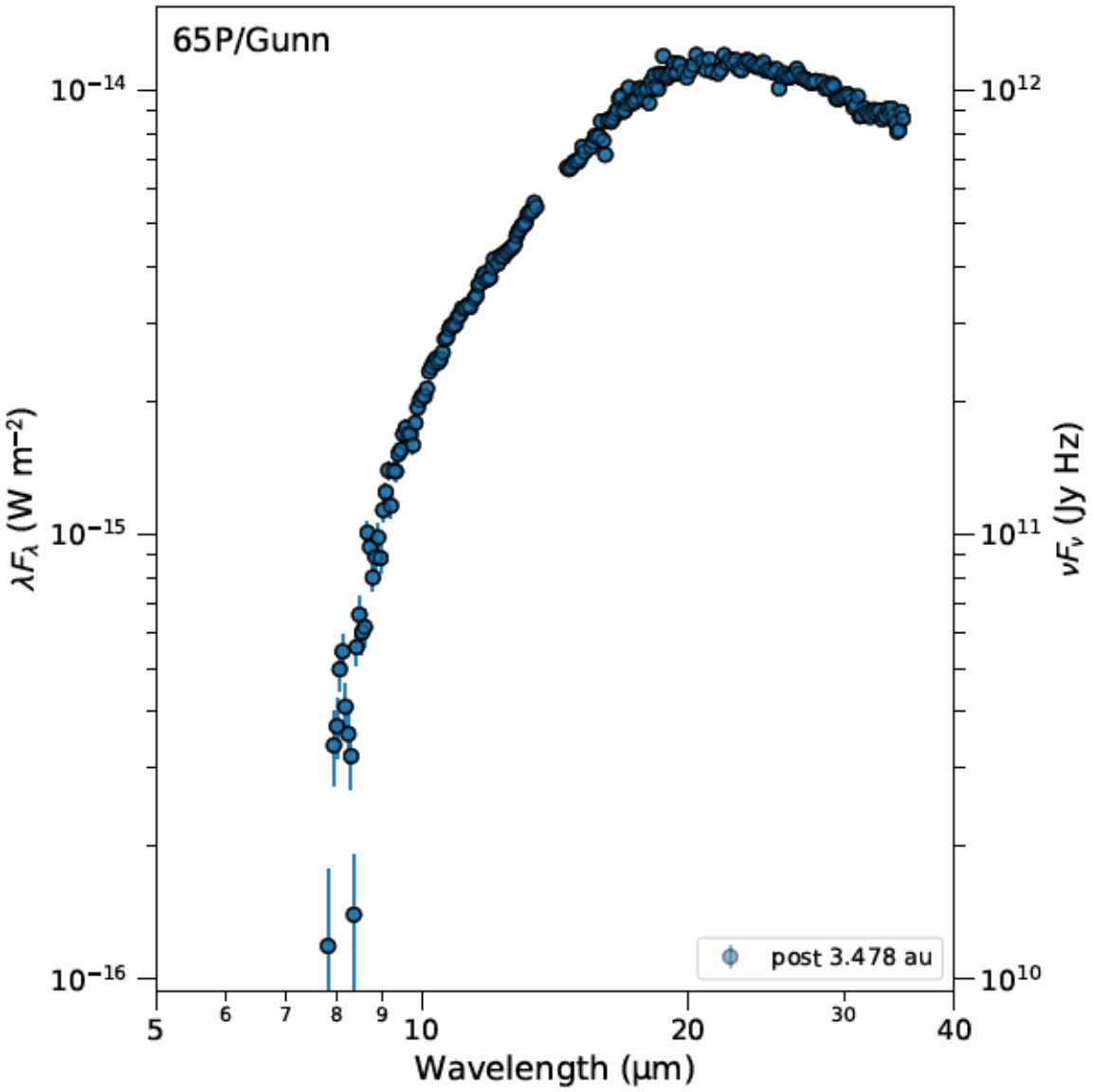

Figure 21: Comet 65P/Gunn.

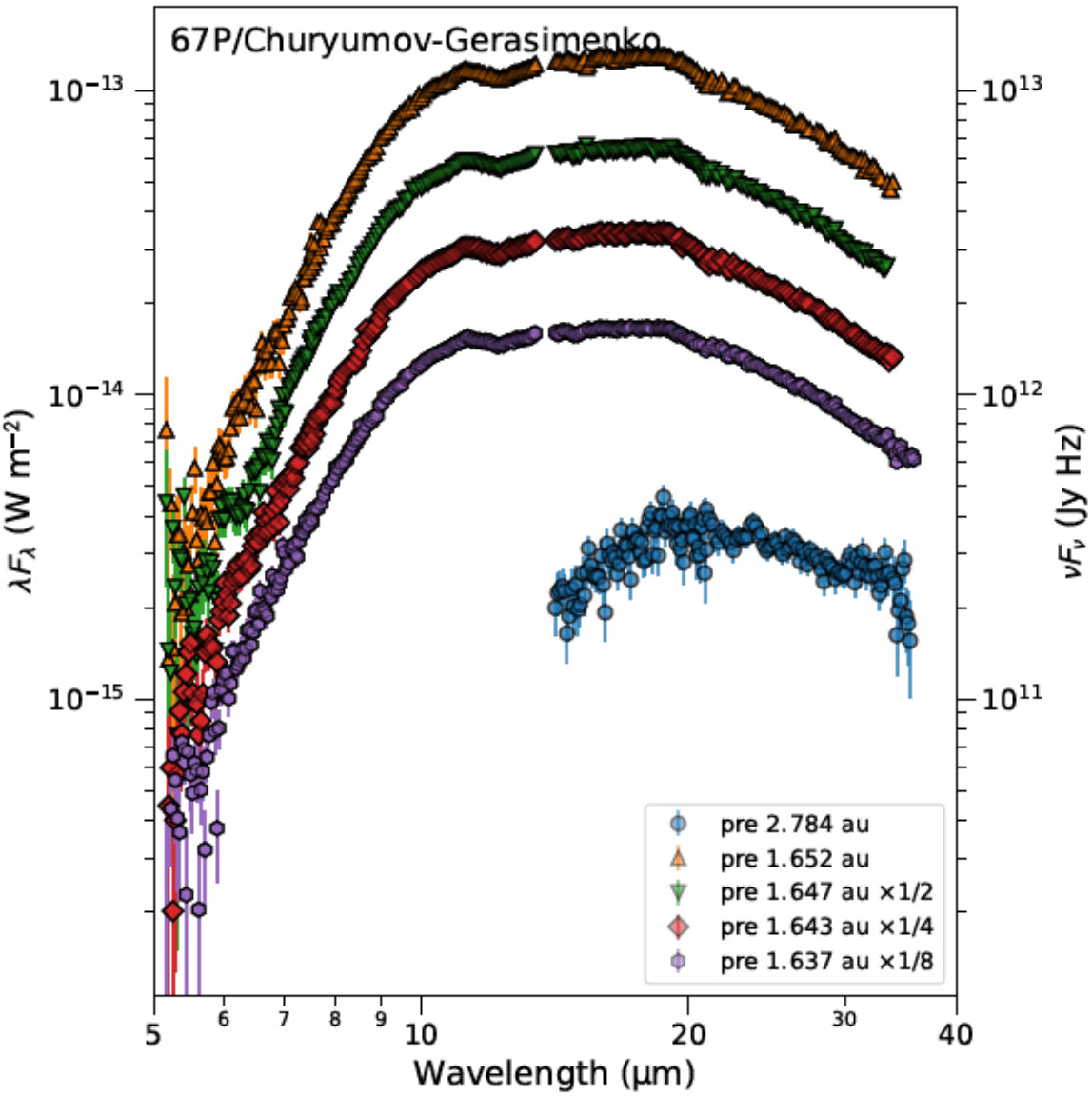

Figure 22: Comet 67P/Churyumov-Gerasimenko.

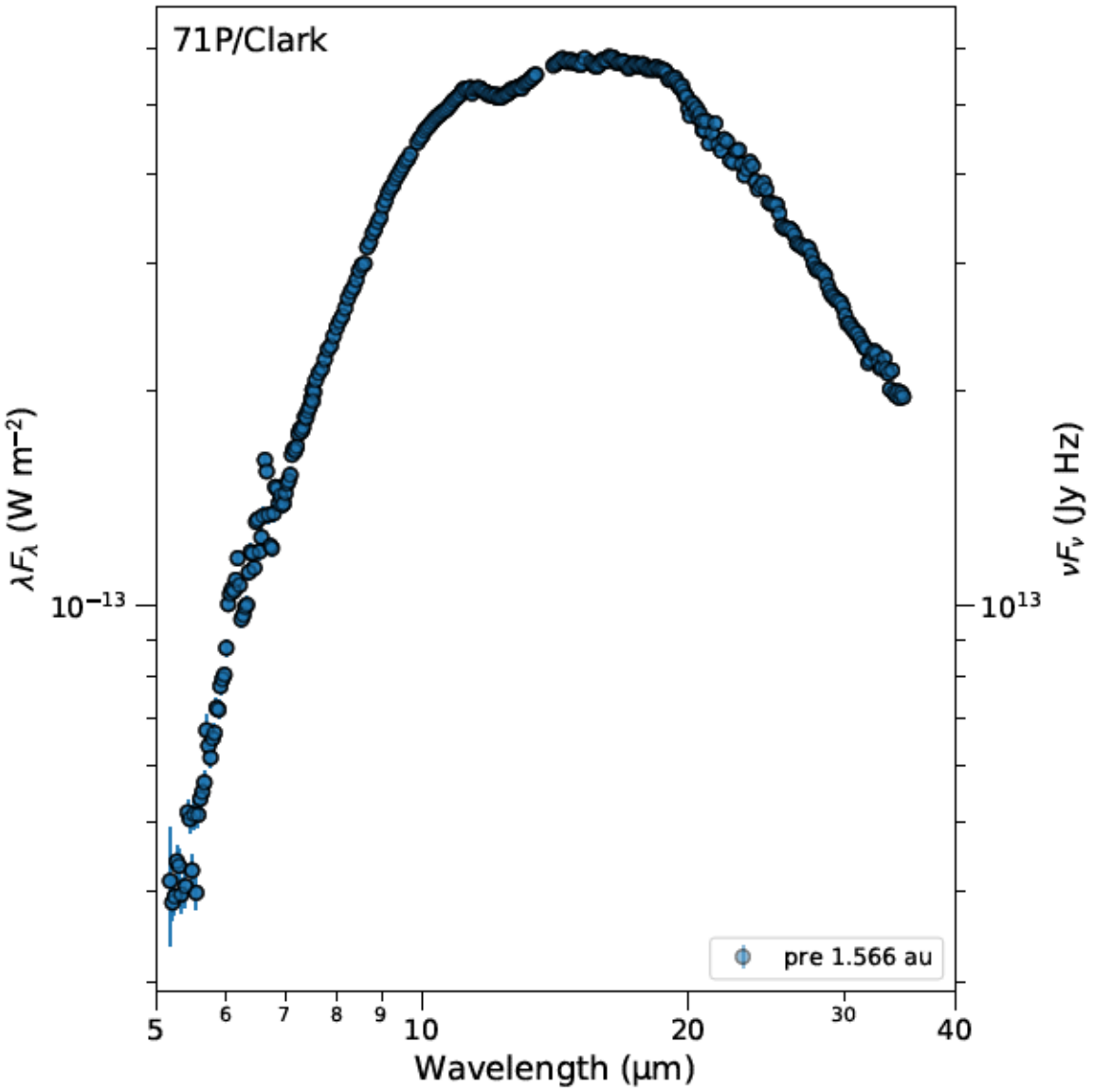

Figure 23: Comet 71P/Clark.

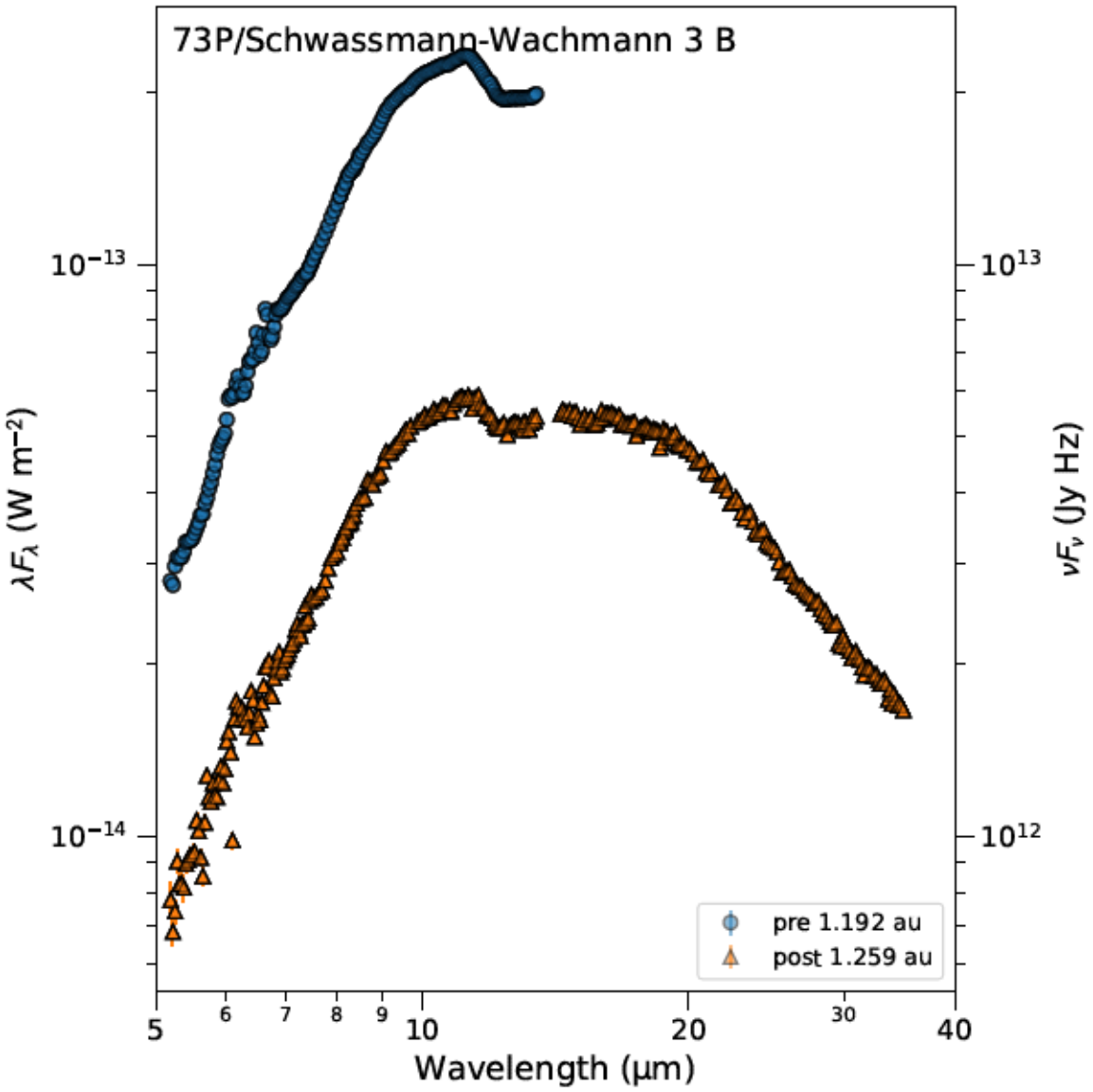

Figure 24: Comet 73P/Schwassmann-Wachmann 3 B.

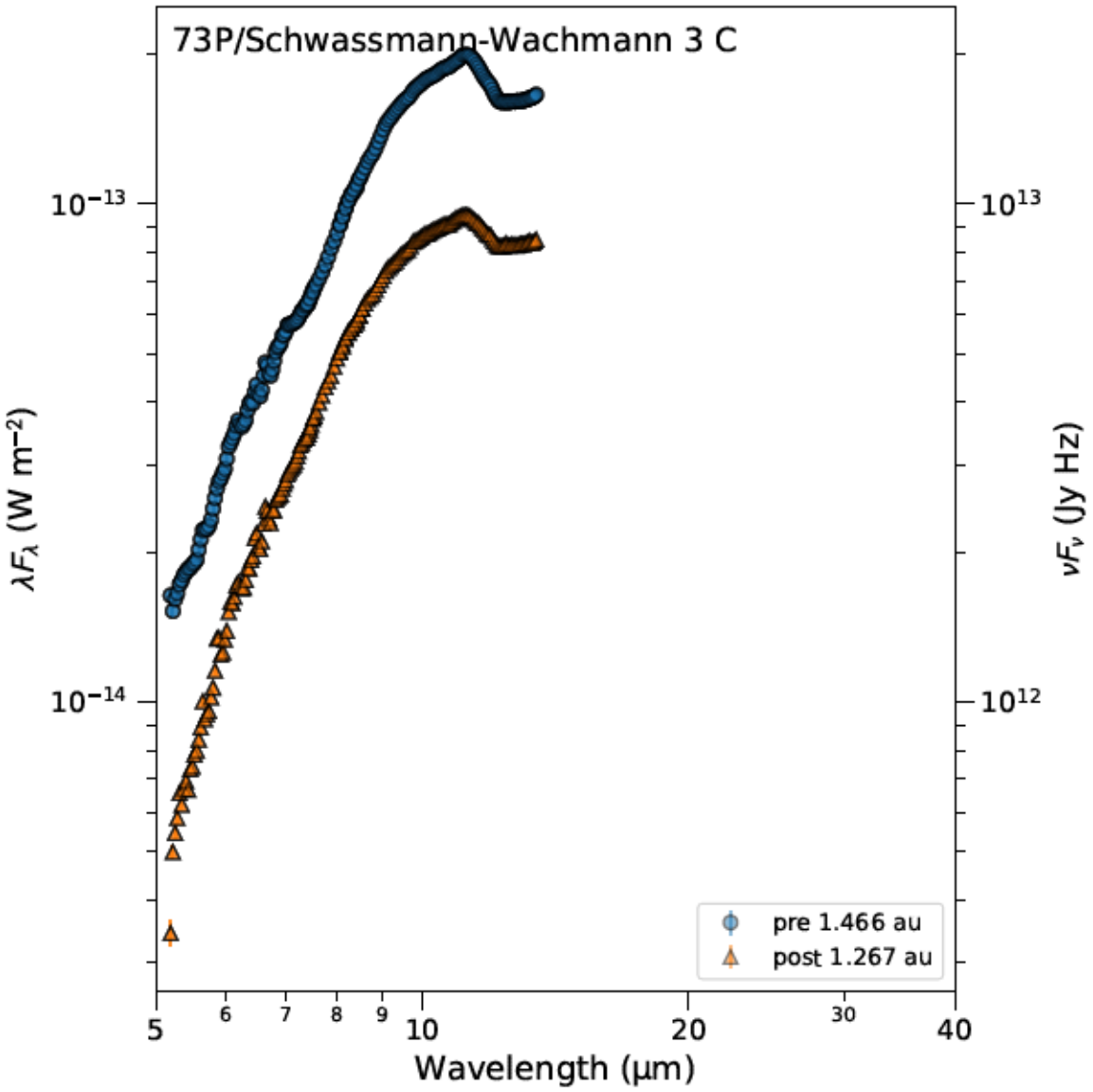

Figure 25: Comet 73P/Schwassmann-Wachmann 3 C.

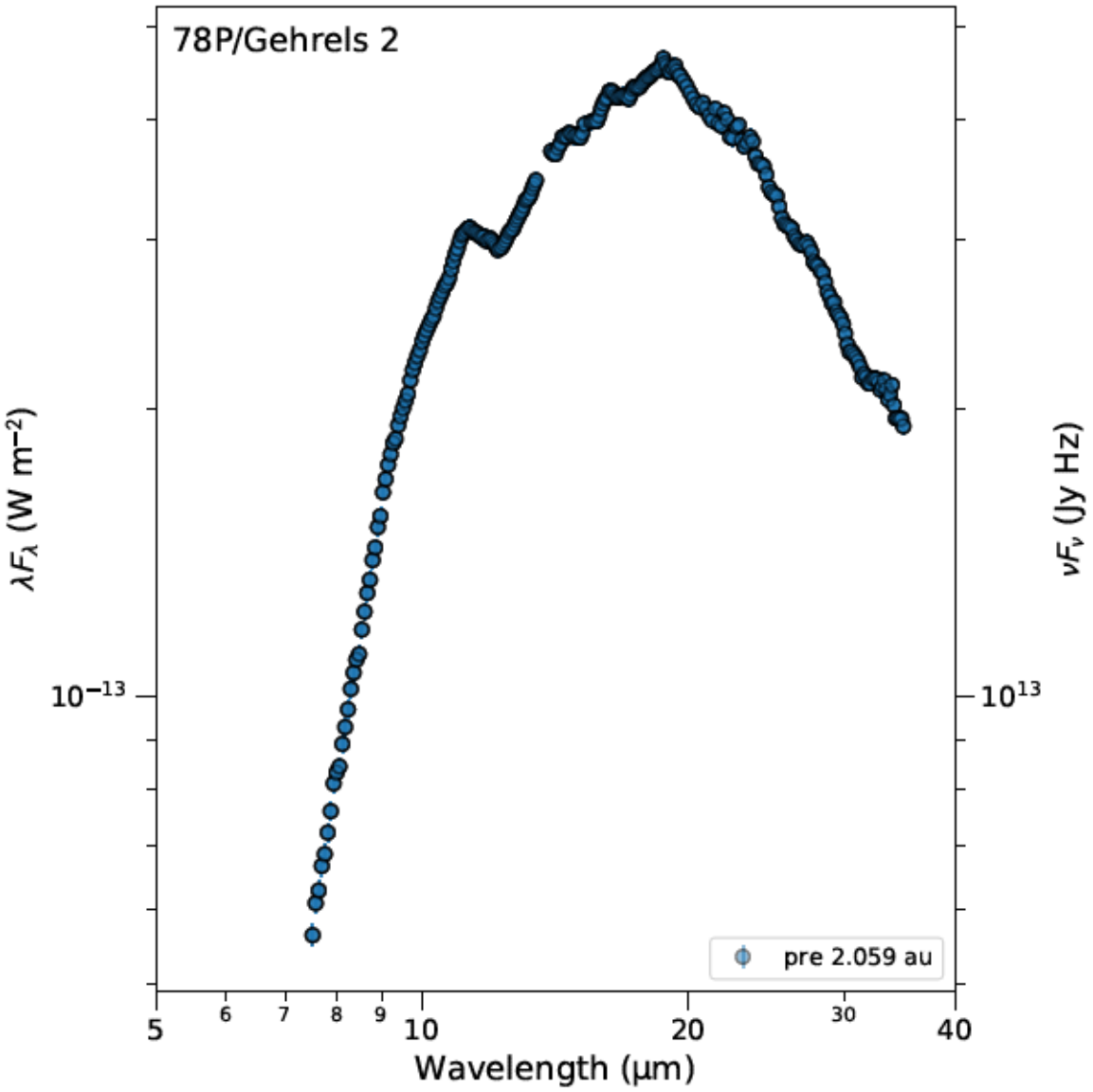

Figure 26: Comet 78P/Gerhels 2.

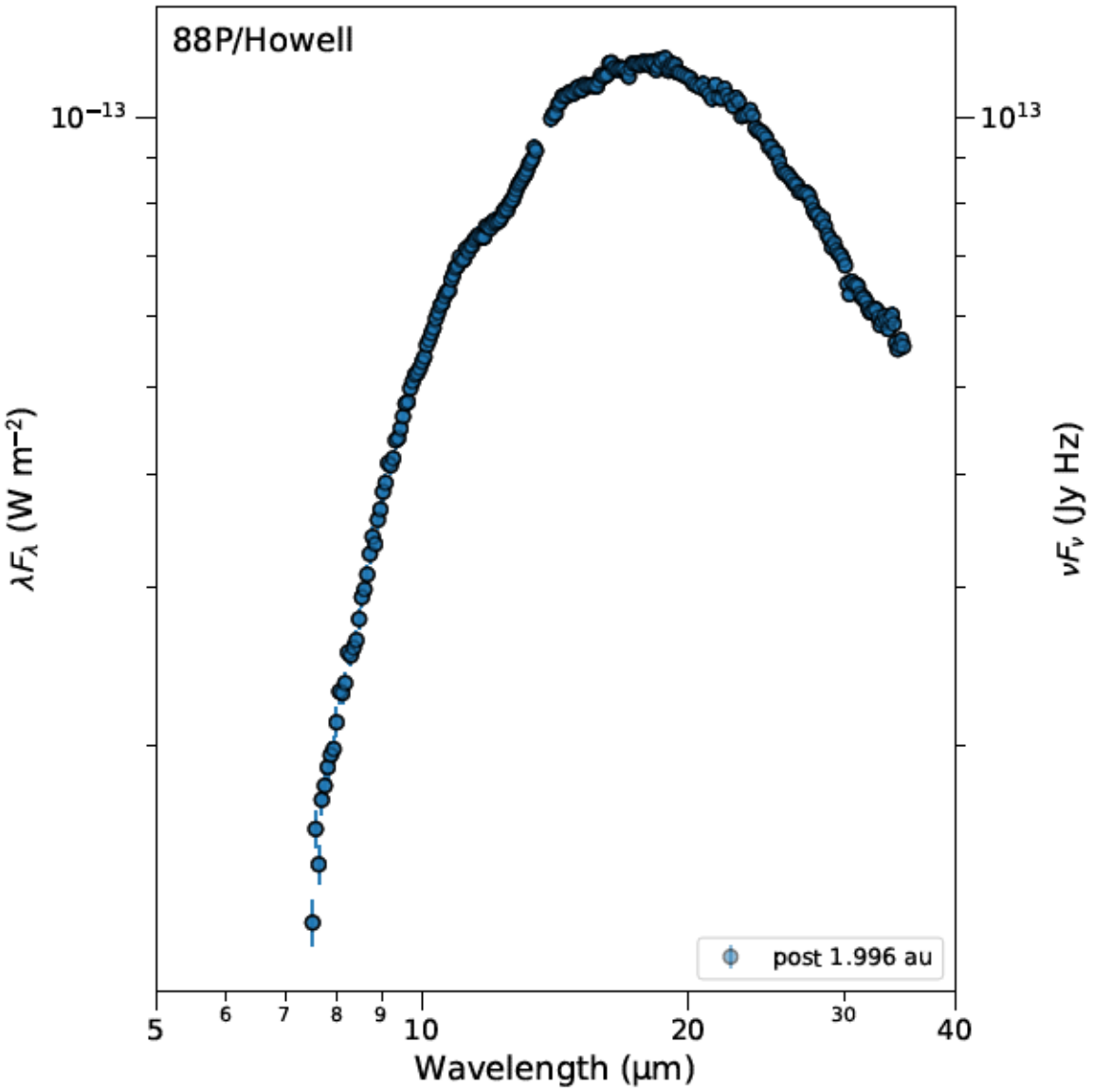

Figure 27: Comet 88P/Howell.

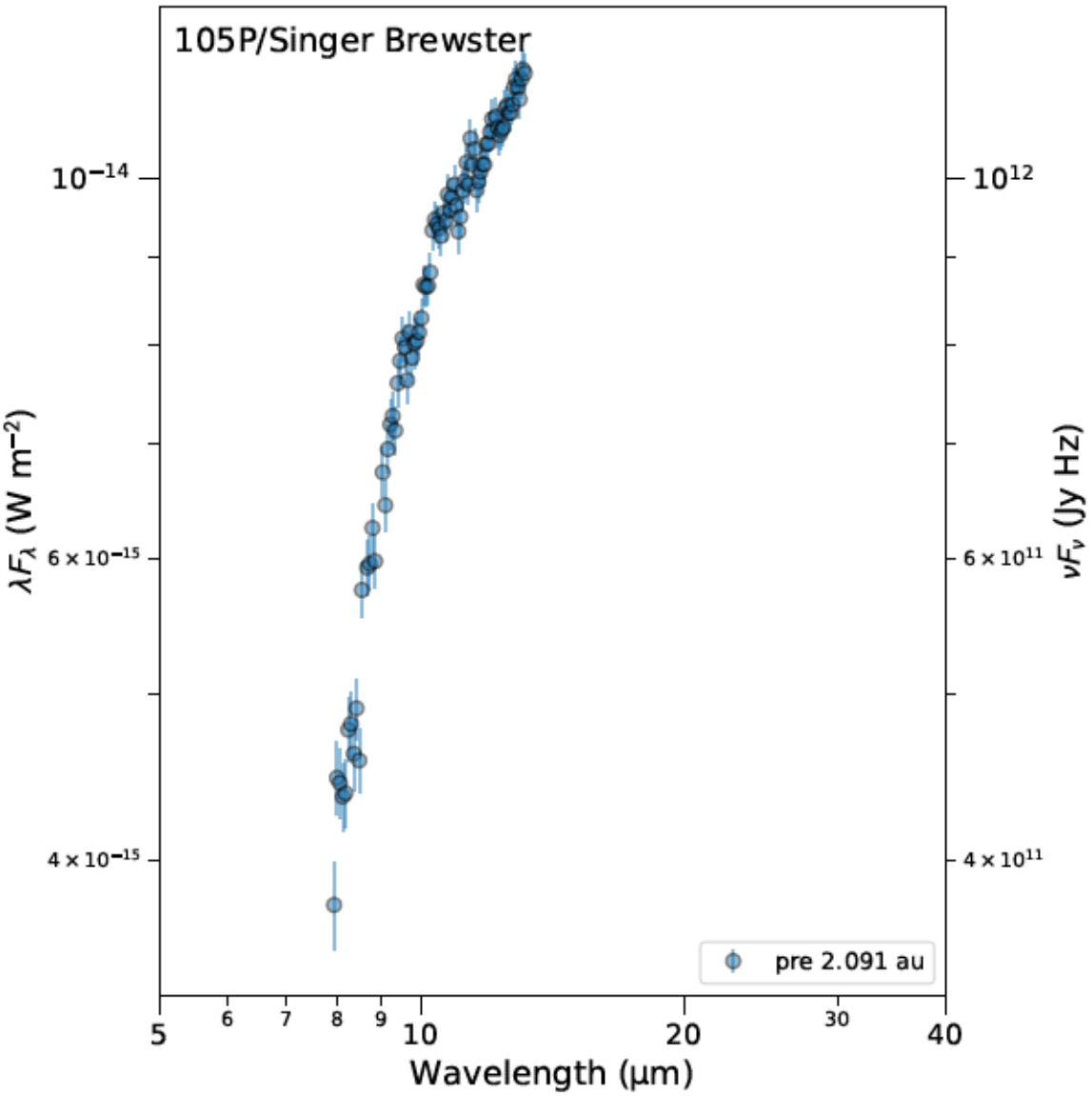

Figure 28: Comet 105P/Singer Brewser.

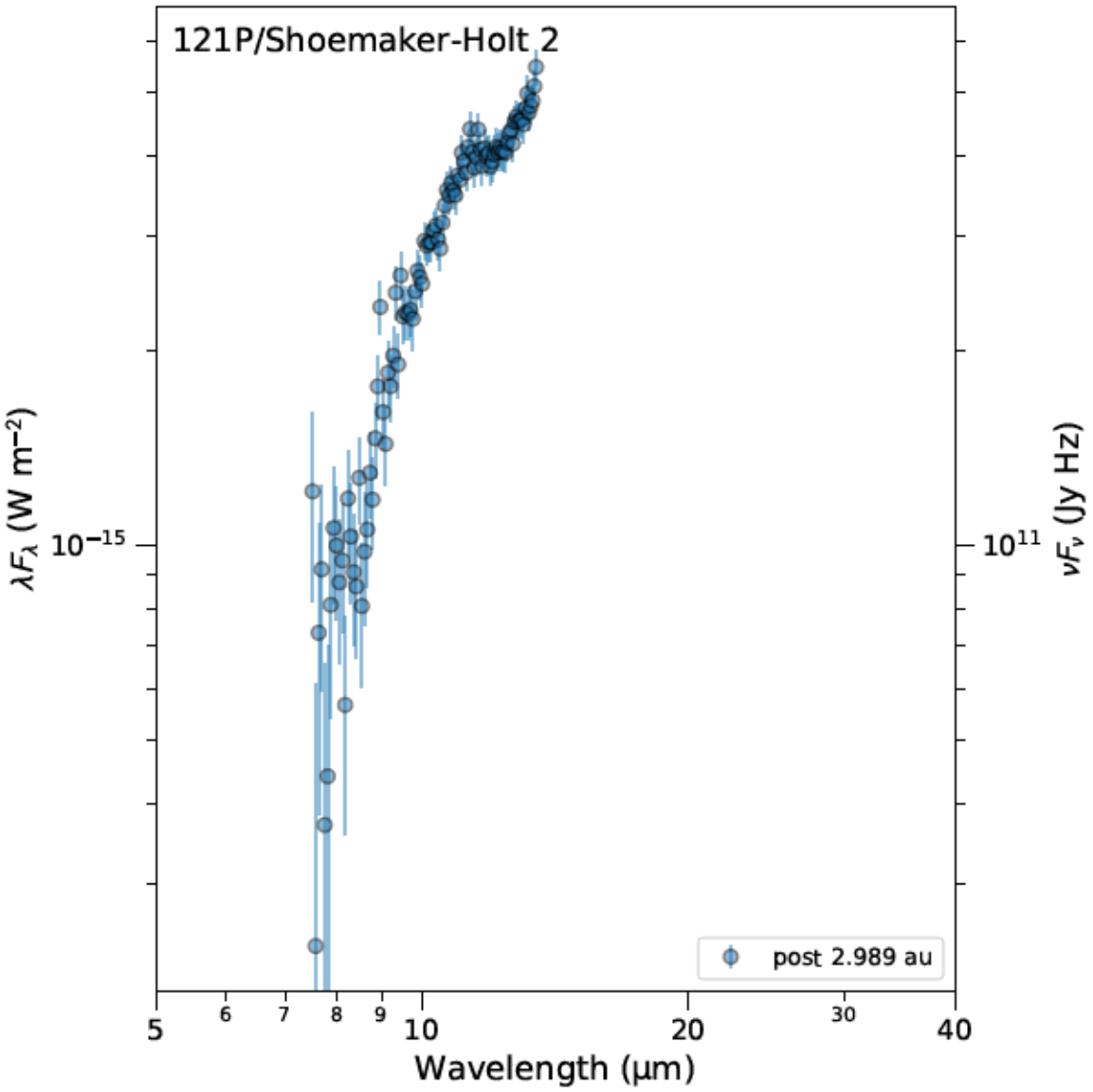

Figure 29: Comet 121P/Shoemaker-Holt 2.

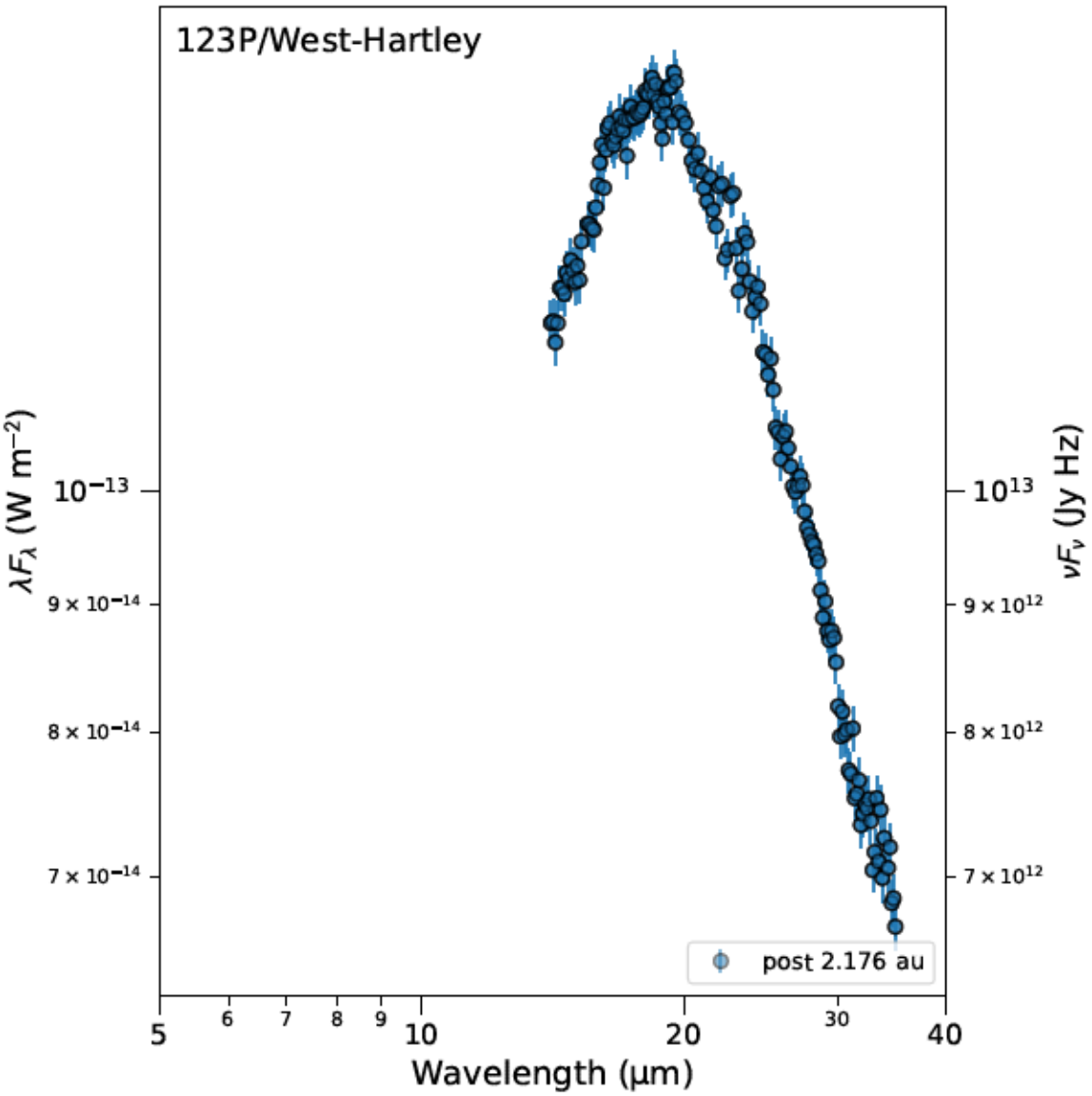

Figure 30: Comet 123P/West-Hartley.

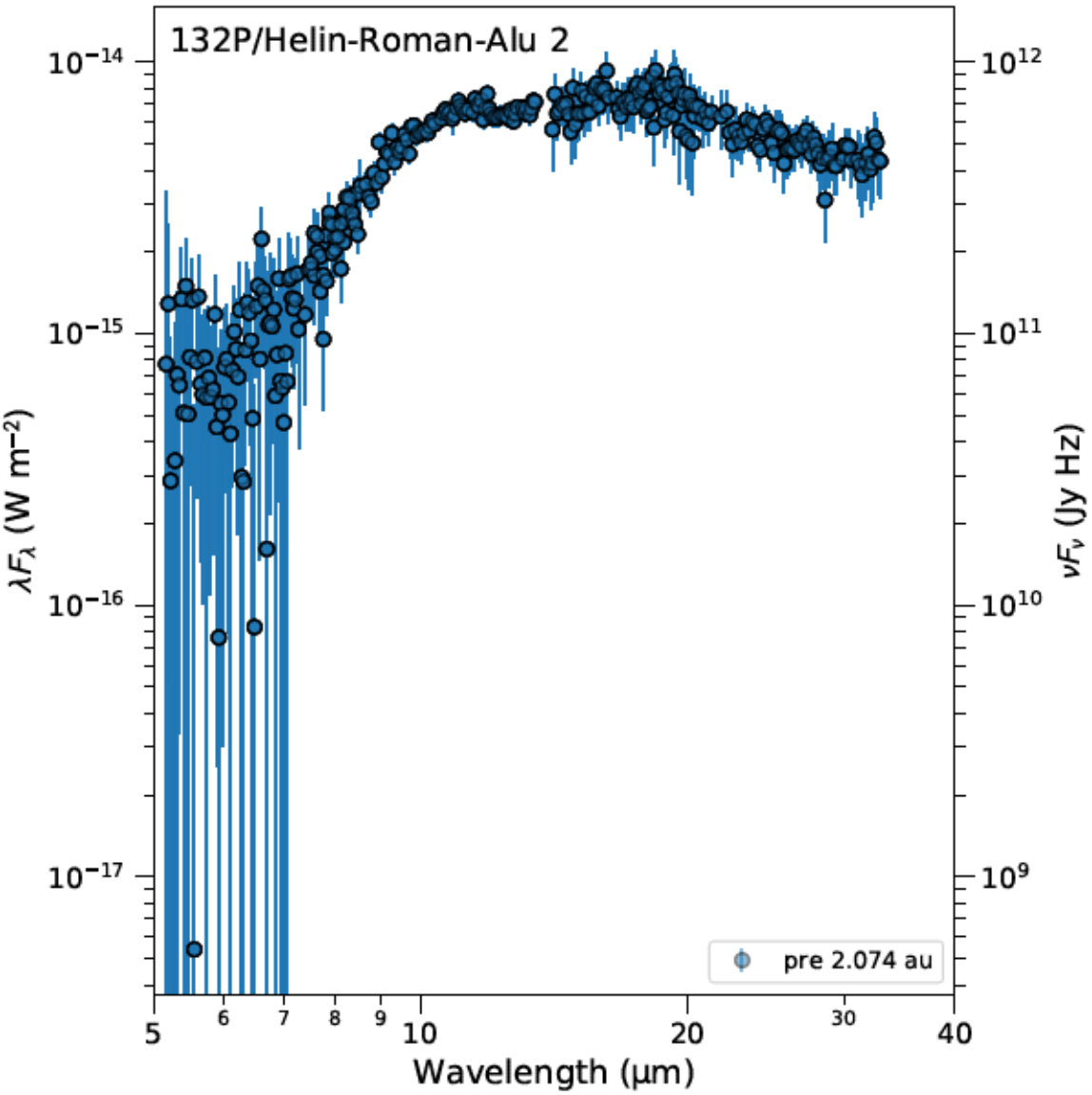

Figure 31: Comet 132P/Helin-Roman-Alu 2.

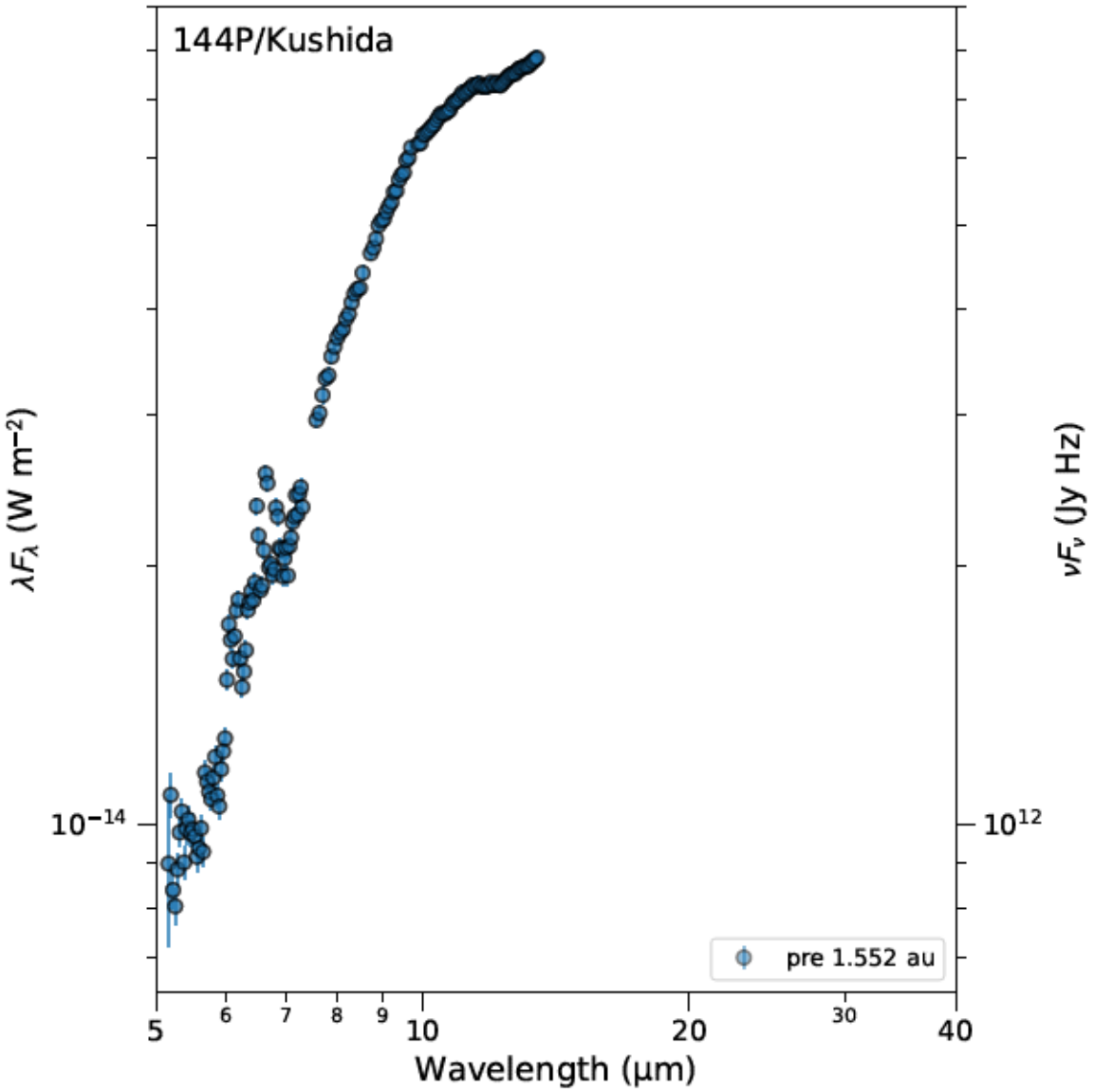

Figure 32: Comet 144P/Kushida.

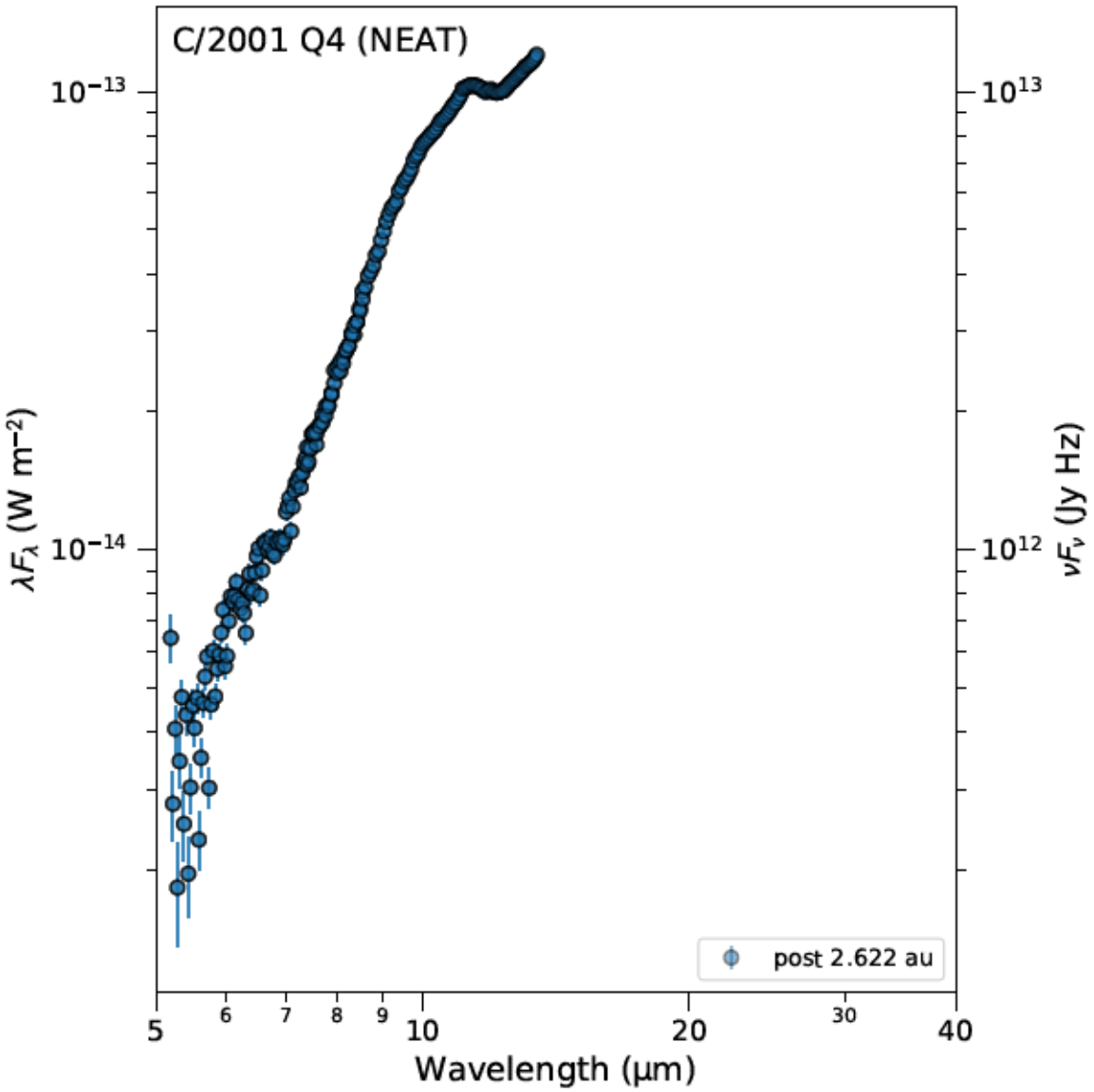

Figure 33: Comet C/2001 Q4 (NEAT).

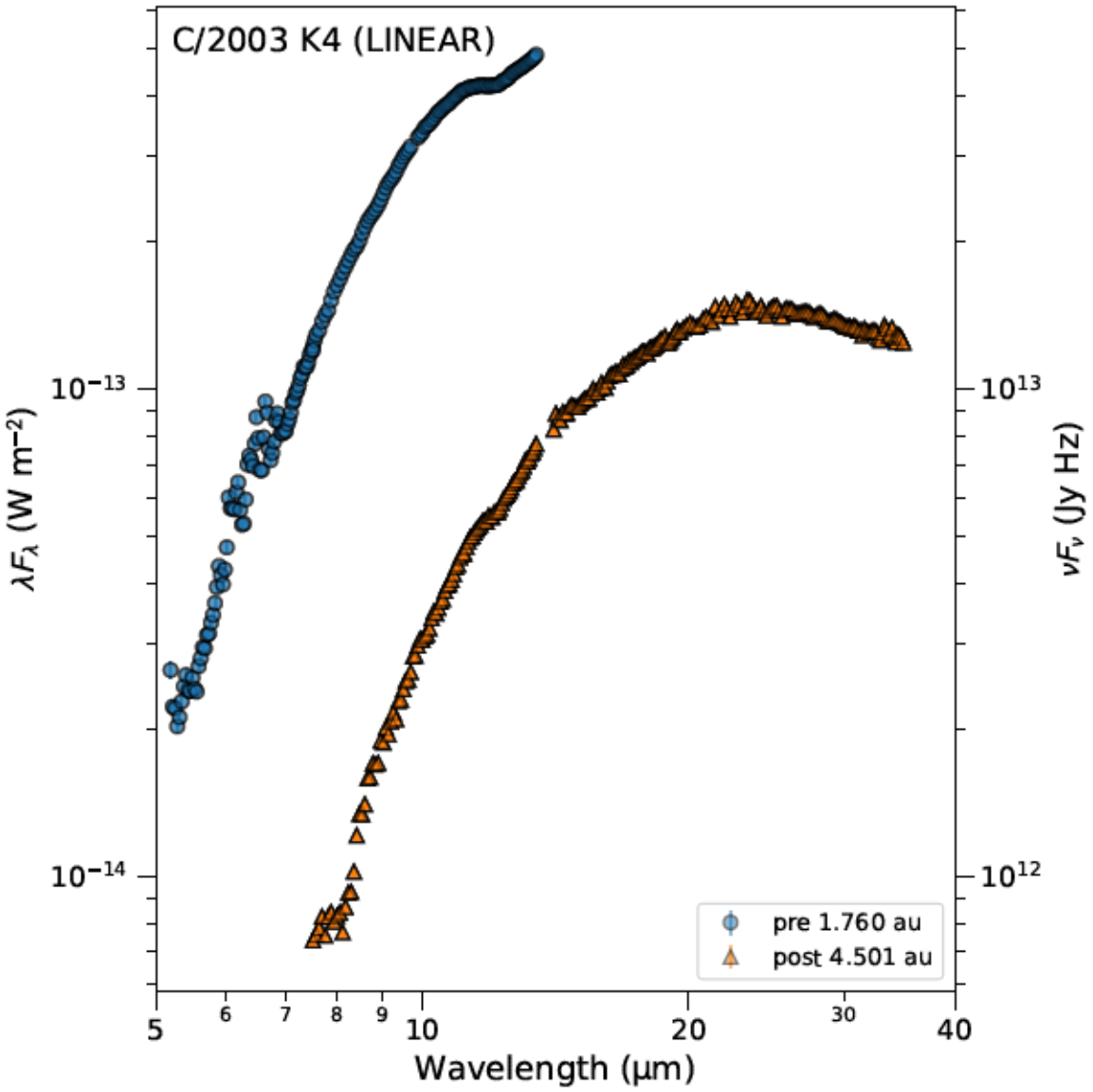

Figure 34: Comet C/2003 K4 (LINEAR).

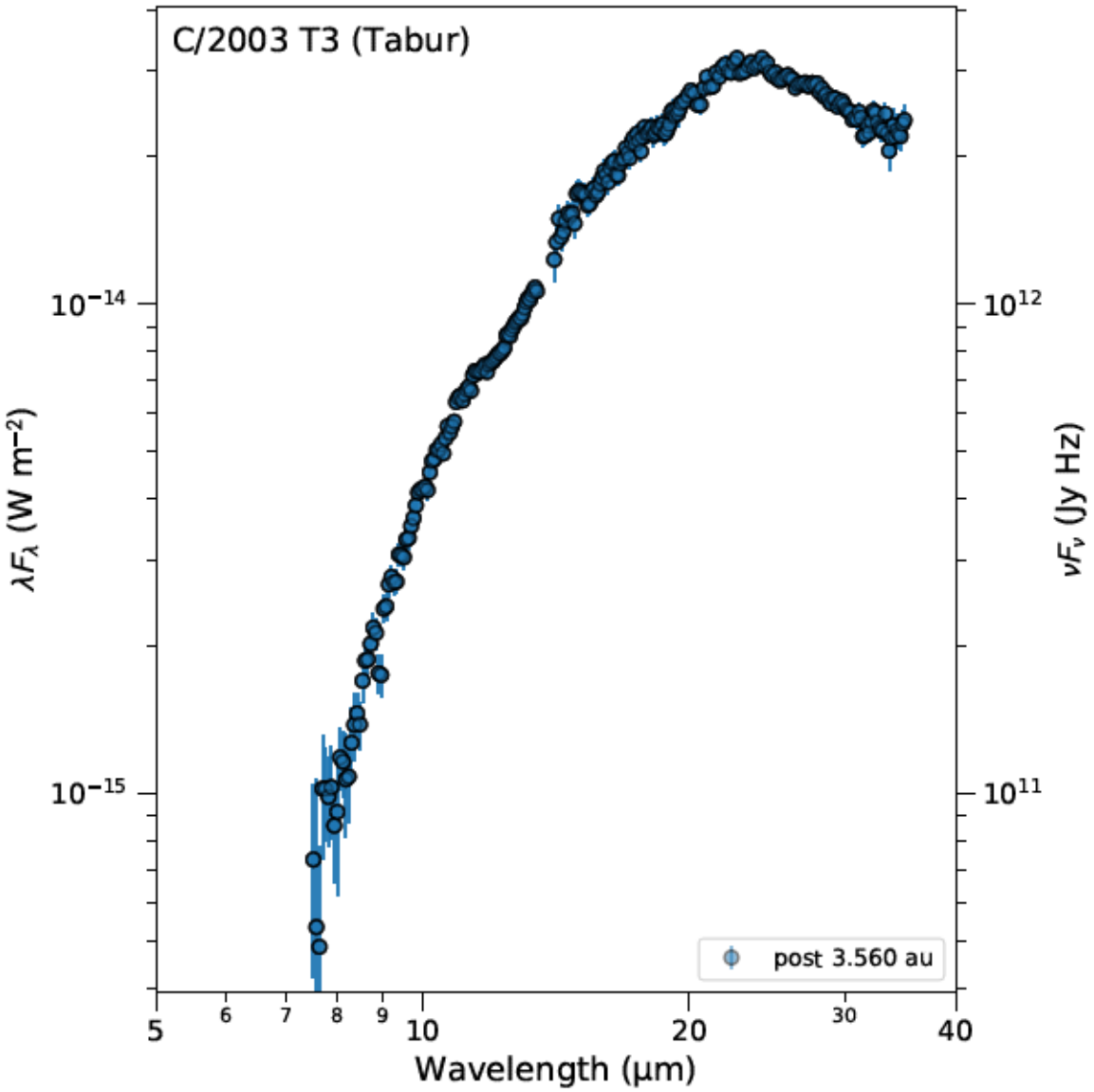

Figure 35: Comet C/2003 T3 (Tabur).

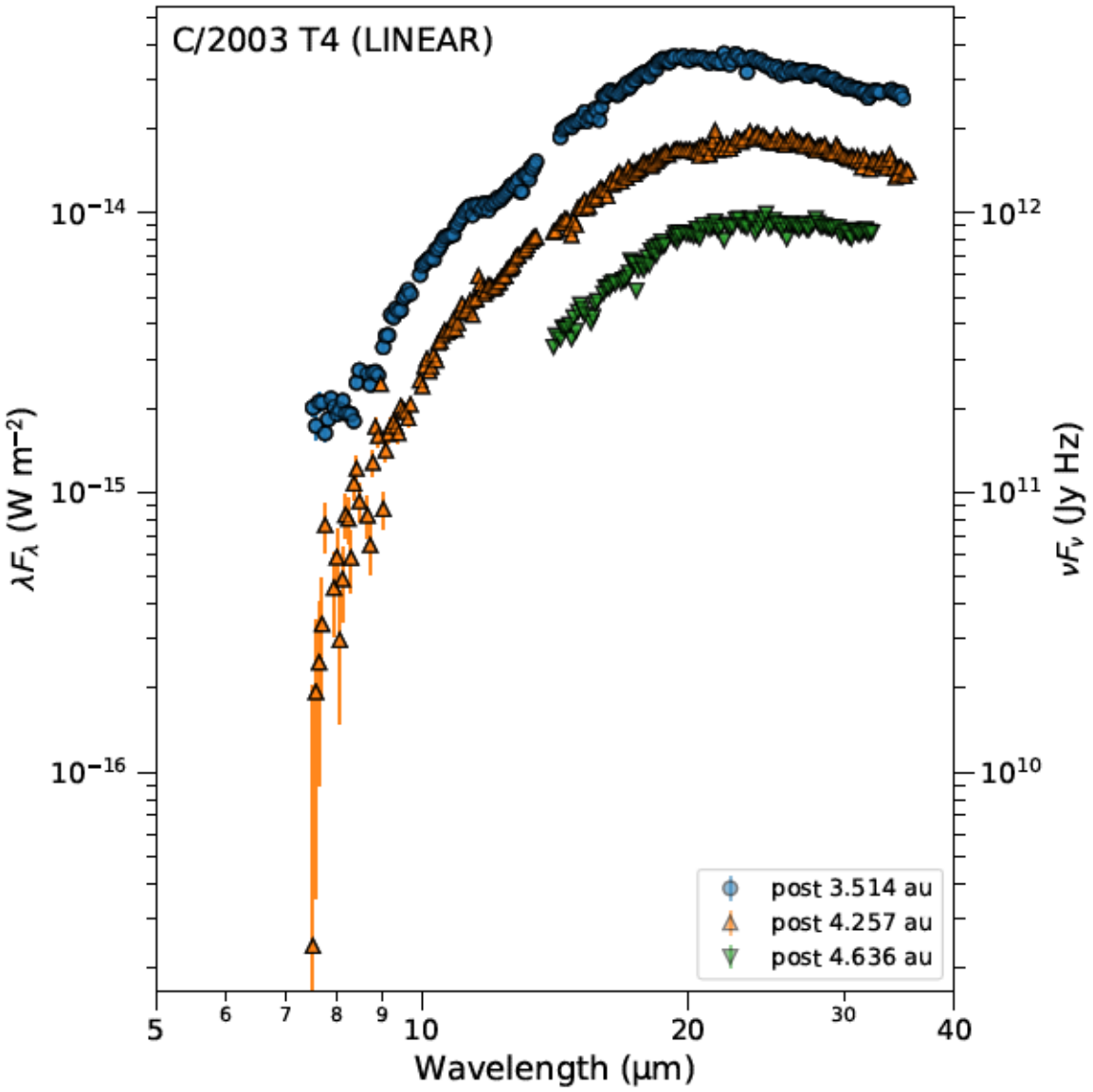

Figure 36: Comet C/2003 T4 (LINEAR).

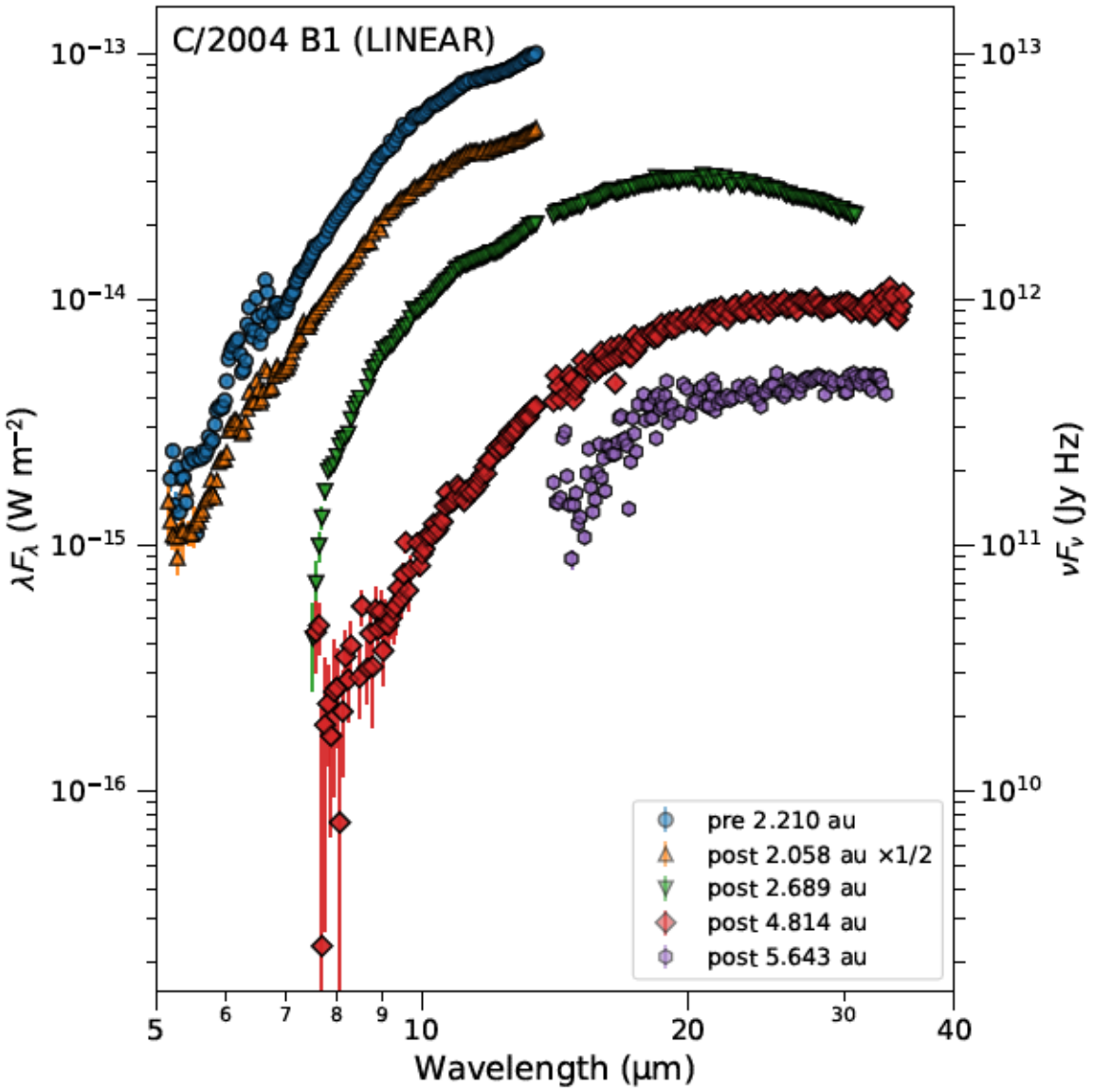

Figure 37: Comet C/2004 B1 (LINEAR).

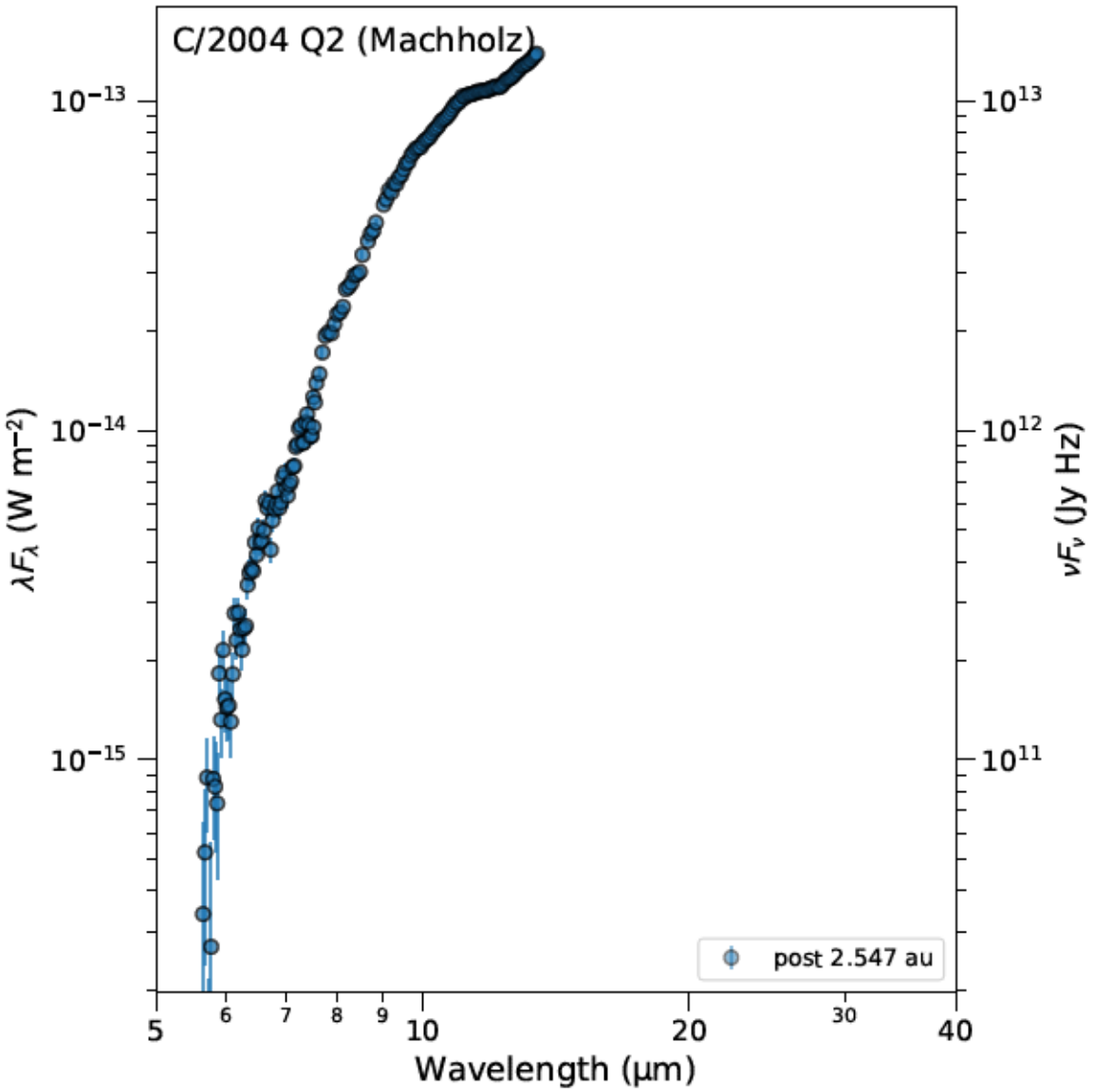

Figure 38: Comet C/2004 Q2 (Machholz).

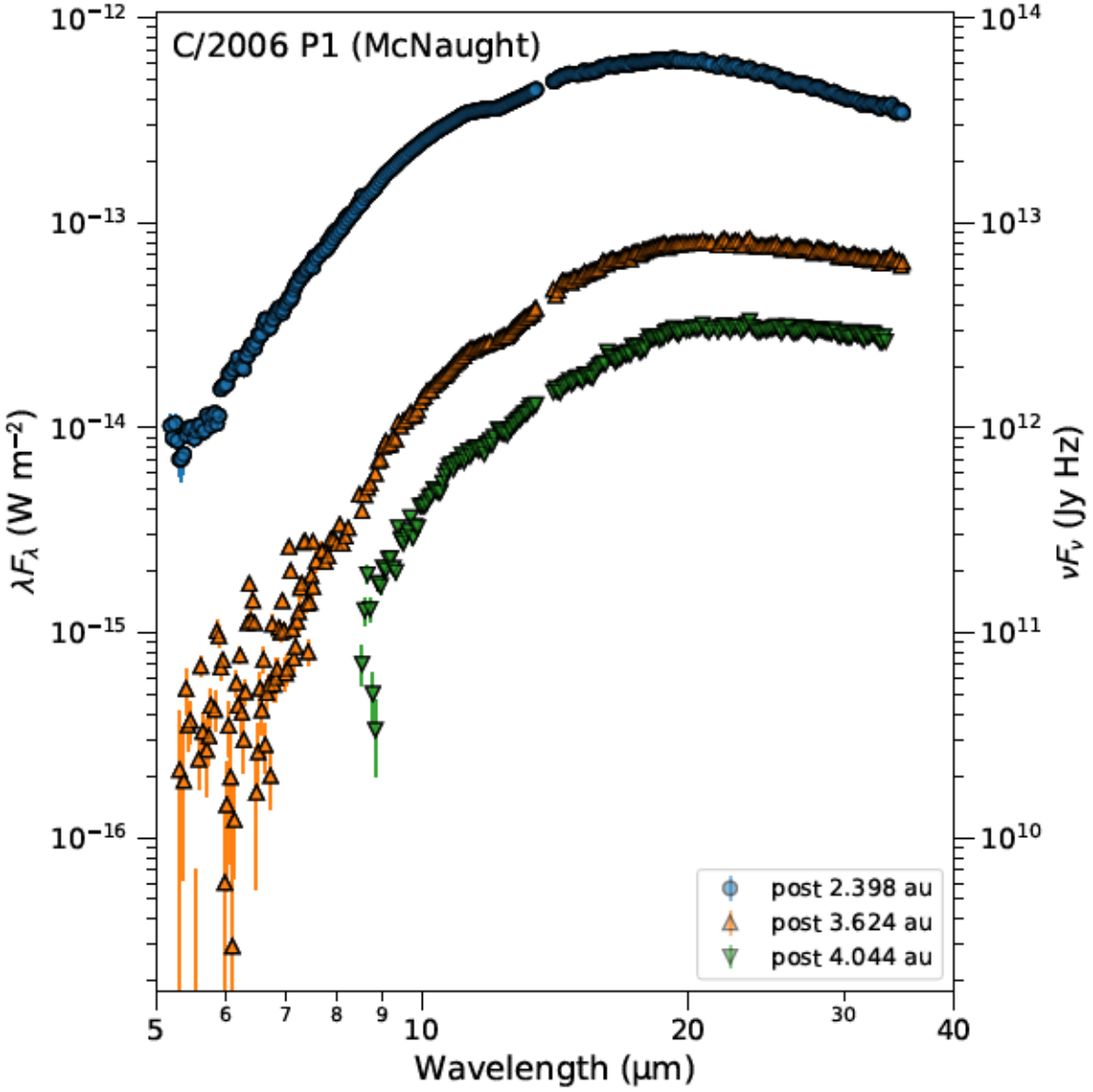

Figure 39: Comet C/2006 P1 (McNaught).

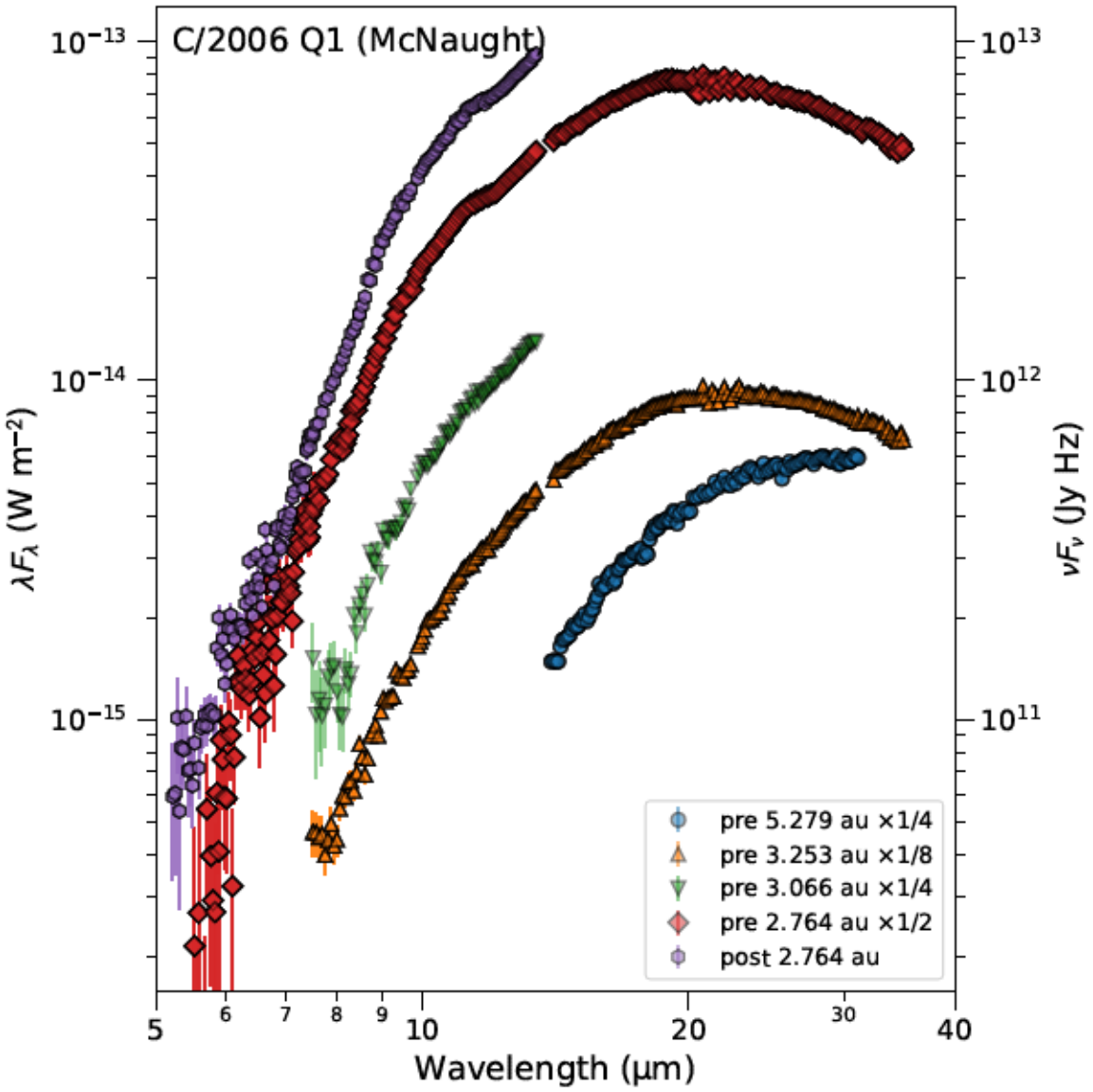

Figure 40: Comet C/2006 Q1 (McNaught).

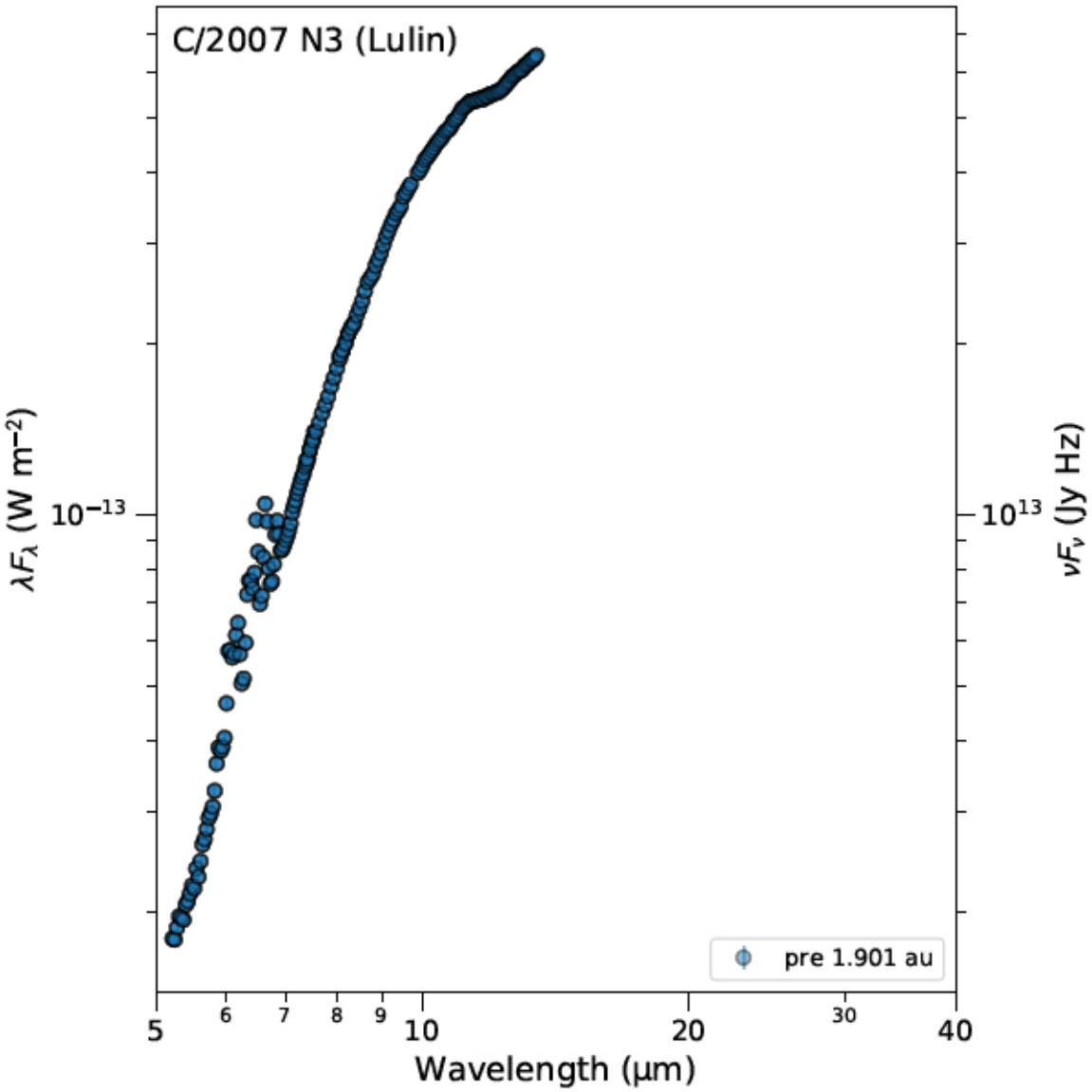

Figure 41: Comet C/2007 N3 (Lulin).

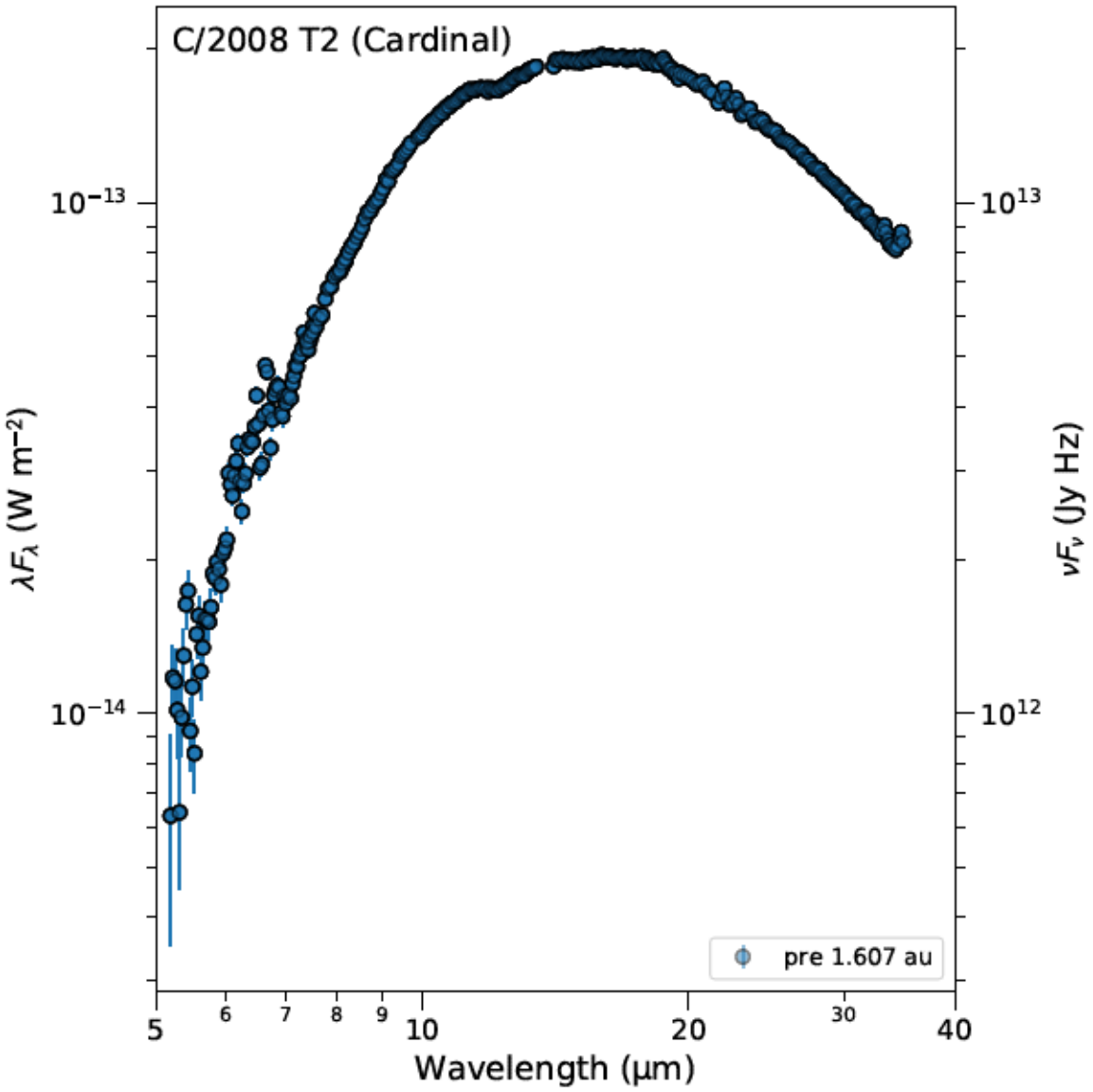

Figure 42: Comet C/2008 T2 (Cardinal).